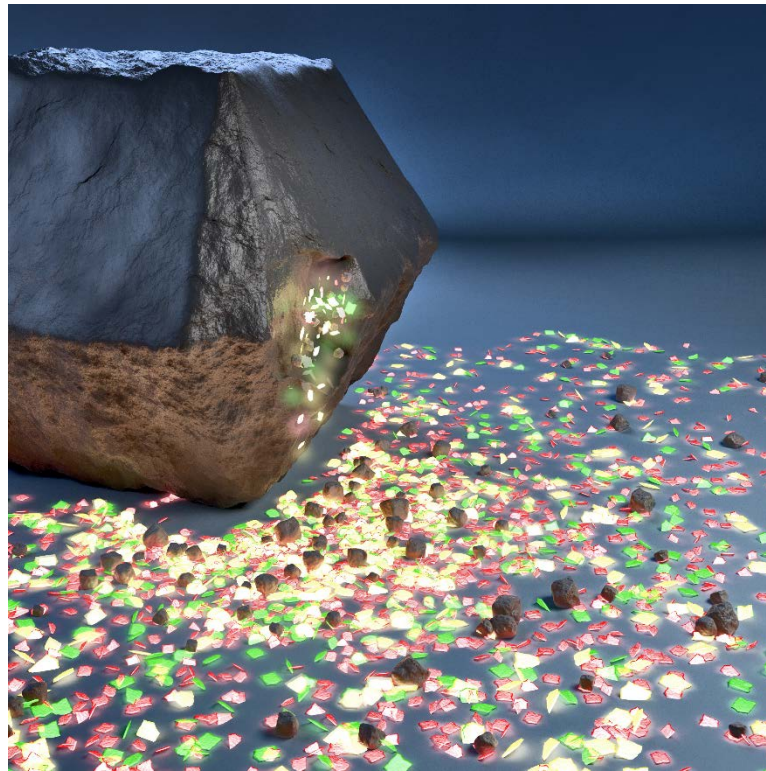


Tuning the carrier dynamics in light-emitting lead halide perovskite nanoplatelets

Verena A. Hintermayr



München, 2017



Tuning the carrier dynamics in light-emitting lead halide perovskite nanoplatelets



Dissertation

an der Fakultät für Physik der
Ludwig-Maximilians-Universität München

vorgelegt von

Verena Agnes Hintermayr
aus Wasserburg am Inn

München, 12.12.2017

Erstgutachten:

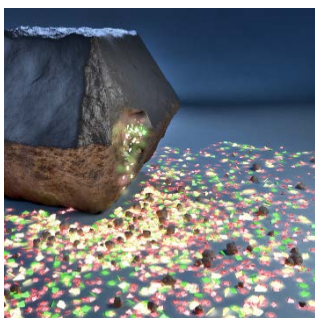
Prof. Dr. Jochen Feldmann

Zweitgutachten:

Prof. Dr. Uli Lemmer

Tag der mündlichen Prüfung:

16.02.2018



The cover picture of this thesis was designed by M. Eng. Christoph Hohmann (Nanosystems Initiative Munich) and was selected to appear on the front cover of *Advanced Materials* (volume 28, issue 43) published in 2016. It illustrates the exfoliation of lead halide perovskite nanoplatelets from microcrystals through ligand-assisted liquid-phase tip-sonication.

Zusammenfassung

Innerhalb der letzten vier Jahre haben organisch-anorganische Bleihalogenid-Perowskit-Nanokristalle, die für lichtemittierende Anwendungen bemerkenswerte Merkmale zeigen, viel Aufmerksamkeit erzeugt. Die optischen Eigenschaften dieser Nanokristalle sind sowohl über ihre Materialzusammensetzung als auch über ihre Größe steuerbar. Obwohl die hier untersuchten zweidimensionalen Bleihalogenid-Perowskit-Nanoplättchen bei Raumtemperatur als Kolloidlösung vorliegen, besitzen sie Eigenschaften, die stark an epitaktisch gewachsene Halbleiter-Quantentöpfe erinnern.

In dieser Arbeit wird zum ersten Mal eine von Liganden unterstützte Exfoliation zur Herstellung von Methylammonium-Bleihalogenid-Nanoplättchen erfolgreich durchgeführt. Die auf diese Weise synthetisierten Nanoplättchen, deren Dicke bis hin zu einzelnen Perowskit-Monolagen kontrollierbar ist, sind sehr stabil. Eine gezielte Trennung unterschiedlich dicker Nanoplättchen ermöglicht es zum ersten Mal, optische Eigenschaften in Abhängigkeit der Monolagenanzahl zu untersuchen. So zeigen die Absorptionsspektren eine große Ähnlichkeit zu bekannten zweidimensionalen Halbleitern. Anhand dieser Spektren wird außerdem die jeweilige Exzitonenbindungsenergie bestimmt. Diese erreicht für einzelne Monolagen Werte von bis zu 300 meV und unterscheidet sich somit stark von Perowskit-Dickschichten, deren Exzitonenbindungsenergie weniger als ein Zehntel davon beträgt. Zudem wird die dickenabhängige Verschiebung der Spektren, welche auf Quanteneffekte zurückzuführen ist, untersucht. Zeitaufgelöste Absorptions- und Photolumineszenzmessungen ermöglichen darüber hinaus eine detaillierte Analyse der Ladungsträgerdynamiken. Hierbei weisen die Abkühlung der Ladungsträger und die Dynamik der Exzitonen eine eindeutige Abhängigkeit zur Nanoplättchendicke auf. So wird in den zweidimensionalen Nanoplättchen eine signifikant kürzere Abkühlzeit als in den deutlich dickeren, dreidimensionalen Nanoplättchen festgestellt. Es wird außerdem gezeigt, dass im Gegensatz zum zweidimensionalen Fall die in dreidimensionalen Nanoplättchen resonant erzeugten Exzitonen bereits wenige hundert Femtosekunden nach ihrer optischen Anregung dissoziieren. Des Weiteren wird nachgewiesen, dass ein Abfall der Photolumineszenzlebensdauer mit einer Abnahme der Nanoplättchendicke einhergeht. Dies kann wiederum mit der um etwa eine Größenordnung erhöhten Exzitonenbindungsenergie in Verbindung gebracht werden.

Die vorliegende Arbeit trägt zu einem fundierten Verständnis der Ladungsträgerdynamiken in zweidimensionalen Perowskit-Nanoplättchen und der daraus resultierenden optischen Eigenschaften bei. Insgesamt können die daraus gewonnenen Erkenntnisse helfen, Perowskit-Nanokristalle als nächste Generation optoelektronischer Bauelemente auf den Weg zu bringen.

Abstract

Organic-inorganic lead halide perovskite nanocrystals have gained a lot of attention within the last four years, because of their highly interesting properties for light-emitting applications. Their optical properties can be tuned not only through their composition but also through their size. The type of nanocrystals studied here are two-dimensional nanoplatelets with properties reminiscent of epitaxially grown semiconductor quantum wells, albeit they appear at room temperature and in the form of colloidal nanocrystals in solution.

In this work the preparation of highly stable methylammonium lead halide nanoplatelets by ligand-assisted exfoliation with a controlled thickness down to a single perovskite monolayer is presented for the first time. The separation of nanoplatelets with individual thicknesses enables for the first time thickness-dependent optical spectroscopy on lead halide perovskite nanoplatelets. The absorption spectra of these nanoplatelets show similarities to established two-dimensional semiconductors. Using these spectra the respective exciton binding energy is determined. It reaches values of up to 300 meV, which is more than 10 times the value of bulk films. Furthermore, the quantum-confinement induced shift of the absorption onset is examined as a function of the nanoplatelet thickness. In addition, time-resolved absorption and photoluminescence experiments are conducted, enabling a detailed analysis of the charge carrier dynamics in lead halide perovskite nanoplatelets. Interestingly, the carrier cooling behavior as well as the exciton formation dynamics exhibit a thickness dependence. It is shown that the cooling time measured for two-dimensional nanoplatelets is shorter than that of the much thicker, three-dimensional nanoplatelets. Moreover, a dissociation of resonantly excited excitons within a few hundreds of femtoseconds is only observed in three-dimensional nanoplatelets. Furthermore, the photoluminescence lifetime is found to decrease with decreasing number of crystal layers. Again, this can be attributed to the increase of the exciton binding energy by roughly one order of magnitude.

This thesis contributes to a fundamental understanding of carrier dynamics in two-dimensional perovskite nanoplatelets and of the resulting optical properties. Overall, this may help to incorporate perovskite nanocrystals into the next generation of optoelectronic components.

Publications and conferences

Scientific publications of results presented in this work

- V. A. Hintermayr, A. F. Richter, F. Ehrat, M. Döbinger, W. Vanderlinden, J. A. Sichert, Y. Tong, L. Polavarapu, J. Feldmann, A. S. Urban
Tuning the Optical Properties of Perovskite Nanoplatelets through Composition and Thickness by Ligand-Assisted Exfoliation
Advanced Materials 28(43): 9478-9485 (2016)
(CeNS Publication award 2016, Category: Best junior scientist publication)
- V. A. Hintermayr, A. S. Urban, J. Feldmann
Relaxation dynamics of photoexcited electron-hole pairs in 2D and 3D MAPI nanoplatelets
in preparation (2017)

Additional publications

- Y. Tong, E. Bladt, M. F. Aygüler, A. Manzi, K. Z. Milowska, V. A. Hintermayr, P. Docampo, S. Bals, A. S. Urban, L. Polavarapu, J. Feldmann
Highly Luminescent Cesium Lead Halide Perovskite Nanocrystals with Tunable Composition and Thickness by Ultrasonication
Angewandte Chemie 55(44):13887-13889 (2016)
- V. A. Hintermayr, C. Lampe, M. Löw, J. Feldmann, T. Lohmüller, A. S. Urban
Enhanced environmental stability of self-assembled organic-inorganic perovskite nanocrystals
in preparation (2017)

Contributions to conferences and workshops

- V. A. Hintermayr, R. Oliver, M. Kappers, P. Dawson, J. Stolarczyk, J. Feldmann
Deposition of Au Nanoparticles on GaN surfaces: Effect of decoration on photocurrent measurement (Poster)
3rd International SolTech Conference, Wildbad Kreuth, Germany, April 2014
- V. A. Hintermayr
Effect of gold Nanoparticle deposition on the photoactivity of GaN films (Talk)
Workshop on Photonics and Optoelectronics, Hirschegg-Kleinwalsertal, Austria, September 2014
- V. A. Hintermayr, N. Mutz, C. Cardenas-Daw, M. Fu, J. Stolarczyk, A. S. Urban, J. Feldmann
Fluorescence studies on single lead iodide and lead bromide perovskite particles (Poster)
4th International Solar Technologies Go Hybrid-Workshop, Bad Staffelstein, Germany, March 2015
- V. A. Hintermayr, J. A. Sichert, N. Mutz, C. Cardenas-Daw, Y. Tong, M. Vollmer, M. Fu, J. Stolarczyk, A. S. Urban, J. Feldmann
Fluorescence studies on organometal halide perovskite nanoparticles (Talk)
E-MRS Spring Meeting, Lille, France, May 2015
- V. A. Hintermayr, L. Polavarapu, A. S. Urban, J. Feldmann
Controlling optical properties of organic/inorganic halide perovskites by means of size and composition (Talk)
DPG Spring Meeting, Regensburg, Germany, March 2016
- V. A. Hintermayr, A. F. Richter, L. Polavarapu, A. S. Urban, J. Feldmann
Wide photoluminescence tunability of organic/inorganic halide perovskites by controlled variation of size/dimension and composition (Poster)
5th International SolTech Conference Solar, Munich, Germany, April 2016
- V. A. Hintermayr
Time-resolved measurements on thickness-controlled perovskite nanoplatelets (Talk)
Workshop on Photonics and Optoelectronics with New Materials, Lenggries, Germany, July 2016
- V. A. Hintermayr, A. F. Richter, F. Ehrat, M. Döblinger, W. Vanderlinden, Y. Tong, J. A. Sichert, L. Polavarapu, J. Feldmann, A. S. Urban,

Thickness dependence of excitonic decay of methylammonium lead halide perovskites
(Poster)

2nd International Conference on Perovskite Solar Cells and Optoelectronics, Genoa, Italy, September 2016

- V. A. Hintermayr, L. Polavarapu, Y. Tong, E. Bladt, M. F. Aygüler, A. Manzi, K. Z. Milowska, P. Docampo, S. Bals, A. S. Urban, J. Feldmann

Highly Luminescent Cesium lead halide perovskite (CsPbX_3 , $X = \text{Cl, Br and I}$) Nanocubes and Nanoplatelets (Poster)

2nd International Conference on Perovskite Solar Cells and Optoelectronics, Genoa, Italy, September 2016

- V. A. Hintermayr

Material characterization techniques based on electrons (Talk)

Workshop on Optical Spectroscopy of New Material, Syracuse, Italy, March 2017

- A. F. Richter, V. A. Hintermayr, L. Polavarapu, A. S. Urban, J. Feldmann

Exciton Dynamics in Perovskite Nanoplatelets: The Influence of Crystal Thickness
(Poster)

6th SolTech Conference, Munich, Germany, October 2017

- V. A. Hintermayr, B. J. Bohn, L. Polavarapu, A. S. Urban, J. Feldmann

Relaxation Dynamics of Photoexcited Electron-Hole Pairs in Methylammonium Lead Iodide Nanoplatelets (Talk)

MRS Fall Meeting, Boston, USA, November 2017

Contents

Zusammenfassung	I
Abstract	III
1 Introduction	1
2 Fundamentals	5
2.1 Lead halide perovskites	6
2.1.1 Chemical class of lead halide perovskites	6
2.1.2 Electronic band structure and density of states	7
2.1.3 Linear absorption	11
2.1.4 Temperature dependence of the semiconductor band gap	13
2.1.5 Free carriers versus excitons	16
2.1.6 Lead halide perovskite nanocrystals (2D)	19
2.2 Reduced dimensionality: From 3D to 2D	22
2.2.1 Quantum confinement	22
2.2.2 Optical absorption in 2D materials	23
2.3 Ultrafast optical phenomena	26
2.3.1 Carrier relaxation regimes	26
2.3.2 Recombination dynamics	27
2.3.3 Nonlinear optical response of semiconductors	29
3 Experimental methods	31
3.1 Structural and compositional analysis	32
3.1.1 Electron microscopy	32
3.1.2 Atomic force microscopy	35
3.1.3 X-ray diffraction	36

3.2	Optical characterization techniques	38
3.2.1	Steady-state spectroscopy	38
3.2.2	Time-resolved spectroscopy	41
3.3	Synthesis: Ligand-assisted exfoliation	45
3.3.1	Precursor synthesis	45
3.3.2	Synthesis of perovskite nanoplatelets	45
3.3.3	Separation of thinner and thicker nanoplatelets by centrifugation	47
3.3.4	Preparation of mixed halide perovskite nanoplatelets	47
4	Fabrication and separation of nanoplatelets with individual thicknesses	49
4.1	Bulk-like perovskite nanocrystals of different composition	50
4.1.1	Synthesis and structural analysis of perovskite nanocrystals	50
4.1.2	Mixed-halide perovskite nanoplatelets	53
4.2	Separation of perovskite nanoplatelets with different thicknesses	57
5	Thickness-dependent absorption and emission of perovskite nanoplatelets	65
5.1	Quantum confinement-induced shift of band gap and exciton binding energy	66
5.1.1	Two-step quantum well model	67
5.1.2	Modeled absorption spectra based on the Elliott formula	69
5.2	Tunability of emission by size and composition	73
5.3	Temperature-dependent absorption and photoluminescence measurements	76
6	Carrier dynamics in 2D and 3D MAPI nanoplatelets: Excitons versus free carriers	81
6.1	Transient absorption spectroscopy measurements	82
6.1.1	Linear and transient absorption of MAPI nanoplatelets	82
6.1.2	State filling: Analysis of the continuum and excitonic state	83
6.1.3	Recombination mechanism in 3D and 2D MAPI nanoplatelets	85
6.1.4	Hot carrier cooling in 2D and 3D perovskite nanoplatelets	88
6.1.5	Dissociation of excitons in MAPI nanoplatelets	94
6.2	Thickness-dependent time-resolved photoluminescence measurements	98
7	Conclusion and outlook	103
	Bibliography	107
	Acknowledgment	129

Introduction

The name perovskite identifies a class of minerals that were first discovered in the Ural Mountains in the year 1839 and named after the founder of the Russian Geographic Society, Lev Perovskite. The original perovskite mineral, calcium titanate (CaTiO_3), is composed of calcium, titanium and oxygen with the characteristic ABX_3 stoichiometry. However, the name perovskite has since been applied to every compound with the same crystallographic structure and stoichiometry. Already in the year 1908, the basic properties of titanate-based compounds were analyzed [1]. Furthermore, in the '40s, the demonstration of ferroelectricity in barium titanate (BaTiO_3) created interest towards the understanding of their unique electronic properties [2, 3]. First studies on organic-inorganic perovskites were conducted by Dieter Weber in the late '70s and in the following years their exceptional chemical and physical properties were examined [4, 5]. Some significant progress in this area was achieved by the research group led by David Mitzi [6, 7]. Back then the general interest was merely minor and seemed to cease. However, in the year 2009 the material was rediscovered as the first reports of organic-inorganic hybrid perovskites used as sensitizers in solar cells appeared, yielding a light-to-electricity conversion efficiency of 3.8 % [8]. Since then, an unprecedentedly rapid enhancement of power conversion efficiencies has been accomplished. Currently, there are reports on perovskite solar cells with an efficiency exceeding 22 % [9]. Moreover, combining perovskites with silicon promises further enhancement as already been demonstrated by a tandem solar cell boasting 25 % power conversion efficiency [10]. These numbers are comparable to silicon based devices, making perovskites a conceivable contender to rival the prevalence of crystalline silicon solar cells. To put this into perspective, the development of single-junction GaAs cells with an efficiency of roughly 29 % [11] took nearly 60 years.

Triggered by the research on solar cells, the interest on perovskite nanostructures has again gained a fresh impetus. Low dimensional layered perovskite materials were already

studied in the '90s [6, 12–14], but the recent development of bright and colloidal stable perovskite nanocrystals [15–18] widens the possible experimental opportunities enabling new fields of application. Due to their intriguing optical and electrical properties, hybrid organic-inorganic methylammonium lead halide perovskites described by the chemical formula $\text{CH}_3\text{NH}_3\text{PbX}_3$ ($\text{X} = \text{I}, \text{Br}, \text{Cl}$) are promising components to develop not only efficient solar cells but also other high-performance optoelectronic devices such as light-emitting diodes [19], photodetectors [20], optically pumped lasers [21, 22] and field-effect transistors [23]. Some of the unique properties of lead halide perovskites, which have led to this are long carrier diffusion lengths [24, 25], long photocarrier lifetimes [26], a high absorption coefficient [27] and the tunability of the band gap through size and halide composition [28]. Furthermore, colloidal perovskite nanocrystals show very high photoluminescence (PL) quantum yields of more than 95 % [29].

Still, there are three main concerns regarding the handling of devices comprising perovskites: (i) Halide ion migration, (ii) toxicity and (iii) limited chemical and thermal stability. 2D perovskite materials exhibit unique properties which can help to overcome these issues and favor their usage in solar cells, transistor and light emitting devices [30, 31]. It has been proven that the stability issue can be addressed using nanoplatelets (NPLs). Less degradation due to air and water exposure has been observed in quantum-confined perovskite structures compared to their bulk counterpart likely linked to surface passivation and an additionally applied layer of ligands [32–34]. Furthermore, perovskite nanoplatelets exhibit strong quantum confinement effects that arouse particular interest, along with the already mentioned band gap tunability, that can be obtained by means of both halide composition and crystal size [35–37]. In the case of methylammonium lead iodide (MAPI) a blue-shift of the emission energy of 0.68 eV can be observed by reducing the thickness of the nanoplatelets down to a single unit cell. Therefore, one can control the emission wavelength of perovskite nanoplatelets over the entire visible range by tuning merely their size.

In the scope of this work, a new synthesis of highly stable colloidal perovskite nanoplatelets is introduced, the so-called ligand-assisted exfoliation. This synthesis enables the controlled synthesis of hybrid organic-inorganic methylammonium lead halide perovskite nanoplatelets of a certain thickness and halide composition. Within this work the fabrication of quantum-confined nanoplatelets consisting of mixed halides is demonstrated for the first time. Furthermore, a model is created to help the understanding of the observed quantum size effects. Additionally, time-resolved spectroscopy is applied to study the carrier dynamics and to resolve the vagueness that still surrounds the basic characteristics of this semiconductor. Although a lot of research on perovskites has been

done in the last couple of years, many issues are still not completely understood. Some of these, such as the role of excitons and free carriers, the exact value of the exciton binding energy, hot carrier cooling and the effect of the dimensionality on optical properties, are addressed and investigated throughout this thesis.

In general, fundamental studies on perovskite nanoplatelets are necessary to gain a better understanding and control of the electronic and optical properties of perovskites. An unambiguous knowledge of the perovskite photosystem is desirable as it facilitates the application and optimization of perovskite nanostructures for modern optoelectronic devices.

Fundamentals

In this chapter the fundamental characteristics of perovskites are scrutinized more closely. Perovskite materials show many differences compared to well-known and extensively studied semiconductors like gallium arsenide (GaAs), silicon (Si) or cadmium sulfide (CdS). Especially the rich chemical structural complexity and multifunctional properties of perovskites has quicken interests. To be able to explain those properties, it is helpful to analyze this class of material in comparison to conventional semiconductors using established pictures and concepts of semiconductor physics. The research on the fundamental properties of lead halide perovskites has mainly been performed in the last couple of years and most of the cited literature was published during the work on this thesis.

As a basis, the chemical structure of perovskites and their band structure is introduced. Afterwards, the interaction and coupling of charge carriers to light, to each other and to phonons is examined. In this work, the fabrication of two-dimensional lead halide perovskite nanostructures, so-called nanoplatelets (NPLs), with controlled thicknesses is reported, enabling thickness-dependent studies on linear absorption and ultrafast optical phenomena. Hereby, the impact of quantum confinement is of special interest. Hence, characteristic qualities of three-dimensional (3D) and two-dimensional (2D) semiconductors are discussed in more detail. Additionally, basic principles of optical nonlinearities are presented. This is necessary to evaluate and discuss time-resolved measurements, which are presented in chapter 6 .

2.1 Lead halide perovskites

2.1.1 Chemical class of lead halide perovskites

Perovskites refer to a crystallographic family which represents any compound with a general ABX_3 stoichiometry and which show a crystal structure similar to the archetypical perovskite $CaTiO_3$ [38, 39]. The first report on perovskites was already made in the year 1839 by the German mineralogist Gustav Rose [40]. The A, B and X sites stand for three particular lattice positions. The crystal structure of perovskites is shown in figure 2.1. The component denoted by B is located in the center of a regular octahedron created by the X components. These $[BX_6]^{-4}$ octahedra define a corner-sharing network that creates cuboctahedral gaps wherein the A component is centered. In the presented thesis all studies are performed on lead halide perovskites, which are mainly considered in the following. In this case, the B component is lead (Pb^{2+}) and the X component is either iodide, bromide, chloride or a mixture of these. Depending on the A cation, which is either an organic molecule or an inorganic cation, organic-inorganic (hybrid) or all-inorganic lead halide perovskites are obtained, respectively.

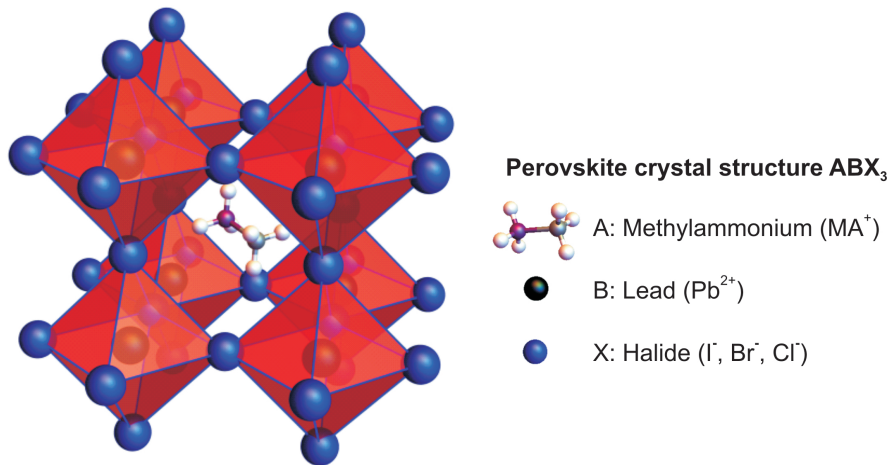


Figure 2.1: Perovskite crystal structure (ABX_3). Methylammonium lead halide is sketched as an example. The X components (halide (I^- , Br^- , Cl^-)) define a corner-sharing network of octahedra. In the center of those octahedra, the B component (lead (Pb^{2+})) is located. The A component (methylammonium (MA^+)) is centered in the gap between these octahedra.

Many different compounds can be combined to form the perovskite crystal structure. In order to estimate the stability of those, one can apply the semi-empirical Goldschmidt tolerance factor [41]

$$t = \frac{r_A + r_X}{\sqrt{2} \cdot (r_B + r_X)}, \quad (2.1)$$

with r_A, r_B and r_X being the ionic radii of the components A, B and X. Studies have shown that most metal halide perovskites exist within the boundaries $0.81 \leq t \leq 1.0$ [42]. Various examples of possible perovskite compounds are listed in literature [43–47] showing the diversity of this material class.

As already mentioned, this thesis focuses on lead halide perovskites. More precisely, methylammonium lead halide perovskite nanocrystals (NCs) are investigated. The methylammonium (CH_3NH_3^+ or simply MA) is the organic content and acts as the A component in the ABX_3 stoichiometry. Depending on the halide, these will be referred to as MAPI (methylammonium lead iodide, $\text{CH}_3\text{NH}_3\text{PbI}_3$), MAPBr (methylammonium lead bromide, $\text{CH}_3\text{NH}_3\text{PbBr}_3$) or MAPCl (methylammonium lead chloride, $\text{CH}_3\text{NH}_3\text{PbCl}_3$).

The crystal structure shows a large number of possible polymorphs. Changes can be induced by external physical parameters such as pressure, electric or magnetic fields and especially by the temperature. Depending on the temperature, MAPI, MAPBr and MAPCl can be found in the orthorhombic (low temperature), tetragonal (intermediate temperature) or cubic phase (high temperature). The exact temperatures at which the transitions between these phases take place vary depending on the halide content. More detailed studies on the phase transitions and structural arrangements of the different phases can be found in section 2.1.4. Most measurements presented in this work were performed at room temperature. In this temperature range, MAPI is present in the tetragonal phase, whereas MAPBr and MAPCl are in the cubic phase [48, 49].

2.1.2 Electronic band structure and density of states

The electronic band structure describes the range of allowed energies and k-values of electrons and holes in a solid. A detailed understanding of the band structure of a material is a prerequisite for insight into properties such as optical absorption, excited state lifetime and carrier recombination mechanisms.

In this section the electronic band structure of perovskites, more precisely MAPI, is examined and compared to a well-known conventional semiconductor, namely GaAs. The accurate determination of the electronic band structure is challenging and different approaches have been used to cope with appearing difficulties. The electronic band structure of perovskites has been studied extensively using density-functional theory (DFT) [50–52]. One main disadvantage of this method is that the band gap is generally underestimated [53]. These insufficiencies can be overcome by the implementation of relativistic corrections and spin-orbit coupling (SOC) [54]. Another approach is to use quasiparticle self-consistent GW theory (G is the Green’s function and W the screened Coulomb in-

teraction) [55]. In recent literature one can find a manifold of theoretical approaches to investigate the electronic properties of lead halide perovskites [56, 57].

Figure 2.2a) illustrates the band structure of MAPI obtained from DFT calculations, if a simple pseudocubic structure is assumed. MAPI is a direct band gap semiconductor with a band gap located at the R point. That is unlike most well-known semiconductors, which commonly have their band gaps located at the Γ -point. The slightly differing energy position of M_{1-3} and X_{1-3} , respectively, is caused by the distorted cubic structure. Figure 2.2b) depicts the density of states (DOS), highlighting the DOS close to the valence band maximum (VBM) and the conduction band minimum (CBM). The electronic band structure of MAPI near the fundamental band edge is dominated by iodide and lead. The molecular states of MA^+ merely play a subordinate role [58]. Hence, for a calculation of the DOS only the partial DOS distribution of the Pb 6p, Pb 6s and I 5p states are important and illustrated in figure 2.2b).

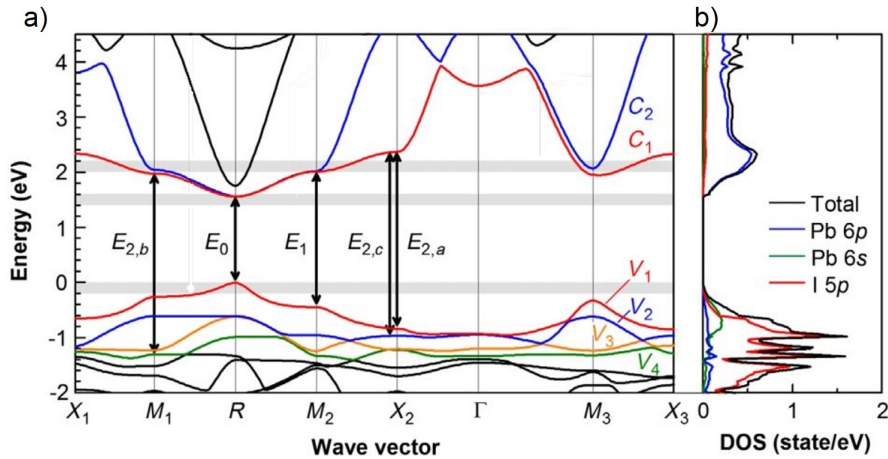


Figure 2.2: Band structure and DOS of MAPI. a) Band structure of MAPI obtained from DFT calculations by assuming a simple pseudocubic structure. b) Total DOS distribution for Pb 6p, Pb 6s and I 5p. Figure taken from Shirayama et al. [50].

At the VBM the electronic band structure of MAPI is dictated by the $[PbI_6]^{-4}$ building blocks. In figure 2.3a) the bonding diagram of such isolated $[PbI_6]^{-4}$ clusters is presented in order to characterize the VBM. This building block has a lowest unoccupied molecular orbital (LUMO) consisting of Pb 6p - I 5s antibonding orbitals and a highest occupied molecular orbital (HOMO) of Pb 6s - I 5p antibonding orbitals, respectively. Like for the isolated $[PbI_6]^{-4}$ building block the VBM of MAPI is built up by the hybridization of Pb 6s and the I 5p orbitals and has an antibonding character. The CBM is mainly formed by the Pb 6p orbitals [59]. A simplified picture of the energy levels of MAPI is shown in figure 2.3b). As illustrated in figure 2.3b) and c), perovskites show an inverted electronic band structure compared to conventional III-V semiconductors such as GaAs. In contrast

to MAPI, in GaAs the upper valence band (VB) is dominated by p states (As 4p) and the lower conduction band (CB) by s states (Ga 4s, As 4s), respectively. This 'inversion' of the band structure as compared to GaAs suggests the possible appearance of interesting phenomena for MAPI and makes lead halide perovskites a special class of semiconductors.

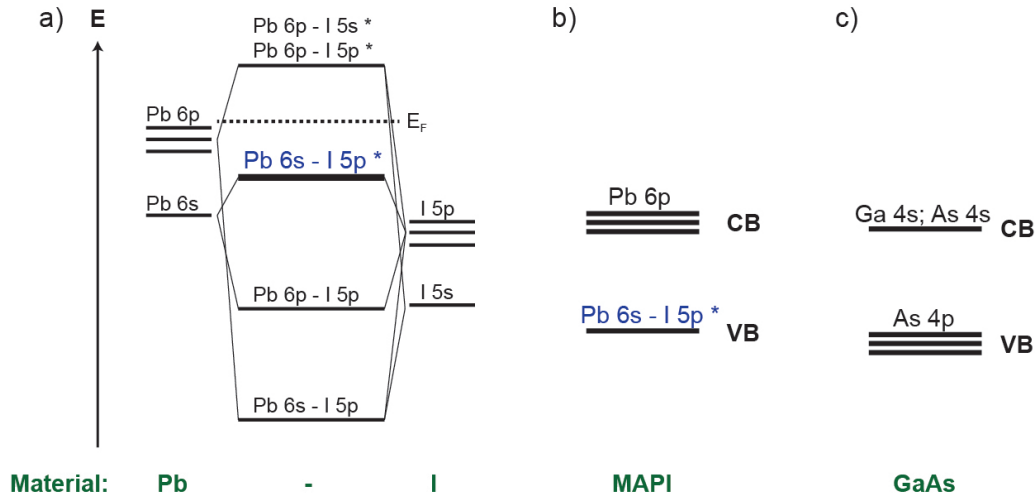


Figure 2.3: Comparison of energy levels of MAPI and GaAs. a) Block diagram of an isolated $[\text{PbI}_6]^{-4}$ cluster according to Umebayashi et al. [60] b) Energy levels of MAPI (3D) with a p-like conduction band c) Energy levels of GaAs. In comparison to MAPI, the band structure of GaAs is inverted.

Spin-orbit coupling

One consequence of the inverted band structure is that the spin-orbit coupling of MAPI affects the conduction band and not the valence band like in conventional semiconductors, e.g. GaAs. The spin-orbit coupling is a phenomenon in quantum physics which describes the interaction of the spin of a particle with its motion [61]. As lead and iodide have large atomic numbers the SOC is supposed to be considerably large and leads to a splitting of the 3-fold degenerate CBM into a lower 2-fold degenerate CBM and a higher energy 4-fold degenerate state. Since the split-off band (SO) in the CB is energetically lowered by this splitting, the band gap is reduced. In MAPI, the calculated contribution of SOC can be as large as the band gap itself. Further calculations show that the VB is practically unchanged by the SOC [62]. In contrast, in typical semiconductors the SOC causes a splitting of the upper VB due to its p character, but the CB remains virtually unchanged [63]. In figure 2.4, a sketch depicts the SOC in hybrid perovskites (e.g. MAPI) and III-V semiconductors (like GaAs). The split-off bands with an energy difference Δ with respect to the CBM or VBM, respectively, are illustrated for both cases. For GaAs, when taking

into account the SOC, the bands of the heavy hole (HH) and light hole (LH) are shifted to higher energies whereas the SO band is lowered in energy. The SO is lowered by $2/3 \cdot \Delta$ and the HH and LH are raised consequently by $1/3 \cdot \Delta$ relative to the band positions without SOC. In the case of hybrid perovskites, the light electron (LE) and heavy electron bands (HE) are shifted to higher energies and the SO band is lowered.

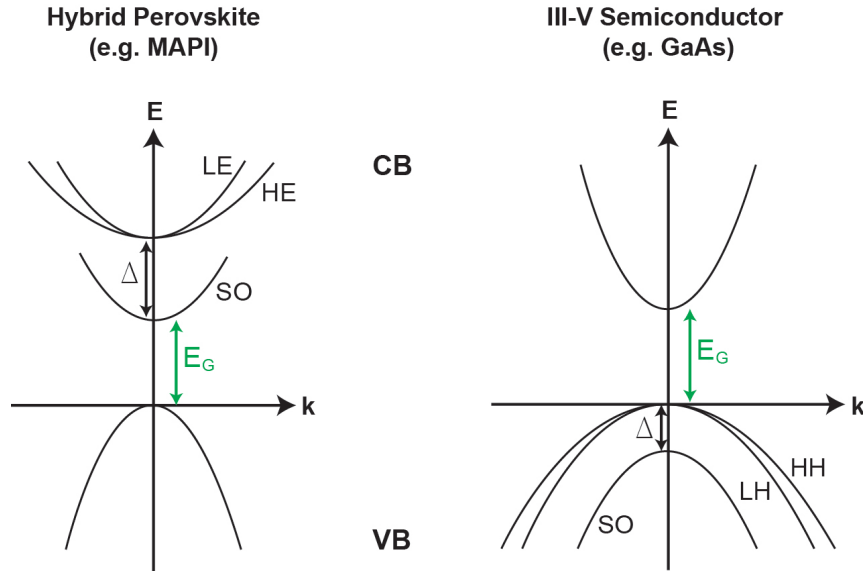


Figure 2.4: Comparison of hybrid perovskites (e.g. MAPI) and III-V semiconductors (e.g. GaAs). The effect of SOC on the band structure and resulting split-off band (SO) is illustrated for III-V semiconductors and hybrid perovskites. The spin-orbit coupling has to be considered to calculate the actual band gap. In both cases the SO band is reduced in energy. In contrast to III-V semiconductors for perovskites the splitting is in the p-like CB.

Recent publications have reported on Rashba band splitting [64] in MAPI films [65]. The Rashba effect is directly linked to the SOC and has already been discussed for years in theoretical works [54, 63, 66–69]. It only occurs, if the inversion symmetry in the crystal is broken. This results in a splitting of single bands which are separated in k -space and consequently an indirect band gap instead of a direct band gap is formed [70]. For the samples analyzed in this thesis the Rashba effect and the related shift from a direct to an indirect semiconductor has not been observed. This is reasonable, since, there is no sufficient reason to expect a breaking of the inversion symmetry.

Effective masses

Recalling the calculated band structure (see figure 2.2a)) one can notice by comparing the upper VB and the lower CB that the curvatures near the R point are quite similar. In most

semiconductors, the energy bands close to the extrema can be described by a parabolic relationship of the energy and the momentum:

$$E = \frac{\hbar^2 k^2}{2m^*}, \quad (2.2)$$

where \hbar is the reduced Planck constant and m^* is the effective mass of the electron (hole) in the CB (VB). Using this parabolic approximation, the effective mass can be obtained from the band dispersion [71]:

$$m^* = \hbar^2 \left[\frac{\partial^2 E}{\partial k^2} \right]^{-1} \quad (2.3)$$

Intuitively, the steeper (flatter) the band at the band edges is, the lighter (heavier) is the effective mass. In GaAs or CdTe the lowest conduction band is more dispersive than the highest valence band and consequently the electron effective mass is much smaller than the effective mass of the hole. In contrast to that in MAPI, the effective mass of the holes and electrons almost equals ($m_e = 0.23, m_h = 0.29$), hence, carrier transport in perovskites is well balanced [52].

2.1.3 Linear absorption

A good first approach to characterize the band structure of a semiconductor experimentally is to measure its absorption spectrum. In the fundamental absorption process, a photon excites an electron from the VB to the CB. This can happen once the photon energy is equal to or larger than the band gap of the semiconductor, consequently one can observe a sudden rise in the absorption. Methylammonium lead halide (MAPbX₃) perovskites are direct semiconductors whose band structure and band gap can be tuned by changing the halide component. For example, with decreasing atomic size of the halide from iodide to bromide to chloride, the band gap increases [72]. In this chapter, MAPI is analyzed representatively.

The probability of the transition of an electron in an initial quantum mechanical state Φ_i to a final quantum mechanical state Φ_f by absorption of a photon is approximated by Fermi's golden rule [73, 74]:

$$W_{i \rightarrow f} = \frac{2\pi}{\hbar} \int |\langle v | \hat{H} | c \rangle|^2 \frac{2}{8\pi^3} \delta(E_C(\vec{k}) - E_V(\vec{k}) - \hbar\omega) d^3k \quad (2.4)$$

Here, $\langle v | \hat{H} | c \rangle$ is the transition matrix from state v in the VB to state c in the CB. The integration must be performed over the whole reciprocal space. In order to simplify this expression, it is often assumed that the transition matrix is independent of k and one obtains accordingly:

$$W_{i \rightarrow f} = \frac{2\pi}{\hbar} |\langle v | \hat{H} | c \rangle|^2 \int \frac{2}{8\pi^3} \delta(E_C(\vec{k}) - E_V(\vec{k}) - \hbar\omega) d^3k \quad (2.5)$$

The integrand is defined as the joint density of states (JDOS). Hence, the optical absorption of a semiconductor is basically given by the squared matrix element between the VB and the CB, which determines the probability of a transition, times the JDOS and provides the total number of possible transitions.

Figure 2.5 depicts the ideal cubic crystal structure of lead halide perovskites and the corresponding Brillouin zone (BZ) in the reciprocal space. With this, one can establish a better understanding of the described symmetry and correlate the crystal structure to the electronic band structure, thus, the absorption spectrum. The points of high symmetry

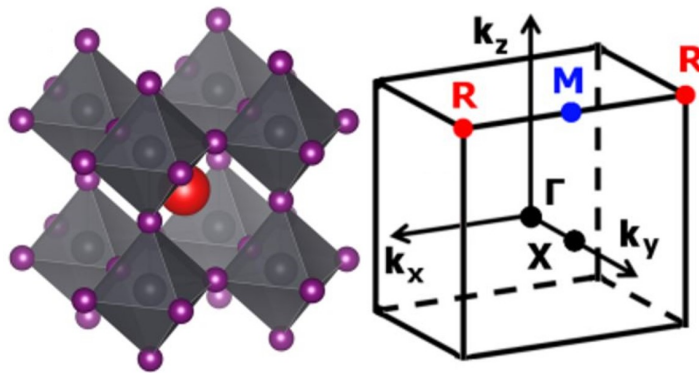


Figure 2.5: Crystal structure of lead halide perovskites in real space and the first Brillouin zone in the reciprocal space. The figures are taken from Even et al. [75].

are indicated as usual. In this section, the calculated absorption spectrum of the cubic phase is analyzed, although at room temperature MAPI is in the tetragonal phase. This is reasonable since the electronic band structures of these two phases show corresponding properties [76].

A simplified sketch of the previously elucidated electronic band structure and the corresponding absorption spectrum is shown in figure 2.6a) and b). Having a closer look at the absorption spectrum of MAPI, one can see a strong absorption onset at roughly 1.6 eV corresponding to the direct band gap of MAPI located at the R point. As expected from the electronic band structure the absorption continues to increase after the initial strong absorption onset. At roughly 2.6 eV a shoulder is recorded in the absorption spectra which can be attributed to the enhanced density of states at the M point. Transitions from bands energetically lower than the CB (CB2) or to bands energetically higher than the VB (VB2) induce additional features, which are marked in figure 2.6 with dashed blue arrows. It has to be mentioned that up to this point, all considerations are made for the one-particle picture not including the impact of Coulomb interaction.

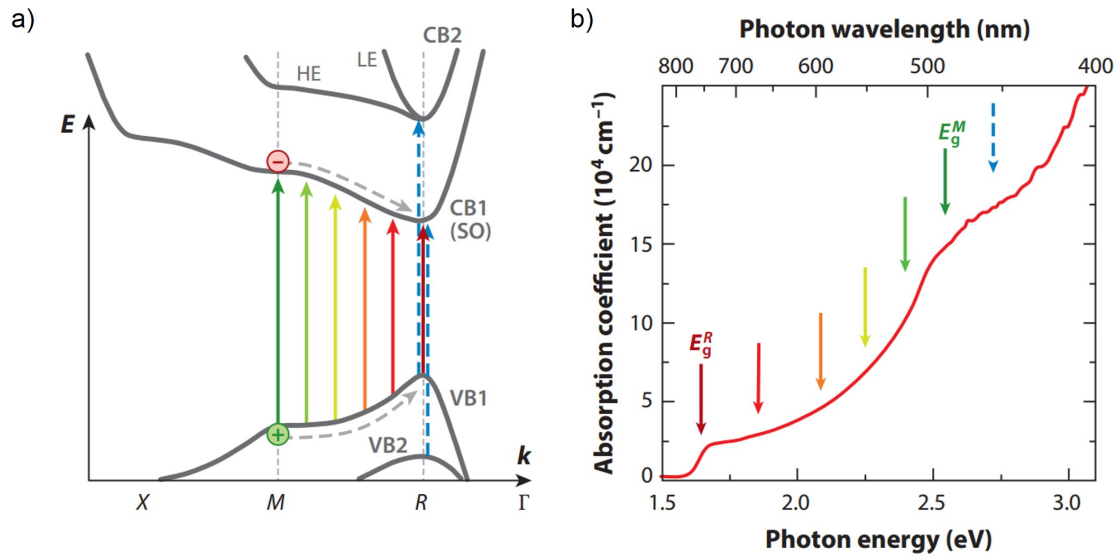


Figure 2.6: Relationship of the band structure with the absorption spectrum for MAPI films. a) Simplified electronic band structure of MAPI. The colored arrows indicate the photoinduced transitions from the valence band to the conduction band. The splitting of CB1 and CB2 is due to the SOC. b) Absorption spectrum of MAPI the arrows with the same colors are marking the position of the transition highlighted in a) in the absorption spectrum. Figures taken from Herz et al. [77].

2.1.4 Temperature dependence of the semiconductor band gap

External physical parameters can lead to changes of the energy levels of a semiconductor. Controlling these parameters such as pressure, temperature, electric and magnetic field can change the behavior of the semiconductor. In this section the impact of a variation of the temperature on semiconductors and in particular on lead halide perovskites is discussed. With increasing temperature, the lattice of the semiconductor expands and the atoms start to move faster and oscillate stronger. The spread lattice induces changes to the energy band gap and the energy levels broaden due to electron-phonon scattering. Not only the band structure but also the carrier population of energetic states is strongly affected by the temperature.

For many semiconductors the temperature dependence of the energy band gap can be obtained by applying the empirically determined Varshni relation [78]:

$$E_G(T) = E_G(0K) - \frac{aT^2}{T + b}, \quad (2.6)$$

with a and b being constants specific for the material and $E_G(T)$ the size of the band gap at different temperatures. This relation shows that for small temperatures the energy gap varies proportionally to the square of the temperature T^2 . For most well-known

semiconductors like Si, Ge, GaAs or InAs a and b are positive. Consequently, one can observe a reduction of the band gap with increasing temperature.

As discussed in section 2.1.2 perovskites are different in their electronic structure compared to conventional semiconductors like GaAs. Instead of a p-like VB and an s-like CB as in GaAs, in MAPI the band structure is inverted. As the unit cell volume (V) is decreased the interactions of the antibonding Pb 6s and I 5p states, which form the VBM, are enhanced, thus, resulting in a raise of the VBM. The CBM is nearly unchanged by the lattice contraction. Consequently, unlike many well-known semiconductors [79], perovskites exhibit a positive gap deformation potential (α_V) given by [80, 81]:

$$\alpha_V = \frac{\partial E_G}{\partial \ln(V)} > 0, \quad (2.7)$$

and for MAPI this potential is calculated to be 2.45 eV [82]. Hence, due to the inverted electronic band structure of perovskites with decreasing temperature a bathochromic shift of the absorption onset and PL can be observed (see figure 2.7). According to previous studies, IV-VI Pb-based compounds show a positive deformation potential like MAPI [83]. Perovskite materials do not obey the Varshni relation shown in equation (2.6). In ongoing work, many research groups are aiming to find an empirical relation to describe the variation of the band gap with temperature [84].

The change of the band gap with temperature can be observed by recording the absorption spectrum of perovskite materials for different temperatures and is shown for a MAPI film in figure 2.7a). The behavior of MAPBr is quite similar [87]. To elucidate the temperature-dependent measurements on MAPI NPLs performed in this thesis, the behavior of MAPI films is discussed in the following. With decreasing temperature, a peak emerges which can be attributed to an excitonic transition. This peak initially shows, as expected, a bathochromic shift. However, at 170 K a second peak arises. The second peak gains in intensity and shifts to lower energies. The emergence of the second peak can be assigned to a structural phase transition from the tetragonal to the orthorhombic phase with both phases coexisting for a small temperature range. This is one of the known phase transitions in MAPI. An overview of the phase transitions present in MAPI at different temperatures is given in table 2.1. Figure 2.7b) illustrates the phase transition and the accompanying change of the band gap energy measured for MAPI films. Jumps of the absorption onset and PL peak are recorded, visualizing the effect of the orthorhombic-to-tetragonal and the tetragonal-to-cubic phase transition. Examples of the temperature dependence of the PL intensity can be found in literature [89, 90].

In the case of MAPI, or any other MA^+ consisting perovskite material, the role of MA^+ is crucial for understanding the processes during the phase transitions. The higher

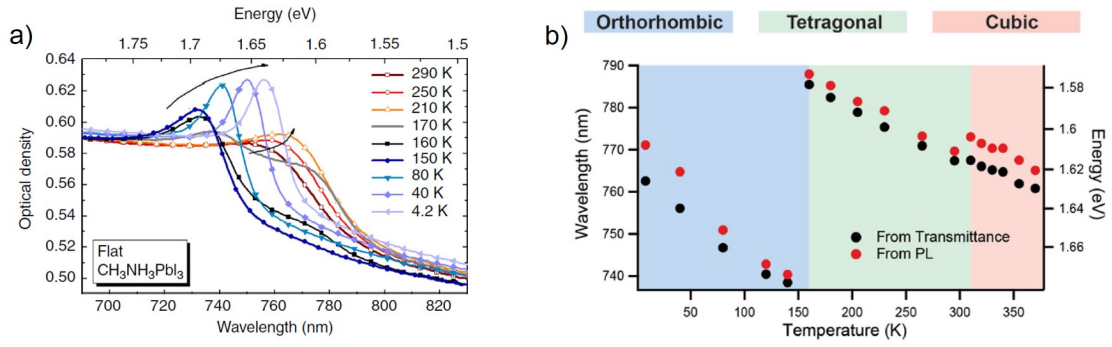


Figure 2.7: Temperature-dependent absorption and PL measurements of MAPI films.

a) Temperature-dependent absorption spectrum, which exhibits a red-shift with decreasing temperature. Furthermore, a strong change in absorption is observed at roughly 160 K, the position of the tetragonal-to-orthorhombic phase transition. The figure is taken from D’Innocenzo et al. [85]. b) The position of the absorption band edge and the PL peak are shown as a function of temperature. The coloring is assigned to the different structural phases with blue: orthorhombic, green: tetragonal and red: cubic, respectively. This figure is taken from Milot et al. [86]

Structural phase and symmetry	Transition temperature (K)	Lattice parameter (Å)
cubic (Pm-3m)	$327.4 \leq T$	$a = 6.28$
tetragonal (I4/mcm)	$162.2 \leq T \leq 327.4$	$a = 8.85, c = 12.44$
orthorhombic (Pnma)	$T \leq 162.2$	$a = 8.84, b = 12.58,$ $c = 8.56$

Table 2.1: Phase transition temperatures and lattice parameters for MAPI [88].

the temperature the more the MA⁺ is able to move and ergo affects the crystal structure. At temperatures roughly above 330 K, MAPI is in the cubic phase and the MA⁺ molecule can rotate freely in the network of [PbI₆]⁻⁴ octahedra. While cooling the rotation is reduced and the MA⁺ molecule starts to hop between stable configurations. This describes the situation in the tetragonal phase. A second phase transition from tetragonal to orthorhombic phase is observed at roughly 160 K. In the orthorhombic phase the crystal is structured such that the MA⁺ is fixed and cannot move anymore [56, 91]. In figure 2.8 the crystal structures adopted by MAPI at different temperatures and corresponding phases are illustrated. For perovskites containing the smaller and spherical Cs⁺ atoms instead of MA⁺ molecules one observes a phase transition at much higher temperatures (up to 560 K [93]).

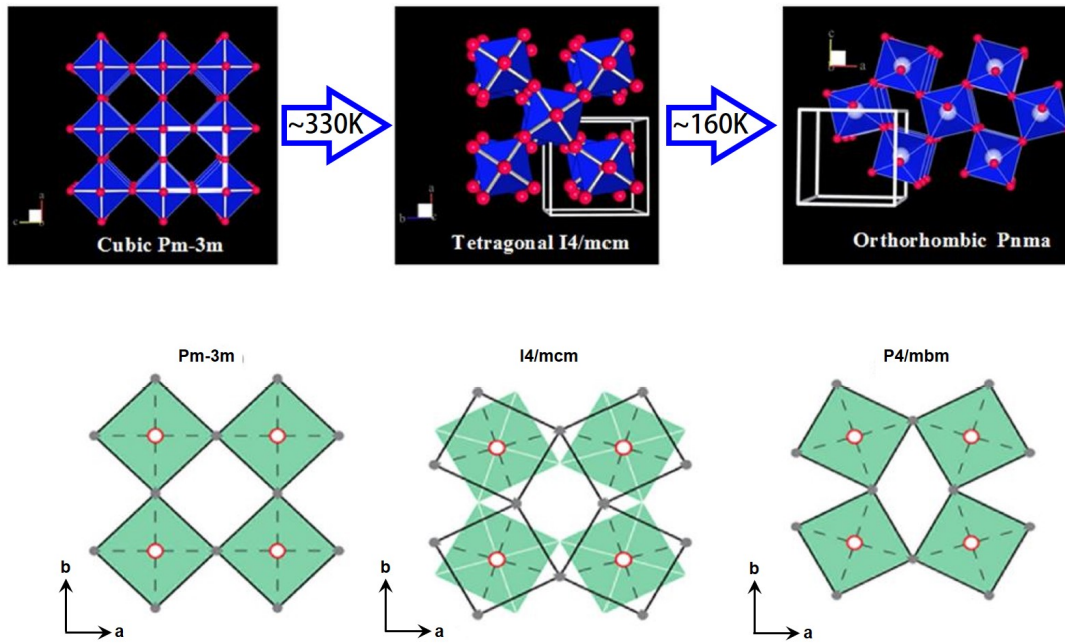


Figure 2.8: Crystal structure of different phases of MAPI. In the top illustration the $[\text{PbI}_6]^{-4}$ octahedra are painted in blue and the iodide ions are displayed in red. In the schemes at the bottom the rotations of neighboring PbI_6 layers relative to each other are exemplified. The figure is adopted from Whitefield et al. [92].

The rigid rotations of the $[\text{PbI}_6]^{-4}$ octahedra are a central element of the phase transitions. The corner-sharing octahedra can only be rotated out-of-phase in directions perpendicular to the rotation axis, but only in-phase or out-of-phase parallel to it. In the cubic phase the octahedra are perfectly aligned. By an out-of-phase rotation the tetragonal phase is implemented. The octahedra are along the c -axis in planes next to each other and rotate in opposing directions (compare figure 2.8). A further reduction of the temperature leads to the tetragonal-to-orthorhombic phase transition. This time the rotation is in-phase and the octahedra rotate in the same direction. Understandably the structural phase of the material affects its charge carrier dynamics, like it is reported for MAPI films [86].

2.1.5 Free carriers versus excitons

In the section 2.1.3, photoexcitation, which creates an electron in the CB and leaves a hole in the VB, was discussed. In these considerations the Coulomb interactions were not included, and the one-particle picture was used. Since electron and hole are electrically

charged, they interact electrostatically. The attractive interaction between electron and hole results from the Coulomb potential,

$$U(r) = -\frac{e^2}{2\pi\epsilon_0\epsilon r}, \quad (2.8)$$

where r is the distance of electron and hole and ϵ is the dielectric constant of the material. A strong Coulomb interaction leads to the formation of a bound electron-hole pair, known as an exciton. This section will deal with excitons and free carriers and their role in perovskites. Subsequently, the dynamics of excitons and the impact of quantum confinement on excitonic effects are discussed in more detail.

Excitons can be formed either by direct photoexcitation or by association of free charge carriers. Vice versa, excitons formed by photoexcitation can dissociate into free carriers. In a simple picture, an exciton can be seen as a hydrogen-like bound pair of charges with an internal energy slightly lower than the band gap energy and with an effective mass depending on the material. In solids there are two basic types of excitons, the Wannier-Mott exciton (also called 'free exciton') and the Frenkel exciton (also called 'tightly bound exciton'). In figure 2.9, the different principles of Wannier-Mott and Frenkel excitons are shown.

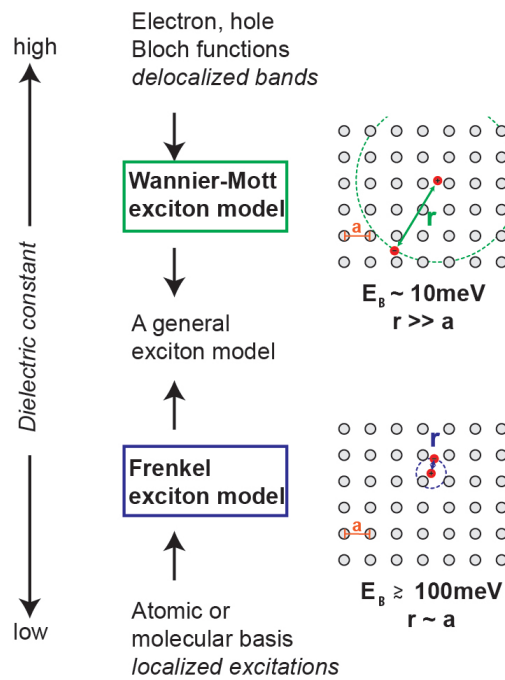


Figure 2.9: Wannier-Mott and Frenkel exciton model. Scheme to sum up the basics of excitons, highlighting the differences of Wannier-Mott and Frenkel excitons. The illustrated figure is based on Scholes et al. [94].

For Wannier-Mott excitons, the average separation of the electrons and holes is much larger than the atomic spacing and the exciton wavefunction is strongly delocalized. It is also called 'free exciton' since the electron-hole pair is weakly bound and the quasi-particle can move freely inside the crystal. If the separation of electron and hole is large enough, one can assume that the exciton is moving in a material with an uniform dielectric constant. Using effective masses, the free exciton can be modeled as a hydrogenic system [61]. In a modified version of the Bohr model of the hydrogen atom, two factors need to be adjusted: (i) The different ratio of the effective masses and (ii) the shielding of the electrostatic force between the electron and hole by the dielectric constant of the surrounding, ϵ_0 . The binding energy of the n -th exciton level with $n = 1, 2, 3, \dots$ is given by

$$E_{B,n} = \frac{\mu e^4}{32\pi^2 \epsilon^2 \hbar^2 n^2} = \frac{\hbar^2}{2\mu a_B^2 n^2}, \quad (2.9)$$

with μ the reduced mass of the exciton ($\mu^{-1} = m_e^{-1} + m_h^{-1}$), m_e and m_h the mass of the electron and hole and a_B the Bohr radius. The Wannier-Mott exciton binding energy is typically on the order of tens of meV and Wannier-Mott excitons are found in many semiconductor crystals [95]. The $n = 1$ state represents the exciton ground state, $n = 2$ the 2s exciton state, $n = 3$ the 2p exciton state and so on. Roughly speaking the exciton is stable if E_B is larger than $k_B T$ (approximately 25 meV at room temperature), otherwise collisions with phonons may dissociate the exciton. The dispersion relation of a free exciton is given by

$$E_n(\vec{K}) = E_G - E_{B,n} + E_{kin} = E_G - E_{B,n} + \frac{\hbar^2 \vec{K}^2}{2(m_e + m_h)}, \quad (2.10)$$

with \vec{K} being the exciton wavevector and $\hbar\vec{K}$ the quasi-momentum. Figure 2.10a) shows the excitation of an electron in the one-particle picture. To illustrate the exciton concept, the two-particle picture (compare figure 2.10b)) is used and the light line is depicted as

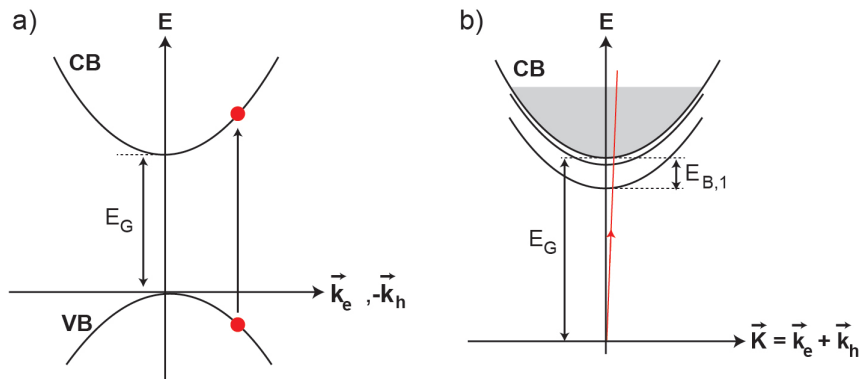


Figure 2.10: Excitation of an electron-hole pair in a) one particle picture with VB and CB
b) in the exciton two particle picture (after Klingshirn [96]).

well. Interactions between photons and excitons are only possible, where the two dispersion relations intersect.

Frenkel excitons are typically found in alkali halide crystals and molecular materials. In these materials the dielectric constant is very low and therefore the screening is only weak resulting in a high exciton binding energy and a small Bohr radius [95]. Consequently, in contrary to the Wannier-Mott excitons, Frenkel excitons cannot freely move inside a crystal, but are limited to a hopping mechanism. They have a smaller radius and are localized at a specific atom or molecule. Since Frenkel excitons represent localized excitation they cannot be described in the effective mass approximation [94].

The roles of excitons and free carriers in perovskites have been discussed in many publications [21, 24, 85, 97–99]. Up to date there are diverse opinions about their roles in the performance of this material and the reported E_B values vary widely. In the case of MAPI, these values range from roughly 2 to 55 meV [100], whereby many different experimental techniques were used to determine them. A few examples are summarized in the review of Herz [77]. The excitons in methylammonium lead halide perovskites can be describe using the Wannier-Mott model [101, 102].

At low temperatures the absorption spectra of MAPbX_3 ($X=\text{I, Br, Cl}$) clearly show excitonic effects, whereas at room temperature the situation is not as clear. In general, semiconductors with a larger band gap display stronger excitonic features due to a reduced background screening. In accordance to that, MAPCl and MAPBr show increased excitonic behavior compared to MAPI [103]. In MAPbX_3 films free carriers and excitons coexist, with the ratio of the two populations depending on the halide ion. For the case of MAPI time-resolved spectroscopy experiments have been used to show that after photoexcitation, free carriers are dominant [104–106].

2.1.6 Lead halide perovskite nanocrystals (2D)

The properties of lead halide perovskites above presented are based on measurements performed mainly on films. In the following section the development regarding the research on 2D NCs of this material is thematized. The first colloidal stable synthesis of lead halide perovskites was conducted in the year 2014 by Schmidt et al. [15]. Several research groups adopted the synthesis, however, a control of the size and shape of the NCs was not achieved. In 2015 the formation of 2D lead halide perovskite NPLs showing excitonic features attributed to quantum confinement and a corresponding blue-shift of the photoluminescence was reported [107]. Shortly afterwards in the work of Sichert et al., which was conducted at the same chair and in parallel to this thesis, individual PL maxima were assigned to NPLs of incremental thickness [37]. By a systematic modification of the organic

ammonium cations with alkyl chains of different lengths, namely octylammonium (OA) and methylammonium (MA), the thickness of the NPLs is varied. Since the OA is too large to fit in the perovskite crystal structure a self-termination of the crystal growth is attained. In figure 2.11a) the absorption and PL spectra of MAPBr NPLs with successively decreasing thickness is illustrated. Furthermore, in figure 2.11b) a scheme of the corre-

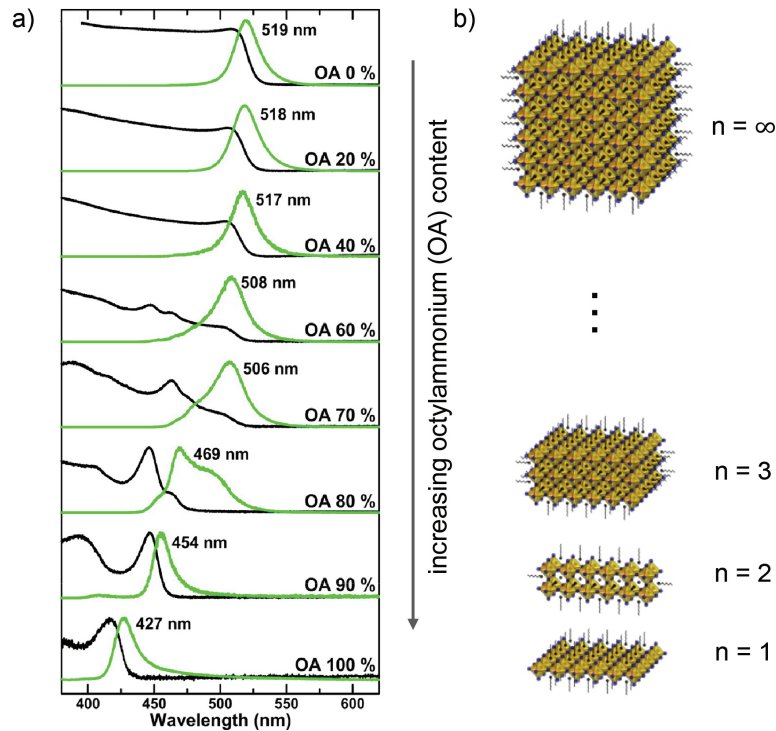


Figure 2.11: MAPBr NPLs of different thickness. a) Absorption and PL spectra. By increasing OA to MA ratio the thickness of the platelets is successively reduced, shown on the schematic picture in b). Figure adopted from Sichert et al. [37].

sponding NPLs with a different number of layers (n) is shown. A shift of the absorption onset and the PL maximum is recorded. This shift is induced by quantum size effects and the appearing PL peaks can be assigned to NPLs with different thicknesses. These experimental findings are confirmed through quantum-confinement calculations.

Figure 2.12 depicts electron microscopy images of the synthesized NPLs. As observed in the scanning electron (SEM) and transmission electron microscope (TEM) images, the prepared NPLs tend to stack together. In the calculation the observed stacking is considered by applying the one-band effective-mass Kronig-Penney model. According to Sichert et al. [37] the exciton binding energy of very thin NPLs is in the range of several hundreds of meV. However, a more precise determination of the exciton binding energy and analysis of the quantum size effects was not possible. This required a separation of the lead halide perovskite NPLs according to their thickness. In the presented thesis the preparation of dispersions of lead halide perovskite NPLs with certain thicknesses is reported. This

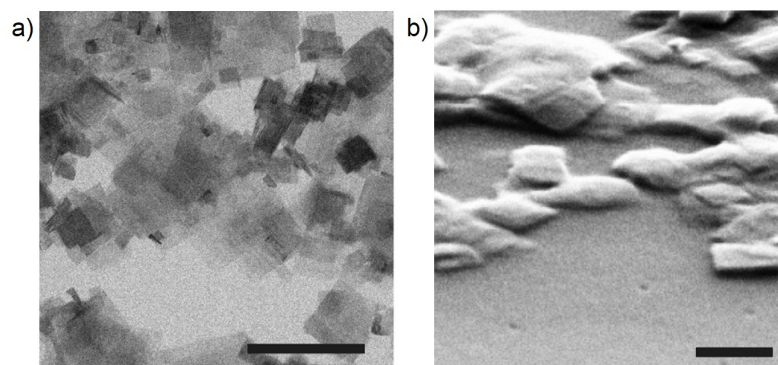


Figure 2.12: Electron microscopy images of thin lead halide perovskite NPs. The images are adopted from Sichert et al. [37] and illustrate the a) TEM and b) SEM images of samples with a high OA ratio (80%). The scale bar in each image corresponds to 200 nm. The obtained NPs are very thin but not uniform in thickness and are stacked together.

enormous achievement enables the thickness-dependent investigation of carrier dynamics in 2D and 3D lead halide perovskite NPs, presented in chapter 6.

2.2 Reduced dimensionality: From 3D to 2D

So far mainly the behavior of 3D semiconductors was described, assuming an infinite crystal size. The simplification of an infinite expansion is invalid for thin NPLs. If the size of the crystal is reduced, the electrons and holes are locally restricted by the boundaries of the crystal making quantum confinement effects important.

2.2.1 Quantum confinement

If the size of a nanocrystal is in the range of the wavefunction of the electron, quantum size effects need to be considered. In this range the electron is affected by the boundaries and potential barriers of the nanocrystal and its energy levels are shifted. As a result of quantum size effects the band gap is increased, causing a blue-shift in absorption and PL, and in the formation of discrete energy levels instead of continuous energy bands. A nanocrystal can be confined in zero, one, two or three dimensions, resulting in a 3D (bulk), 2D (quantum well), 1D (quantum wire) or 0D (quantum dot) structure, respectively. By reducing the dimension of the nanostructure the DOS of the electrons naturally changes. Figure 2.13 illustrates the density of states for electrons in a 3D, 2D, 1D and 0D semiconductor nanostructure. A change in the DOS of the electrons will of course influence the

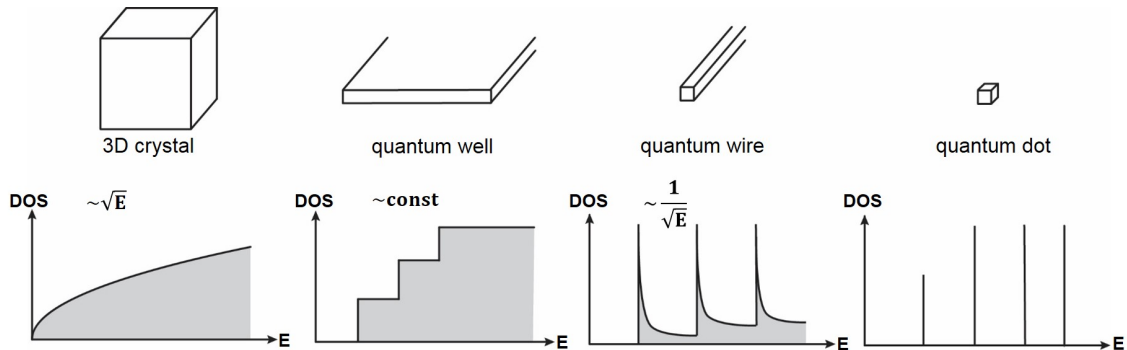


Figure 2.13: Density of states of electrons for a 3D crystal, a quantum well (2D), a quantum wire (1D) and a quantum dot (0D). Illustration according to Zhang and van Roosemalen [108].

absorption spectrum.

In the case of a confinement in one direction, one obtains a 2D nanostructure. The easiest model to describe the impact of quantum confinement is to use the ideal case of an electron restricted in a potential with infinite potential barriers [109]. With the assumption of confinement in the z-direction and an electron that can freely move in the 2D x-y plane, the obtained energy dispersions for the conduction (E_c) and valence band (E_v) can be described accordingly:

$$E_c(k) = E_G + \frac{\hbar^2}{2m_e} (k_x^2 + k_y^2) \quad (2.11)$$

$$E_v(k) = E_G + \frac{\hbar^2}{2m_h} (k_x^2 + k_y^2) \quad (2.12)$$

By solving the Schrödinger equation (2.13) one obtains the eigenenergy levels E_n given in equation (2.14) [110].

$$H\Psi_n(z) = \left(-\frac{\hbar^2}{2m_{e,h}} \frac{\partial^2}{\partial z^2} \right) \Psi_n(z) = E_n \Psi_n(z) \quad (2.13)$$

$$E_n = \frac{\pi^2 \hbar^2}{2m_{e,h} L^2} n^2 \quad (2.14)$$

$m_{e,h}$ is the effective mass of the electron or hole and L represents the thickness of the 2D system. While this approach assumes a potential well with infinitely high energetic barriers, a more realistic approach would consider a finite potential barrier instead. Once again the Schrödinger equation must be solved numerically to determine the wavefunction and the energy eigenvalues.

2.2.2 Optical absorption in 2D materials

As discussed in section 2.1.5, excitons, bound states between electrons and holes, are formed due to their Coulomb interaction. The created bound states can be modelled as a hydrogen-like system and using the Elliott equation one can calculate their absorption including the excitonic impact on the semiconductor. Within Elliott's theory single particles states form the basis of the pair states with an envelope function expressing the pair correlation. The motion of the exciton can be split into the motion of the center of mass and the relative motion of the electron-hole pair. This approximation is valid for Wannier-Mott excitons only and can be used to extract the exciton binding energy and band gap energy of a material (compare section 5.1.2). In order to show the impact of the reduced dimensionality on the absorption spectra of a semiconductor, the theoretical absorption according to the Elliott formula is presented for the 3D and 2D case. In general the absorption coefficient $\alpha(\omega)$ is identified with the imaginary part of the dielectric constant ϵ_2 , given by [110]:

$$\alpha(\omega) = \frac{\omega \epsilon_2}{c \eta(\omega)}, \quad (2.15)$$

with $\eta(\omega)$ equal to the index of refraction.

In the 3D case the Elliott formula is given by:

$$\begin{aligned} \alpha_{3D}(\hbar\omega) = & \left[A \cdot \Theta(\hbar\omega - E_G) \cdot D_{CV}^{3D}(\hbar\omega) \right] \cdot \left[\frac{\pi x e^{\pi x}}{\sinh(\pi x)} \right] \\ & + A \cdot E_B \sum_{n=1}^{\infty} \frac{4\pi}{n^3} \delta\left(\hbar\omega - E_G + \frac{E_B}{n^2}\right) \end{aligned} \quad (2.16)$$

where A is a constant related to the transition matrix, Θ is the Heaviside step function and D_{CV}^{3D} represents the joint density of states in the 3D case. x is given by

$x = \left(E_B (\hbar\omega - E_G)^{-1}\right)^{1/2}$ [111]. In the first term of the sum, the absorption of the continuum is described by the joint density of states and the Sommerfeld factor (SF) for 3D materials ($\left[\frac{\pi x e^{\pi x}}{\sinh(\pi x)}\right]$). The density of states of electrons in the 3D case is proportional to $\sqrt{\hbar\omega - E_G}$, as shown in (figure 2.13). The Sommerfeld factor takes into account the absorption enhancement due to the Coulomb interaction and is given by:

$$SF = \frac{\alpha_{Coulomb}}{\alpha_{free}}, \quad (2.17)$$

the ratio of absorption coefficient inclusive Coulombic interaction $\alpha_{Coulomb}$ and the free-particle absorption α_{free} . The second term in equation (2.16) is attributed to the excitonic absorption. The oscillator strength in a 3D system is proportional to n^{-3} , with n being the energetic level of the exciton.

For the 2D case, the Elliott formula needs to be modified, using the 2D hydrogen-like model [112]. The absorption of a 2D material according to Elliott is given by:

$$\begin{aligned} \alpha_{2D}(\hbar\omega) = & \left[A \cdot \Theta(\hbar\omega - E_G) \cdot D_{CV}^{2D}(\hbar\omega) \right] \cdot \left[\frac{e^{\pi x}}{\cosh(\pi x)} \right] \\ & + A \cdot E_B \sum_{n=1}^{\infty} \frac{4\pi}{\left(n + \frac{1}{2}\right)^3} \delta\left(\hbar\omega - E_G + \frac{E_B}{4 \cdot \left(n + \frac{1}{2}\right)^2}\right). \end{aligned} \quad (2.18)$$

In figure 2.14 a drawing of the theoretical absorption of a 2D and 3D semiconductor according to Elliott is shown. The calculated absorption spectrum for the 3D case is

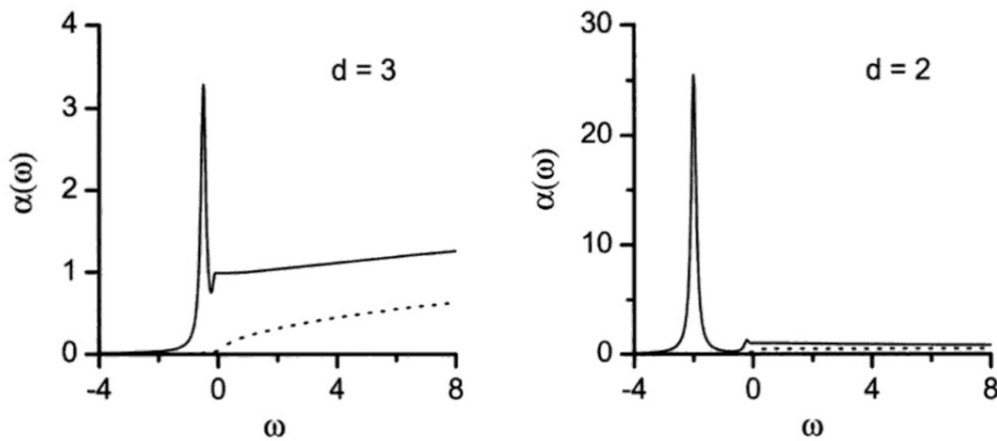


Figure 2.14: Absorption spectra according to the Elliott formula. The calculated absorption spectrum for 3D ($d=3$) and 2D ($d=2$) semiconductors according to the Elliott formula. The solid line (dotted line) is the absorption with (without) Coulomb interaction and corresponding Sommerfeld enhancement. The figure is taken from a book written by Stephan Glutsch [113].

depicted on the left. The dotted line shows the absorption without taking into account

the Coulombic interactions and the related Sommerfeld enhancement. In this case the absorption spectrum is essentially shaped by the energy-dependent density of state which shows a dependence of the root of the energy in 3D (compare figure 2.13). The solid line corresponds to the calculation based on equation (2.16). A peak is observed at ω smaller than zero, followed by a steady increasing plateau with an absorption coefficient roughly one third of the peak maximum. The peak can be assigned to the excitonic ground state and according to equation (2.16) further excitonic peaks ($n= 2, 3, 4, \dots$) are considered. These excitonic peaks for $n > 1$ decreases with the oscillator strength proportional to n^{-3} and are not visible in the graph. The Coulomb interactions are accounted in the calculation of the absorption of the continuum by applying the Sommerfeld factor and result in a strong enhancement of the absorption. Analogous, the absorption of the 2D case is calculated according to the Elliott formula (2.18). The strength of the excitonic peak compared to the continuum is enhanced and moreover the shape of the continuum is changed. According to the formulas (2.16) and (2.18) the absorption area of the exciton is increased by a factor of four for 2D compared to 3D [114]. Since the density of states in 2D shows a stair-case behavior, the continuum absorption appears flatter.

As already mentioned, in this work a successful separation of lead halide perovskite NPLs according to their thickness is achieved. Thus, a detailed study of the quantum confinement and associated effects on optical properties is possible. Furthermore, time-resolved spectroscopy can be performed to investigate the carrier lifetimes and relaxation dynamics in 2D and 3D lead halide perovskite NPLs.

2.3 Ultrafast optical phenomena

The optical properties of lead halide perovskites or other semiconductors are determined by their charge carrier dynamics. To obtain a better insight into those, time-resolved spectroscopy is a helpful tool [115]. Especially relaxation but also recombination processes are analyzed by a pump-probe experiment by recording the nonlinear response of a semiconductor. Moreover, time-resolved PL can be applied to study recombination processes as well. Both methods are used in this thesis to investigate the carrier dynamics in lead halide perovskite NPIs. Details on the working principle of the used setups are given in the experimental methods chapter, section 3.2.2. In order to support the interpretations and discussions presented in chapter 6, ultrafast optical phenomena observed in time-resolved spectroscopy measurements are summarized in the following.

2.3.1 Carrier relaxation regimes

In an optical pump-probe measurement the investigated material is optically photoexcited with a first laser pulse (pump) and subsequently, after a certain time delay, probed with a second pulse (probe). Following the photoexcitation, the relaxation of charge carriers can be separated into several phases. These phases are temporally overlapping, but can be roughly divided into four regimes [116]. A graphical representation of these regimes is depicted in figure 2.15. In this figure typical scattering and relaxation processes for the different regimes and corresponding experimentally determined time scales for MAPI films, according to Flender et al. [117], are given.

Directly after photoexcitation, the charge carriers are in a well-defined phase relation to the electromagnetic field created by the excitation, in the so called coherent regime. In semiconductors carrier-carrier scattering processes, which destroy the coherence, are extremely fast and normally within a few hundred femtoseconds the coherence is lost [115]. The next prevalent regime is the non-thermal regime. Here, the distribution of the highly energetic carriers is non-thermal, meaning it cannot be described by a temperature. Charge carriers thermalize with each other e.g. through carrier-carrier scattering leading to a hot thermal distribution. Hot in this sense refers to their elevated temperature with respect to the atomic lattice. Through emission of phonons the hot carriers cool down until an equilibrium with the lattice is reached. Investigations of the hot-carrier regime address the thermalization of these carriers and give greater information on carrier-phonon, exciton-phonon and phonon-phonon interactions. The cooling behavior of 2D and 3D lead halide perovskites is discussed in section 6.1.4 and thereby compared to other 2D and 3D

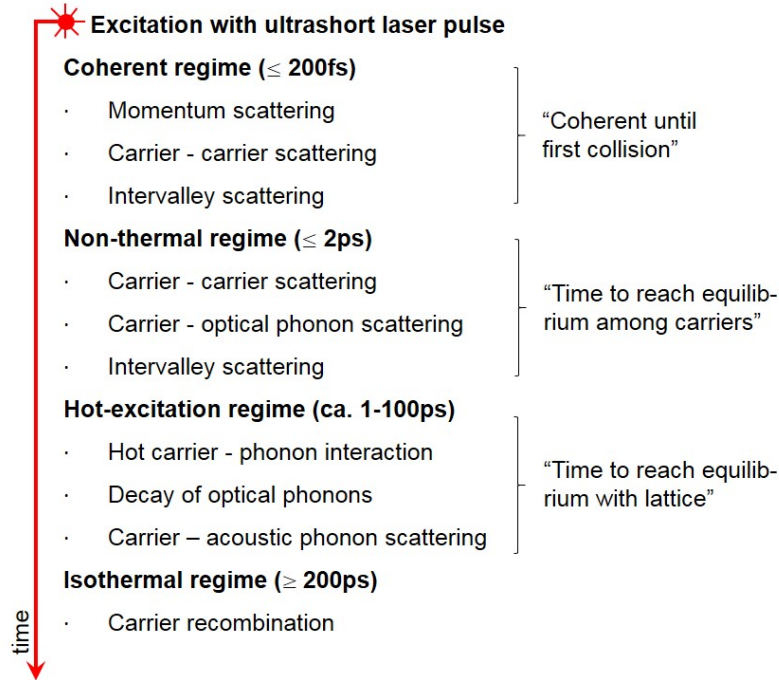


Figure 2.15: Relaxation time regimes for semiconductors. The scheme is based on Shah [116]. The four different regimes partly overlap. The given timescale is measured for MAPI films and presented in the work of Flender et al. [117].

semiconductor nanostructures. In the last of the four regimes, the isothermal regime, the recombination of the charge carriers takes place.

2.3.2 Recombination dynamics

In the isothermal regime the electron and hole recombine. Analyzing recombination kinetics helps to learn more about the role of excitons and free charge carriers in the system. The different recombination mechanisms, which all depend on the concentration of charge carriers, are shown in figure 2.16. The recombination dynamics is usually described by the following equation (2.19):

$$-\frac{dn}{dt} = k_1n + k_2n^2 + k_3n^3 \quad (2.19)$$

In the equation, n represents the charge carrier density and k_i are recombination coefficients. The first-order rate constant k_1 represents the recombination of excitons or can be related to the trapping of charges. k_2 is the second-order rate constant arising from electron-hole recombination and k_3 is the contribution due to Auger recombination. The observation of monomolecular recombination is a strong indication for the formation and subsequent recombination of excitons. A viable way to rule out trap-assisted recombination is the comparison of recombination dynamics for different charge carrier densities. If the detected trend of monomolecular recombination is caused by trap states in the material,

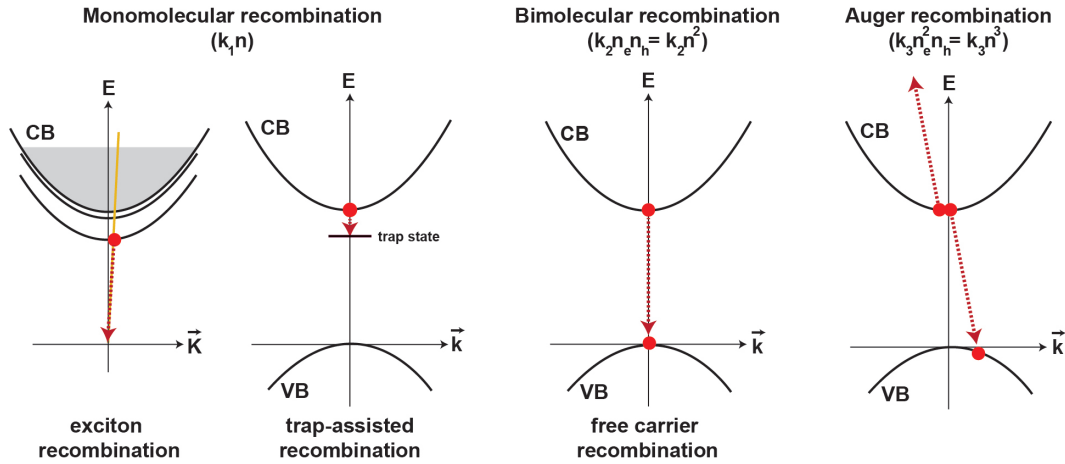


Figure 2.16: Scheme to visualize the different recombination mechanisms in a semiconductor. A monomolecular recombination can be observed either for exciton recombination or trap-assisted recombination. As described in section 2.1.5 the two particle picture is used for excitons and the one particle picture for free carriers. The bimolecular recombination describes the recombination of free carriers. The Auger recombination is illustrated as well. The dependence on the electron density n_e and hole density n_h is given for the case shown in the scheme.

at sufficient high densities the impact of these states is diminished, since a saturation is reached. The second term in equation (2.19), which describes the bimolecular recombination of free carriers, depends on the density of the two different charge carriers. Regarding photoexcitation of a not highly doped semiconductor, one can assume that the density of electrons and holes is approximately the same, consequently, the recombination rate is proportional to n^2 . The Auger recombination, considered in the third term, is a nonradiative three-carrier interaction ($\propto n^3$) and depends a lot on the charge carrier density and can be neglected for sufficiently small carrier densities [118–121]. For semiconductors the probability of Auger recombination is linked to the electronic band structure of the material, since energy and momentum conversion need to be fulfilled for all charges included in the process [122].

A distinction between the different recombination mechanisms is important. Understanding the origin of the recombination helps to further handle the analysis regarding charge carrier dynamics and to improve specific applications. In the case of MAPI films, studies on the charge carrier recombination have been performed, showing that the recombination is mainly dominated by bimolecular recombination, indicating the prevalent role of free charges in MAPI [105]. In chapter 6 of this thesis the charge carrier recombination in MAPI NPIs is analyzed in more detail.

2.3.3 Nonlinear optical response of semiconductors

Transient absorption measurements performed with a pump-probe setup can greatly contribute to obtain a better understanding of semiconductors by providing fundamental information about nonequilibrium and nonlinear properties of these materials. The dynamics are determined in such an experiment by the coherent and incoherent response of the system to photoexcitation. The three most important microscopic effects in the incoherent regime are:

- Phase space filling
- Screening of the Coulomb interaction
- Band gap renormalization (BGR)

In general, these coupled effects are important for the interpretation of the results of transient absorption spectroscopy measurements. Therefore, those are explicitly mentioned and shortly explained in the following.

One needs to consider that charge carriers are fermions. Consequently, the Pauli exclusion principle is valid [61, 123]. According to this principle, only optical transitions into unoccupied states are possible. For the case of a direct semiconductor with free carriers generated through photoexcitation, the change in the absorption coefficient is given by equation (2.20), by only considering phase space filling.

$$\Delta\alpha(\hbar\omega) = (1 - f_e - f_h) \alpha_0(\hbar\omega) \quad (2.20)$$

f_e and f_h are the photoexcited electron and hole distribution functions at energy E_e and E_h coupled by the photon energy $\hbar\omega$. Because of the Pauli blocking the increase of charge carrier density leads to a progressive filling of higher energetic states and a shift of the absorption onset is recorded. In section 6.1.2 the effect of phase space filling on MAPI NPLs observed in transient absorption spectroscopy (TAS) measurements is studied.

Furthermore, changes of the absorption of semiconductors are induced by the screening of photoexcited carriers. To take this effect into account one can introduce an additional dielectric constant ϵ [124]. Using ϵ , the screened Coulomb potential (U_{screen}) is expressed by:

$$U_{screen}(\vec{k}) = \frac{U_{non-screen}(\vec{k})}{\epsilon(\vec{k}, \omega)} \quad (2.21)$$

The third listed microscopic effect, also observable in the TAS spectra, is band gap renormalization. It is a many-body effect and describes the induced renormalization of the band gap and is attributed to mutual exchange and Coulomb interactions between

the added photoexcited carriers [110]. Due to the presence of other carriers, the VBM is increased and the CBM is decreased [125] and a red-shift of the ground state bleach can be observed in the TAS measurements.

The thesis is structured as follows: After this chapter regarding the fundamentals, the experimental methods, used to obtain the presented and discussed results, are introduced. The fabrication and separation of lead halide perovskite NPLs with individual thicknesses applying a top-down synthesis approach, namely ligand-assisted exfoliation, is reported for the first time and is the fundamental requirement for all further investigations. Dispersions of lead halide nanoplatelets of one certain thickness are used to analyze the quantum confinement-induced shift of the band gap and exciton binding energy. According to the Elliott formula the exciton binding energy of MAPI NPLs with individual thicknesses is determined. The control of size and composition in the preparation of the lead halide perovskite NPLs, allows to tune the band gap over the whole visible spectrum. Temperature-dependent measurements on 2D and 3D NPLs indicate a thickness-dependent shift of the phase transition temperature. Additionally, the carrier dynamics, analyzed in time-resolved spectroscopy experiments depend on the thickness of the platelets. Both, the filling of the states and the recombination mechanisms indicate that in 3D NPLs free carriers and in 2D NPLs excitons are dominant. Moreover, in this thesis the cooling behavior of 2D and 3D lead halide perovskite NPLs is examined and compared for the first time. The obtained cooling time for the 2D is much faster than for the 3D case, contrary to observations made for other semiconductor NCs. Furthermore, it is demonstrated that the photoluminescence lifetime decreases with a decreasing number of layers which is related to the increasing exciton binding energy.

Experimental methods

In the first part of this chapter the methods used in this work to analyze and characterize perovskite nanocrystals are introduced. The structure and composition of the prepared nanocrystals were characterized by using different electron microscopy methods, atomic force microscopy and X-ray diffraction. Additionally, optical properties were examined in more detail via steady-state and time-resolved measurement methods. To perform time-resolved measurements, a pump-probe setup and a streak camera were used. Furthermore, temperature-dependent PL measurements were performed using a cryostat, capable of cooling to temperatures below 10 K. The second part of this chapter deals with the synthesis of the nanoparticles, which is explained step by step. Ligand-assisted exfoliation, a well-known method for producing nanostructures, was applied for the first time to fabricate perovskite nanoplatelets. This method is capable of producing perovskite nanocrystals of different size, shape, and composition.

3.1 Structural and compositional analysis

Different techniques can be utilized to characterize and analyze the structure and composition of materials. Working with nanocrystals, these investigations can be quite challenging due to their extremely small sizes. In this section different methods and setups, which were used for this purpose in the scope of this work, are introduced.

3.1.1 Electron microscopy

In general, small objects can be investigated using a broad range of microscopy methods. Among these, the most fundamental one is the light microscope. It was already developed in 1590. A light microscope provides a resolution (ρ) of roughly $0.2\ \mu\text{m}$ and is restricted by the Abbe limit [126]:

$$\rho = \frac{\lambda}{\eta \sin(\alpha)}, \quad (3.1)$$

with η the refractive index of the lenses, α the illumination semi-angle and λ the wavelength of the light. In order to improve the resolution, electrons are often used. According to Louis de Broglie the wavelength of electrons is substantially smaller than the wavelength of visible light and is given by [127]:

$$\lambda_e = \frac{h}{p_e} = \frac{h}{m_e \cdot v_e} = \frac{h}{\sqrt{2m_e e U_b}}, \quad (3.2)$$

with p_e , m_e , v_e and e are the momentum, mass, velocity and charge of an electron, respectively. U_b is the applied acceleration voltage and h the Planck constant. Hence, applying the Abbe limit, employing electrons for microscopy can push the Abbe limit down to $0.5\ \text{nm}$.

Scanning electron microscopy

In this work, the structural properties and the surface of lead halide perovskite NCs were investigated using two different electron microscopes. In figure 3.1 the working principle of a scanning electron microscope (SEM) is illustrated in comparison to a transmission electron microscope (TEM) and a light microscope. First, electrons are generated in a field emission gun, where a high electric field extracts electrons from a sharply pointed tip. These electrons are subsequently accelerate in the applied electric field. To focus and define the electron beam, electromagnetic lenses are employed. A beam deflector deviates the focused electrons, in order to scan the surface of the sample step by step. When reaching the sample, electrons are scattered elastically and inelastically and subsequently detected by the InLens and the SE2 detectors. The InLens detector is a rotationally symmetric ring detector around the optical axis and records secondary electrons, which are ionized

by scattering processes with other electrons. It is especially sensitive to differences in the working functions of sample material components. The SE2 detector collects secondary electrons as well, yet it is placed at a higher angle in respect to the gun. In contrast to the InLens detector, it is particularly useful for resolving topographic information.

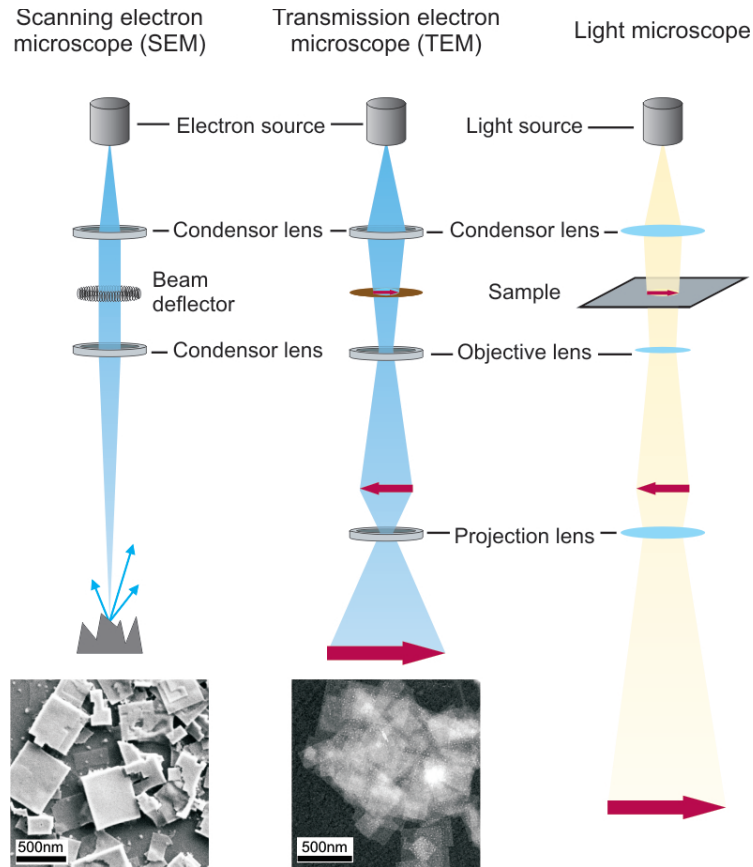


Figure 3.1: Working principle of a SEM and TEM compared to a conventional light microscope. In contrast to light microscopy, where imaging is based on conventional optics, electron microscopy employs electron optics for imaging. For example, instead of using glass lenses, electron microscopes use electromagnetic lenses to manipulate the electron beam. Additionally images of perovskite nanostructures obtained via TEM and SEM are shown.

However, some of the electrons interacting with the specimen do not leave the sample. Therefore, the sample gets charged during illumination. The amount of charging varies mainly based on material-dependent properties of the sample. This residual charge then interacts with the electrons from the gun, distorting the images created. To avoid local charging of the surface and concomitant artifacts, a non-conductive sample is usually coated with a thin layer of metal or carbon. In this process, mainly silica and glass substrates were used for the sample preparation. Routinely nonconductive substrates are sputtered (Sputter Coater EM SCD005, Leica) with a roughly 3 nm thick gold palladium layer. All SEM images presented in this work were made with a field emission SEM

(Gemini Ultra Plus Field Emission Scanning Electron Microscope, Zeiss) having a nominal resolution of 2 nm. To record images, a working distance of 3 - 4 mm and an acceleration voltage of 2 - 4 kV was chosen.

One challenge of scanning electron microscopy is that the accelerated electrons affect the sample and may lead to degradation or carbon deposition. Due to the interaction with the electron beam, optical and also electric properties of the sample may be affected. In the case of perovskite nanoplatelets a strong degradation under the electron beam was observed. This issue is addressed later in section 5.2. Hence, imaging with electron microscopy methods was always performed after analytical measurements and sample characterization procedures.

Transmission electron microscopy

Similar to scanning electron microscopy, transmission electron microscopy is based on electron optics. The setup of a TEM is schematically shown in figure 3.1. In principle it is much more comparable to a conventional light microscope than an SEM. Instead of a light source, an electron gun is used and the glass lenses are replaced by electromagnetic lenses. In contrast to an SEM, a TEM is suitable for examining the internal structure of a sample. TEM images display a sample as a whole and provide a higher resolution than SEM images. To visualize a sample by transmission electron microscopy, electrons have to be transmitted through the sample. Consequently, the sample may not be thicker than roughly 100 nm. In this work the TEM (JEM-1011, JOEL) provided by the group of Prof. Dr. Joachim Rädler is operated with an acceleration voltage of 80 kV. The resolution is approximately 1 - 3 nm and copper grids covered with a holey carbon film were used for sample deposition.

High-resolution transmission electron microscopy

To perform high-resolution transmission electron microscopy a large objective aperture has to be selected, enabling many beams including the direct one to pass through the sample. The electron beam, ideally represented by a plane wave, interacts with the specimen. Thus, the outgoing electron wave shows modulations of its phase and amplitude, yielding information about the object's structure. The resulting image of a high-resolution transmission electron microscope (HRTEM), formed by the interference of the diffracted beam and the direct beam, shows directly a 2D projection of the atomic structure of the specimen with a resolution of up to 0.05 nm. The obtained HRTEM images presented in this work were recorded with an HRTEM (Titan Themis, FEI) operated at an accelerating voltage of 300 kV.

Scanning electron transmission microscopy

In a scanning TEM (STEM) the principles of the SEM and TEM are combined. Similar to an SEM, the electron beam is focused on a single spot and is scanned over the sample [128]. In contrast to an SEM, and similar to a TEM, an STEM records the transmitted electrons. Using HRTEM in STEM mode, one can achieve images with a spatial resolution of up to 0.05 nm. The STEM measurements were performed with the same device as the acquisition of the HRTEM images.

Energy-dispersive X-ray spectroscopy

One can not only record the scattered electrons, but also the emitted X-rays. Accelerated electrons may kick out electrons from atomic shells - ergo ionizing them - while passing through the sample. The resulting vacancies are filled up by electrons of higher shells and, consequently, characteristic X-rays are emitted. Additionally, in order to perform a spatially resolved compositional analysis in STEM mode, one can use an energy-dispersive X-ray spectroscope (EDX) to detect these X-rays. For this thesis, a Super-X SSD detector was implemented to the HRTEM to perform EDX analysis. All HRTEM related measurements were done by Dr. Markus Döblinger at the chair of Prof. Dr. Thomas Bein.

3.1.2 Atomic force microscopy

An atomic force microscope (AFM) is a tool to investigate the surface morphology of a sample in a non-destructive fashion. Furthermore, almost any force interaction, such as van der Waals, electrical, magnetic or thermal interactions can be investigated with an AFM [129].

The general working principle of an AFM, also known as scanning probe microscopy (SPM), is based on the interaction of a thin tip with the sample. This tip of an AFM is atomically sharp and fixed to the free end of a cantilever. The beam of a laser, which is reflected off the cantilever, is recorded with a photodiode while the tip is scanned over the surface of the sample. The surface topology can then be calculated from the cantilever deflection. All AFM images presented in this work are recorded with a commercial AFM (Multimode, Bruker), equipped with a Nanoscope III controller and a type E scanner. Silicon cantilevers (AC160TS, Olympus; resonance frequency approx. 300 kHz) were used and typical scans were recorded at 1 - 3 Hz line frequency, with optimized feedback parameters and at 512 x 512 pixels. Image processing and analysis were performed with the Scanning Probe Image Processor software (v6.4; Image Metrology). For the background correction global fitting with a third-order polynomial and line-by-line correction through

the histogram alignment routine were applied. Before AFM imaging, all samples were dried under ambient conditions. The AFM measurements were performed by Dr. Willem Vanderlinden at the chair of Prof. Hermann Gaub.

3.1.3 X-ray diffraction

X-ray diffraction (XRD) is a non-destructive analytic technique to quickly investigate different properties of a crystal or quasi-crystal. This includes the crystal structure, the present phases, the crystal dimensionality and chemical bonds. In this thesis XRD is used to determine the crystal structure of the fabricated lead halide perovskite NCs.

XRD relies on the fact that X-rays, like every other electromagnetic wave, are diffracted by a grating. The diffraction is most efficient if the grating and the wavelength of the incident ray are roughly of the same size. Since the wavelength of X-rays is in the same order of magnitude as the spacing of planes in a crystal lattice, XRD enables a measurement of the properties of the crystal structure. In 1912, XRD was observed for the first time by Max Laue and some of the measurements presented in this thesis were made in the very same lab as Max von Laue made his discovery.

The structure of a crystal can be associated with the characteristic diffraction pattern of a sample measured at different angles. At certain angles the diffracted radiation is very intense. These directions correspond to constructive interferences of diffracted X-ray beams. The angles under which constructive interference occurs can be determined with Bragg's law [130].

$$n\lambda = 2d\sin\theta \quad (3.3)$$

This is also illustrated in figure 3.2. Since the wavelength of the used X-rays is known,

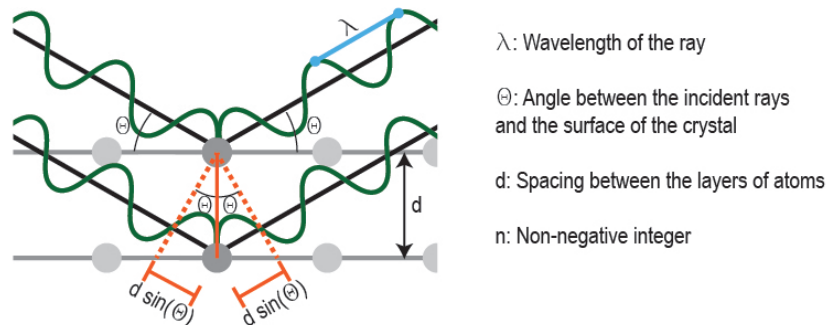


Figure 3.2: Schematic representation of X-ray diffraction and Bragg's law. Two waves are glancing off two atoms in distance d to each other. The incident angle is equal to the reflected angle. If Bragg's law (compare equation 3.3) is fulfilled, the two reflected waves are in phase and a constructive interference is observed.

Bragg's law can be used to calculate the spacing d between the atoms in the crystal structure. The recorded intensities of the peaks indicate the arrangement of the atoms and allow for a characterization of the crystal structure and an identification of the prevailing phase.

XRD measurements shown in this thesis were performed on an X-ray diffractometer (D8 Discover, Bruker) operated at 40 kV and 30 mA, employing Ni-filtered Cu K_{α} radiation ($\lambda=1.5406 \text{ \AA}$) and a position-sensitive detector (LynxEye, Bruker), which was provided by the chair of Prof. Thomas Bein. In the measurement the detector is moved in a circle around the sample and its position is recorded as 2θ .

3.2 Optical characterization techniques

There are various techniques available to characterize samples by optical means. In this thesis mainly measurements in the energy range of visible light (1.65 - 3.27 eV) were conducted. The most prominent advantages of optical characterization techniques are that they are fast to perform, generally non-destructive and almost no additional sample preparation is necessary. In the following, steady-state spectroscopy and time-resolved spectroscopy methods conducted in this work are explained.

3.2.1 Steady-state spectroscopy

Steady-state spectroscopy measures the long-term average of detected light intensities under illumination. In this work, both absorption and photoluminescence (PL) have been investigated in the range from ultra-violet to visible light (UV-Vis). In general, steady-state spectroscopy methods inquire the interaction of the sample with light by monitoring the transmitted or emitted light of a sample with respect to the wavelength.

Absorption spectroscopy

The absorption spectra at room temperature presented in this thesis were recorded with one of two spectrophotometers (Cary 5000 and Cary 60, Agilent Technologies). It is possible to measure both solutions in Quartz cuvettes or films attached to transparent substrates. In order to create the absorption spectrum, a narrow wavelength range of the light emitted by a source (for example a xenon lamp) is selected by a monochromator and directed through the sample. The excitation light interacts with the sample and the intensity of the transmitted light is recorded. The intensity of the transmitted light (T) of a sample can be read from the obtained extinction spectrum and is usually given as the optical density (OD) of a sample. The correlation of transmission and OD is given by:

$$T(\lambda) = \frac{I(\lambda)}{I_0(\lambda)} = 10^{-OD(\lambda)} \quad (3.4)$$

In the measurement the intensity (I) of the transmission of the sample is compared to a reference sample (I_0). As light propagates through matter it is absorbed and scattered, hence, the intensity decreases exponentially according to the Beer-Lambert law [131]. For the measurement it is important to have a low enough optical density to ensure only one scattering or absorption event. Otherwise the Beer-Lambert law is invalid. To express the absorption by OD , which is the logarithmic ratio of I and I_0 at a certain wavelength, is therefore reasonable.

Photoluminescence spectroscopy

In a similar way as for the absorption spectrum, the PL spectrum of a sample is recorded. Instead of detecting the transmitted light, the isotropically emitted light of the sample is collected. In order to decrease reabsorption, which would erroneously reduce the recorded PL, the determined OD in the absorption measurement should not be higher than 1.

The PL measurements shown in this thesis were conducted with commercial fluorescence spectrophotometers (Cary Eclipse, Agilent Technologies; Fluorolog 3, Horiba). The Fluorolog 3 from Horiba is equipped with an integration sphere (K-Sphere Petit, Horiba) enabling the determination of the quantum yield (QY) of the investigated sample, which is given by:

$$QY = \frac{N_{em}}{N_{abs}}, \quad (3.5)$$

with N_{em} , the number of emitted, and N_{abs} , the number of absorbed photons. The walls of the integration sphere are covered with a highly reflective coating, hence, one can measure the emission and scattering of the sample in all directions. By recording the PL spectrum of the sample and a reference sample (only the solvent in a cuvette or the substrate) the QY can be obtained. The difference of the signal at the excitation wavelength between sample and reference is proportional to N_{abs} . Moreover, N_{em} is proportional to the change of the area covered by the PL peak rise. It can be strongly reduced by reabsorption, therefore, the OD determined in the previous absorption measurement should be smaller than 0.1.

In this thesis the presented spectra are plotted as functions of either wavelength or energy. However, the emission is recorded in dependence of the wavelength by applying a monochromator. In the adjustment from the wavelength to the energy scale one has to consider this and modify the intensity, as well [132].

$$I(E) = I(\lambda) \frac{d\lambda}{dE} = I(\lambda) \frac{d}{dE} \left(\frac{hc}{E} \right) = -I(\lambda) \left(\frac{hc}{E^2} \right) \quad (3.6)$$

Temperature-dependent optical spectroscopy

The absorption and PL of a sample were measured not only at ambient conditions but also in dependence of the temperature using the setup illustrated in figure 3.3. To be able to do temperature-dependent measurements, a substrate with a good heat conductivity is prerequisite. Therefore, sapphire was used as the substrate material. To achieve thermal isolation the sample chamber is set at a pressure of 10^{-5} to 10^{-6} mbar using a turbopump (TurboDrag TMH071P, Pfeiffer Vacuum). The sample is attached to a copper cryostat

with a conductive silver lacquer (Busch). The temperature of the flow cryostat (CryoVac) is controlled by the amount of liquid helium pumped through the cryostat via a diaphragm vacuum pump (ME 4 NT, Vacuubrand) and by a heating wire.

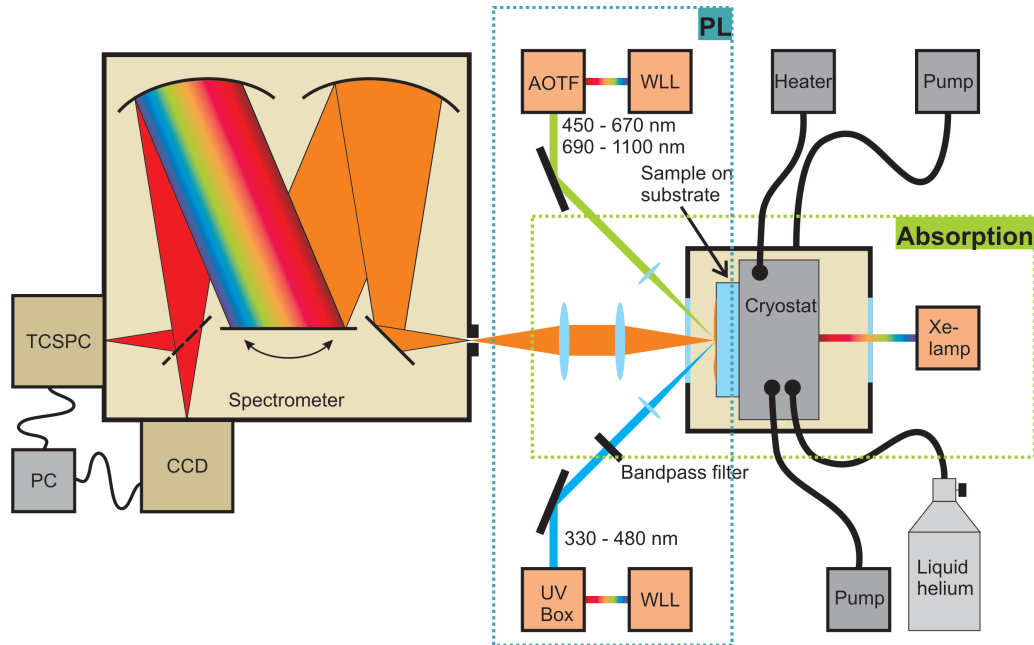


Figure 3.3: Schematic setup for temperature-dependent absorption and PL measurements. The relevant parts for the absorption measurement, besides the spectrometer, are shown in the green box. The sample is illuminated from the back by a xenon lamp and the transmitted light is guided to the spectrometer. In the green box the relevant parts for the PL measurements are shown. The beam of the white light laser reaches the sample from the front under a steep angle. Similar to the absorption measurement, the emitted light is collected like the transmitted light and directed on the spectrometer.

A xenon short arc lamp (XBO 75W/2, Osram), which is located behind the vacuum chamber, illuminates the sample to perform absorption measurements. To guarantee constant light emission, the lamp was switched on approximately one hour prior to the measurement. The transmitted light is focused by a biconvex lens on the slit of the spectrograph (Acton SpectraPro SP-2300, Princeton Instruments).

In order to do PL measurements, instead of a lamp a white light laser (SuperK Extreme EXR-20, NKT Photonics) is used. The laser beam is focused onto the sample in a high angle to avoid the direct detection of the excitation beam. The fluorescence is collected with a long distance objective. The emitted light is directed to the spectrograph in the same way as the transmitted light in the absorption measurements described above.

The signal-to-noise ratio is reduced and the reproducibility improved by recording many spectra and generating the representative average of them. Furthermore, the *OD*

of the relevant spectral region of the sample should be in a range of 0.1 to 1 to prevent systematic errors.

3.2.2 Time-resolved spectroscopy

Since the first non-tunable solid-state mode-locked lasers, a lot of progress has been made in the generation of ultrashort pulses. With the emergence of ultrafast lasers, time-resolved measurements of processes in the femtosecond range became accessible. Many techniques have been developed to investigate linear and nonlinear optical properties of materials. To be able to record ultrafast processes, a laser pulse in the same time range or faster than it has to be applied. Here, the basic working principle of transient absorption spectroscopy via a pump-probe technique, and time-resolved PL measurements using a streak camera are explained.

Transient absorption spectroscopy (pump-probe)

To use pump-probe equipment to resolve ultrashort processes has become a standard technique in the field of ultrafast spectroscopy. In such an experiment, the time resolution is only limited by the pulse width of the laser. It enables the probing and characterization of structural and electronic properties of short-lived excited (transient) states of a material. This is done as follows: Electrons absorb photons of the pump pulse and occupy energetically higher states. These electrons interact with each other, phonons and impurities leading to continuous redistributions. The probe determines the distribution at a certain time after excitation and therefore gives insight into relaxation and recombination processes of the sample.

In figure 3.4 a sketch of the operating principle of a transient absorption measurement with a pump-probe setup is shown. The pump pulse hits the sample and the induced changes are probed by the probe pulse. The time delay Δt can be adjusted by a delay stage, which introduces an optical delay in the path. Here, the transient absorption spectroscopy was performed with a custom built pump-probe setup (Newport Inc.). As light source a Ti:Sa amplifier (Libra HE, Coherent Inc.), with a maximal repetition frequency of 1 kHz at a pulse energy of 5 mJ and a pulse duration of 100 fs, was used. The amplifier generates both the pump and the probe pulse and has an output wavelength of 800 nm. The wavelength of the pump pulse is adjusted with an optical parametric amplifier (OPA) system (OPerA Solo, Coherent Inc.) to the required wavelength. This OPA system enables a tuning of the excitation wavelength over a wide range from 290 nm to 10 μm . In order to probe the sample at a certain time delay Δt , the probe pulse is focused into a dispersive material to generate a continuous white light pulse. Different crystal materials generate

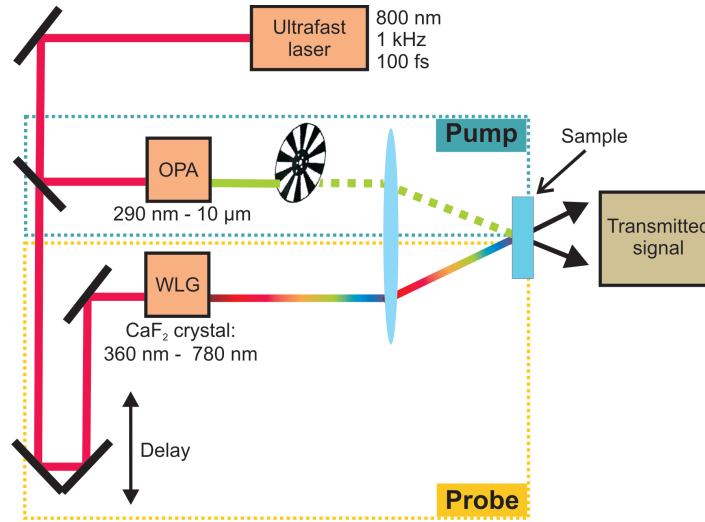


Figure 3.4: Schema of Pump-Probe setup to measure the transient absorption. The laser pulse (800 nm) generated by a Ti:Sa amplifier, is split up and used as pump and the probe pulse. The pump pulse is firstly directed on an optical parametric amplifier (OPA) to set the wavelength in the range of 290 nm to 10 μm to a certain value and secondly hits a chopper wheel, which is synchronized to the OPA. The time delay between pump and probe pulse is determined by a delay stage and a white light generator (WLG) is used to obtain a continuous white light spectrum to probe the changes induced by the previous pump pulse.

different spectra and are generally called white light generators (WLG). Here, a calcium fluoride (CaF₂) crystal was used to probe a spectrum from roughly 360 nm to 790 nm. The transmitted light is detected with a CCD-spectrograph (MS127i, Oriel Instruments). Furthermore, to be able to determine the induced changes in transmission a chopper wheel is attached in the path of the pump pulse. This chopper wheel is synchronized to the OPA. It blocks every second pulse and is triggered to the spectrograph. The differential transmission (DT), given by the induced change of transmission ΔT divided by T_0 , the transmission of the probe pulse without the pump, is recorded in the spectrograph and is given by:

$$DT = \frac{\Delta T}{T_0} = \frac{T - T_0}{T_0} \quad (3.7)$$

For small changes in transmission of maximal 10%, the DT is proportional to changes of the absorption coefficient. Actually in the setup used here, the changes of the optical density (ΔOD) are displayed directly.

$$\Delta OD = \log(T_0) - \log(T) \quad (3.8)$$

Comparing equations (3.7) and (3.8) one can easily connect the differential transmission and the change of the optical density.

However, it has to be taken into account that due to wavelength-dependent dispersion effects, the probe pulse hits the sample at different times. Therefore, the temporal overlap

of pump and probe depends not only on the optical path but also on the wavelength. The wavelength-dependent variation of the onset time is also called chirp. To correct for this, a second-order polynomial function was applied individually to every data matrix providing a wavelength independent delay.

In the result section of this thesis pump-probe measurements on resonantly excited charge carriers are presented. However, probing and pumping the same wavelength range is difficult, since the pump pulse is much more intense than the probe and without further treatment one would mainly record the pump. By attaching additional polarization filters it is possible to block the polarized pump pulse, yet still detecting the transmitted probe. In dependence of the pump wavelength the light exiting the OPA is horizontally or vertically polarized, whereas the polarization of the probe beam does not change. Therefore, in the case of equal polarization a $\lambda/2$ -plate needs to be inserted into the probe path.

PL lifetime (streak camera)

A streak camera (C5680, Hamamatsu) is used to determine the PL lifetime of a sample. This works as described in the following and as shown in figure 3.5. The sample is illuminated with a pulsed diode laser (LDH-P-C-405, Pico Quant) with a wavelength

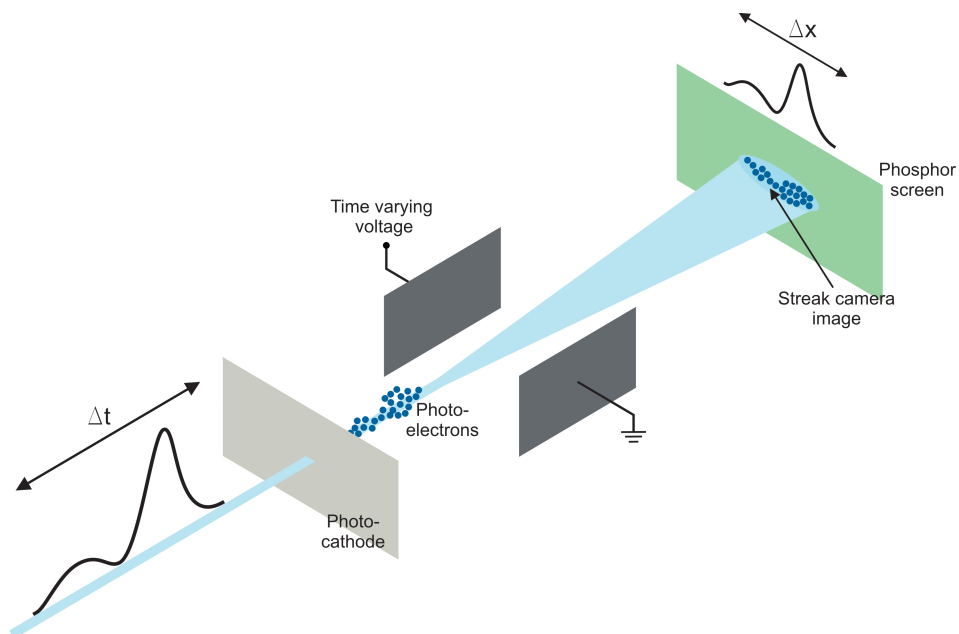


Figure 3.5: Working principle of a streak camera. The temporal profile of the emitted light pulse is transformed to photoelectrons as photons hit a photocathode. The electrons are subsequently deflected by a time varying electric field, created by a capacitor. This time-dependent deflection leads to a spatial profile of the electrons. These electrons hit a phosphor screen and are reconverted to photons. A CCD camera is used to detect the photons creating the streak camera image.

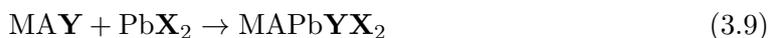
of 405 nm. The camera and the laser diode have to be triggered with the right delay to be able to record the whole signal of the process to be monitored. The laser beam hits the cuvette, filled with the sample solution, under an angle of approximately 30 degree. The isotropically emitted PL is detected perpendicular to the surface of the cuvette and focused with two lenses into an imaging spectrograph (250i, Chromex) to split it up spatially according to the wavelength before reaching the camera. In the camera, the photons hit a photocathode and are converted into electrons. Subsequently, these electrons are accelerated and pass through a capacitor. The voltage of the capacitor is changed linearly in time, thus, in dependence of their arrival time the deflection of the electrons varies. Consequently, these electrons, which exhibit a certain temporal profile, hit an attached phosphor screen at different spots. The electrons are reconverted to photons and collected by a CCD camera, providing information about the time between the moment the laser hits the sample and the moment a photon is emitted. Hence, the obtained streak camera image reveals a PL signal resolved both temporally and spectrally. Furthermore, in order to be able to compare different measurements, the offset of the plots have been corrected and normalized to the peak intensity.

3.3 Synthesis: Ligand-assisted exfoliation

The ligand-assisted exfoliation is a top-down synthesis of perovskite nanoplatelets (NPLs). In this part of the thesis, the synthesis is described in a way to be able to track the single steps and to perform the synthesis solely by following these instructions. More details on the mechanism and fundamental working principle will be discussed in chapter 4.

3.3.1 Precursor synthesis

For the synthesis of the perovskite nanoplatelets several precursors are needed. The generalized reaction to obtain methylammonium lead halide perovskites is described as follows:



where **Y** and **X** represent the contained halides, namely iodide, bromide or chloride. The content of halides can be adjusted by using a combination of four different precursors salts **MAY**, **MAX**, **PbX₂** and **PbY₂**. To simplify, only the case of two reagents are shown in reaction equation (3.9). The reaction takes place under ambient conditions in toluene and, as a ligand, a small amount of oleylamine and octanoic acid is added.

The typically used materials were PbCl₂ (lead(II) chloride, 98 %), PbBr₂ (lead(II) bromide 98 %), PbI₂ (lead(II) iodide 99 %), methylamine (CH₃NH₂, 33 wt% in absolute ethanol), hydrochloric acid (HCl, 37 wt% in water), hydrobromic acid (HBr, 48 wt% in water), hydriodic acid (HI, 57 wt% in water), oleylamine (70 %, technical grade), diethylether (99.8 %), octanoic acid (99 %) and toluene (99.8 %). All of these chemicals were purchased from Sigma-Aldrich and used as received.

In a first step, the precursor **MAY** (**Y** = I, Br, Cl) was fabricated. For MABr 36 ml of methylamine (33 % in absolute ethanol) were filled in a 100 ml round bottom flask, placed in an ice bath and stirred continuously. Subsequently, 28 ml of HBr (48 wt% in water by weight) were added. For MAI 33 ml of HI (57 wt% in water) were added to 36 ml of methylamine (33 % in absolute ethanol). After mixing the two solutions, the obtained product was stirred for two hours to complete the reactions. Thereupon, the water was removed through rotary evaporation at 50 °C and under 200 mbar vacuum, providing MABr or MAI as precipitants. In a last step, the raw product was washed three times with diethyl ether and then dried at 70 °C under vacuum conditions for five hours. After this step, the synthesis of the precursor is completed.

3.3.2 Synthesis of perovskite nanoplatelets

Mixed halide perovskites can be fabricated the same way by using precursor salts containing the different halides. In a first step, bulk perovskite powders were prepared by a simple

grinding process. In a typical synthesis, 0.16 mmol of MAY ($Y = \text{I, Br, Cl}$) powder was mixed with 0.16 mmol of corresponding PbY_2 powder in a mortar and then the mixture was grinded using a pestle. The formation of bulk perovskites while grinding is indicated by a change of colors. During grinding the color of the precursor powders changes as one can see in figure 3.6, showing the characteristic color of MAPCl (white), MAPBr (yellow) and MAPI (black). In a next step MAPbY_3 ($Y = \text{Br, I, Cl}$) nanoparticles were prepared

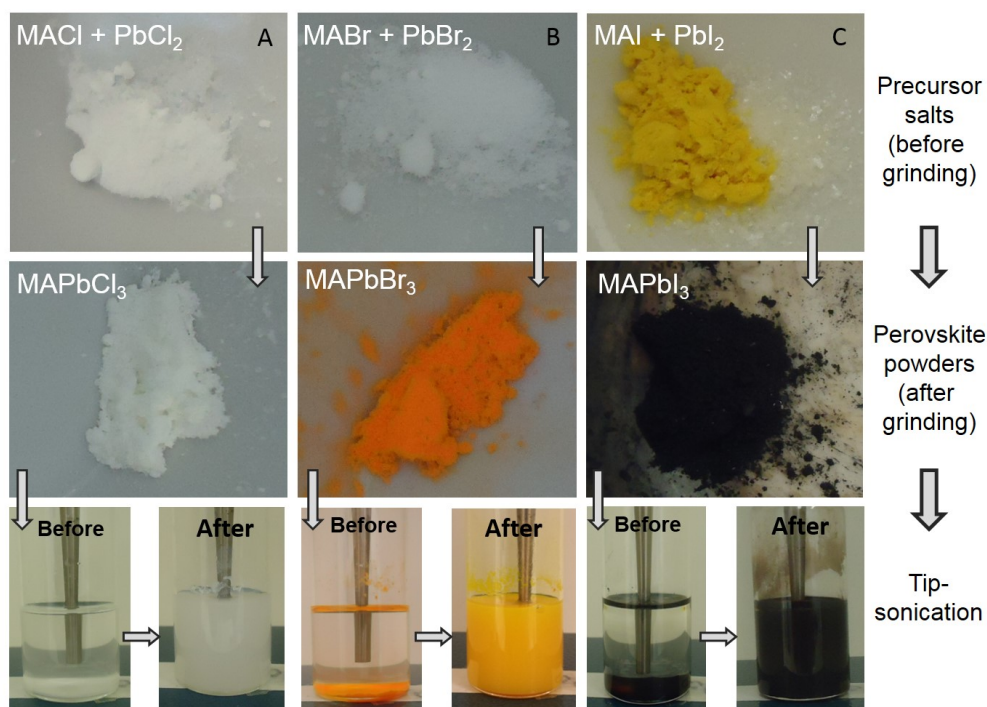


Figure 3.6: Pictures of different steps of synthesis: Grinding and tip-sonication. In the upper row the starting precursor salts before grinding are shown. By comparing the pictures of the precursor powders (upper row) and ground powder (middle row) a change in color can be noticed. By grinding the powders, the characteristic colors of MAPCl (white), MAPBr (orange) and MAPI (black) are obtained. To get the produced perovskite crystals in solution, toluene and the capping ligands (oleylamine and octanoic acid) are added and tip-sonication is performed. The bottom row shows the solution before and after tip-sonication. After the tip-sonication the perovskite particles are nicely dispersed in toluene. The figure is adopted from the publication of Hintermayr et al. [72].

from a previously ground bulk perovskite powder. The previously ground powders were added to a mixture of 10 ml of anhydrous toluene, 0.3 ml octanoic acid and 0.3 ml of oleylamine. Subsequently, the solution was sonicated using a tip sonicator (SonoPlus HD 3100, Bandelin) at 50 % of its maximum power for 30 minutes. As one can see in figure 3.6, the powders were not dispersible in toluene prior to tip-sonication. Yet, after sonication the colloidal solution of MAPbY_3 ($Y = \text{Br, I, Cl}$) was well dispersed and concentrated.

The obtained solutions contain nanocrystals of different sizes and shapes, which can be separated by careful centrifugation and dilution.

3.3.3 Separation of thinner and thicker nanoplatelets by centrifugation

Since the solution of perovskite crystals was quite dense, it only exhibit a weak PL signal. In order to separate the thinner nanoplatelets the prepared solutions had to be diluted immediately after the sonication. After dilution the solution was put in a centrifuge at a speed of 7000 rpm for 10 minutes. During centrifugation bigger crystals precipitate and the thinner NPLs stay in solution. Hence, for the further process the supernatant was used, which consists mainly of thinner NPLs. The recorded PL of the obtained dispersions are blue-shifted compared to the typical PL wavelengths of corresponding perovskite films, indicating that the separation of thinner, quantum-confined NPLs was successful. The as-obtained perovskite dispersions exhibit strong violet-blue (approx. 360 nm), blue (approx. 450 nm) and orange-yellow (approx. 680 nm) fluorescence for MAPCl, MAPBr and MAPI, respectively.

In order to separate the thicker nanoplatelets showing bulk-like properties, the dispersions produced by sonication were cooled down to room temperature and centrifuged at 9000 rpm for 10 minutes. Afterwards, the supernatant was thrown away and the sediment was redispersed in 10 ml toluene by conventional ultrasonication. The remaining micron-sized crystals were removed by a further centrifugation at 5000 rpm for 5 minutes. Hereby, in the case of MAPBr a bright yellow-green colored solution was obtained. The same procedure was applied for the preparation of MAPCl and MAPI. The received solutions emit in the blue and near-infrared (NIR) spectral regions, respectively.

3.3.4 Preparation of mixed halide perovskite nanoplatelets

For the preparation of mixed halide perovskite ($\text{CH}_3\text{NH}_3\text{PbBr}_{3-x}\text{Cl}_x$ and $\text{CH}_3\text{NH}_3\text{PbBr}_{3-x}\text{I}_x$) platelets, corresponding reagents (MABr, MAcl, MAI, PbCl_2 , PbBr_2 , and PbI_2), were first grinded to acquire bulk perovskite powders with different compositions. For example, $\text{MAPbBr}_2\text{I}_1$ perovskite powder was prepared by grinding a mixture of 0.16 mM MABr, 0.08 mM of PbBr_2 and 0.08 mM PbI_2 . The obtained powders were dispersed in a mixture of 10 ml anhydrous toluene and 0.3 ml oleylamine and then subjected to tip-sonication under similar experimental conditions as described before. The obtained solution was centrifuged at 8000 rpm for 5 minutes to remove excess reagents and thinner platelets. Afterwards, the sediment was dispersed in 10 ml of anhydrous toluene to produce mixed halide perovskite platelets. Corresponding to the halide content, the color of the dispersions is different (see figure 3.7 top row). Samples

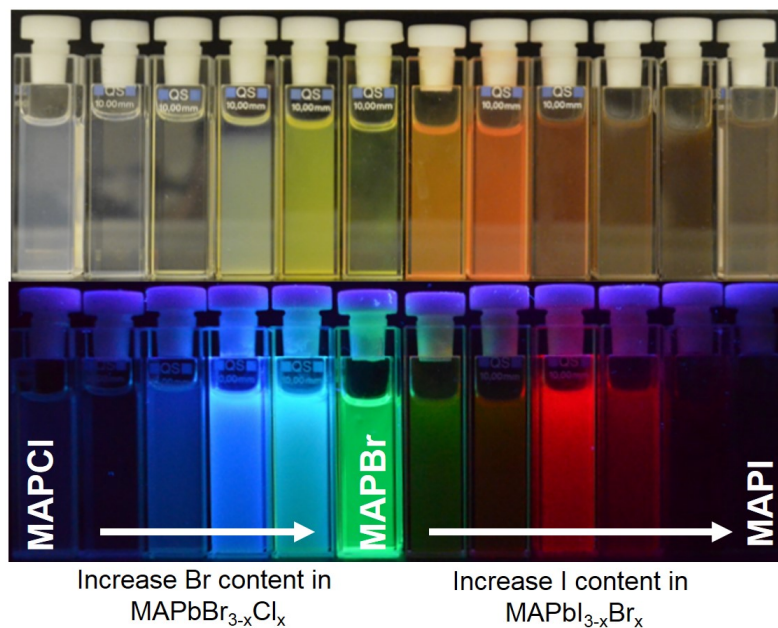


Figure 3.7: Cuvettes of mixed halide perovskites. In the top line dispersions illuminated with white light are shown. From left to right the content of bromide in $\text{CH}_3\text{NH}_3\text{PbBr}_{3-x}\text{Cl}_x$ and further of iodide in $\text{CH}_3\text{NH}_3\text{PbBr}_{3-x}\text{I}_x$ is increased. According to the halide content, the color of the dispersions are different. In the bottom line the same cuvettes illuminated with UV light are depicted. The observed PL ranges from blue over green to red.

with a higher chloride content, appear white. As the bromide content is increased, a shift to yellow can be noticed. With increasing iodide content, the color turns to orange, brown and further to black, the characteristic color of MAPI. Analyzing the PL of these samples by illuminating the cuvettes with UV light, a wide range of emission colors ranging from violet to infrared (compare figure 3.7 bottom line) can be seen. A more detailed analysis of the PL in dependence of the used halide will be presented in the results part section 5.2.

Chapter 4

Fabrication and separation of nanoplatelets with individual thicknesses

In this chapter a new, simple and versatile synthesis to obtain high quality lead halide perovskite nanoplatelets (NPLs) with lateral dimensions between 20 - 200 nm and a controllable thickness down to a single perovskite unit cell is introduced. The fabrication of nanoplatelets comprising MAPbX_3 ($X = \text{Cl, Br, I}$) and mixed halides with varying ratio of Br/Cl or I/Br is presented. These thin NPLs are confined in one dimension, show quantum confinement effects and were separated according to their thickness. Subsequently, their structural properties and composition were analyzed by using electron microscopy methods, XRD and AFM. A few optical measurements are presented to substantiate drawn conclusions, yet a detailed analysis of the optical properties will follow in the next chapters. Here, the mechanism of the synthesis and the first basic characterization of the achieved nanostructures and compositions are presented.

4.1 Bulk-like perovskite nanocrystals of different composition

The executed synthesis of perovskite crystals is based on a technique called ligand-assisted liquid-phase exfoliation. More details on the used chemicals and the synthesis procedure can be found in section 3.3. This technique is well-known for the fabrication of high-quality 2D materials, such as graphene and metal chalcogenides [133–135]. It relies on the use of a solvent, which reduces the energy of exfoliation according to the Hansen solubility parameter [136]. In the case of perovskite nanocrystals, the exfoliated parts are constituted of altering layers of organic and inorganic components. In general, there are different approaches to synthesize colloidal lead halide perovskite nanocrystals. Many of them are ligand-guided like the one presented in this work [15, 137–142].

4.1.1 Synthesis and structural analysis of perovskite nanocrystals

In the first step of the synthesis the solid precursor materials MAY and PbX_2 ($X, Y = Cl, Br, I$) are mixed together and grinded by using a mortar and a pestle. This process (dry step) is depicted in figure 4.1. Here, the synthesis is exemplarily shown for $MAPBr$,

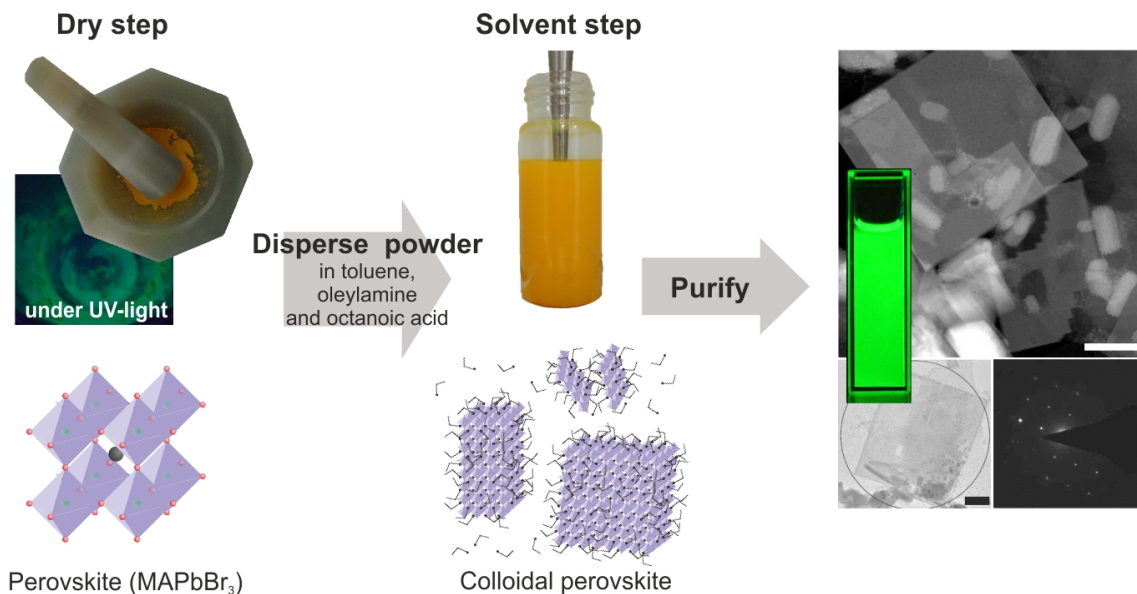


Figure 4.1: Sketch of perovskite nanocrystal synthesis using ligand-assisted liquid-phase exfoliation. The different steps of grinding (dry step), tip-sonication (solvent step) and purification are schematically illustrated. Moreover, on the right side one can see the obtained dispersion of $MAPBr$ bulk-like NPs illuminated with UV light, showing a bright green emission. Besides the cuvette, a STEM image and an HRTEM image with corresponding diffraction pattern are illustrated. The scheme is taken from the publication of Hintermayr et al. [72].

therefore, the precursor salts MABr and PbBr_2 are used. During grinding MAPBr already emerges, reflected by an instating color change from white to orange. An additional strong indication of the formation of perovskites is the green fluorescence of the powder under UV illumination. According to literature the PL emission of MAPBr bulk material is roughly located at 530 nm (2.34 eV) [15, 143]. To be sure that the main amount of the precursor is converted to MAPBr, the grinding is executed for several minutes.

Figure 4.2a) shows SEM images of microcrystals formed in the solid-state reaction, revealing a rather large size distribution (1 - 10 μm) and a variety of morphologies. Additionally, the formed perovskite crystals seem to be layered, consisting of stacked thin-

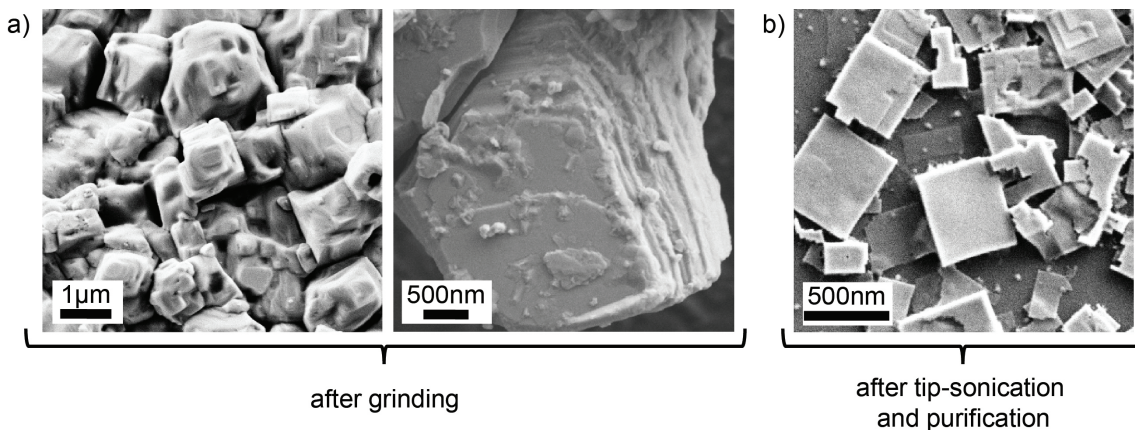


Figure 4.2: SEM images of perovskite crystals, taken after different fabrication steps.

- a) Perovskite powder obtained by grinding, before tip-sonication. One can identify micro-sized crystals which have been formed during grinding and seem to consist of stacked thinner platelets. b) NPLs achieved after tip-sonication and several purification steps. These NPLs show a rectangular shape and a lateral size of a few hundreds of nanometers.

ner perovskite platelets. Figure 4.2b) displays the resulting perovskite NPLs, obtained after tip-sonication and purification. The previously layered structure of big microcrystals seems to be dissipated into smaller, rectangular shaped platelets.

After the fabrication of the perovskite microcrystals, the next goal is to disperse these particles in solution. To achieve this aim, toluene and some capping ligands, a mixture of oleylamine and octanoic acid, are added to the perovskite powder. Then, the mixture is subjected to tip-sonication. The colorless toluene quickly turns into a murky orange solution, as the perovskite crystals become dispersed. In more detail, due to the strong sonication bigger perovskite pieces are broken up at the interface between organic and inorganic components. Subsequently, the solvent infiltrates in between these layers, with the organic ligand binding to the newly formed facets, compensating the residual negative charge and hereby stabilizing the NCs. Since the oleylamine does not fit into the gap between the $[\text{PbI}_6]^{-4}$ octahedra, the used ligand prevents reshaping of bigger crystals.

This process is visualized in the solvent step, sketched in figure 4.1. Control experiments without the usage of capping ligands were performed to support this claim. In those attempts the bulk powder remained insoluble in the solution, even after exposing it to tip-sonication for more than an hour. In order to obtain a purified dispersion of perovskite nanoplatelets several centrifugation steps are necessary. This procedure is explained in more detail in section 3.3. On the right side of figure 4.1 the thereby obtained dispersion illuminated with UV light is depicted, showing a bright green fluorescence.

After the synthesis is completed, multiple measurements were performed in order to characterize and analyze the obtained MAPBr nanostructures. Figure 4.3 illustrates the obtained XRD spectrum. This measurement confirms a cubic crystal structure with a lattice constant (a) of 5.96 Å, similar to literature values [8]. To calculate the lattice

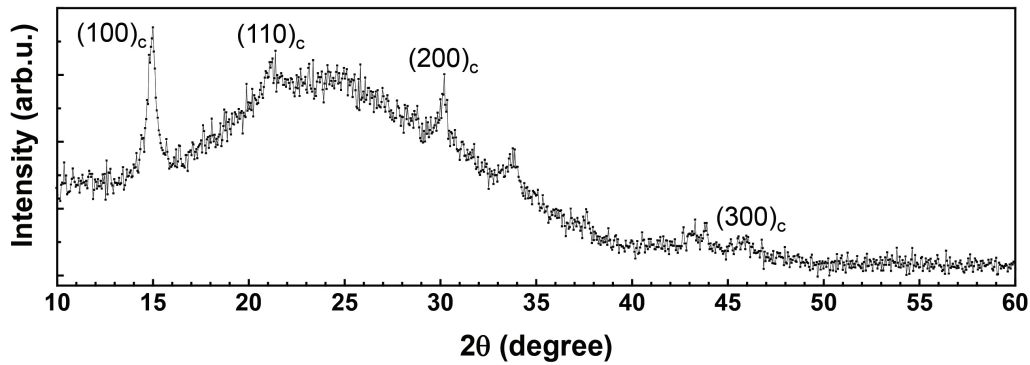


Figure 4.3: XRD spectrum of bulk-like MAPBr nanocrystals. The measurement is performed at room temperature. In this temperature range MAPBr is present in the cubic phase. The recorded peaks of intensity can be attributed to the $(100)_c$, $(110)_c$, $(200)_c$ and $(300)_c$ reflexes and are labeled accordingly. The broad diffraction peak can be associated to the amorphous glass used as a substrate.

constant of MAPBr on the basis of the recorded XRD spectrum, the 2θ values of the diffraction peaks have to be determined. Using Bragg's law (3.3), one obtains for a cubic crystal structure:

$$d_{hkl}^{cubic} = \frac{a}{\sqrt{h^2 + k^2 + l^2}} \xrightarrow{(100)} d_{100} = a = \frac{\lambda_{K\alpha,Cu}}{\sin(2\theta)} = 5.96 \text{ \AA}, \quad (4.1)$$

with $\lambda_{K\alpha,Cu}$, the known wavelength of the incoming X-ray, originated from a copper anode. Furthermore, h , k and l stand for Miller indices, which precisely define planes in a crystal lattice. In figure 4.3 the recorded reflexes can be attributed to the $(100)_c$, $(110)_c$, $(200)_c$ and $(300)_c$ reflexes. Additionally, a broader diffraction peak spread over few tens of degree is observed. This feature can be associated to the glass on which the sample is drop-casted. Since glass is an amorphous material, a broader not distinct peak is expected. In addition to that, no signs of residues of the precursor salts are recorded [144].

In figure 4.4 SEM and STEM images of the nanocrystals obtained after tip-sonication are depicted. These electron microscope images show that the NCs are polydisperse in size and shape and are mainly rectangularly shaped NPLs. The NPLs exhibit different sizes ranging from a few tens of nanometers up to several hundreds of nanometers. Furthermore, the varying contrast of the NPLs suggest a strong variation of their thickness. For a precise thickness determination an AFM was utilized. The results of these measurements are presented in section 4.2. Besides nanoplatelets, a small amount of other morphologies such as cubes and rods are seen on these images. Diffraction measurements, one is shown exemplarily on figure 4.1, prove that the NPLs feature a high crystallinity.

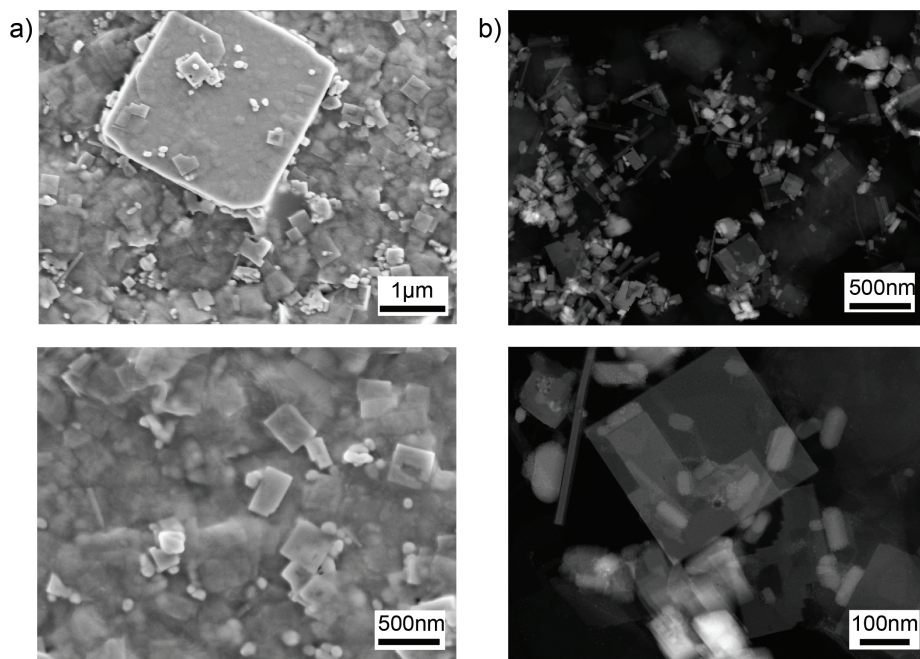


Figure 4.4: Electron microscopy images of MAPBr nanocrystals performed after tip-sonication. a) SEM images b) STEM images. These measurements clearly illustrate that the nanocrystals are polydisperse in size, shape and thickness. In the STEM images nanoplatelets of different thickness are recognizable.

4.1.2 Mixed-halide perovskite nanoplatelets

So far the synthesis was explained referring to MAPBr, however, it can be applied to fabricate MAPI, MAPCl and a combination of halides, e.g. $\text{MAPbBr}_x\text{Cl}_{3-x}$ and $\text{MAPbBr}_y\text{I}_{3-y}$, as well, with $0 \leq x, y \leq 3$.

Again, the quality of the fabricated nanoplatelets and their properties are studied. In figure 4.5 the XRD spectra of MAPCl, MAPBr and MAPI at room temperature are compared with each other. In this temperature range MAPCl and MAPBr can be found in

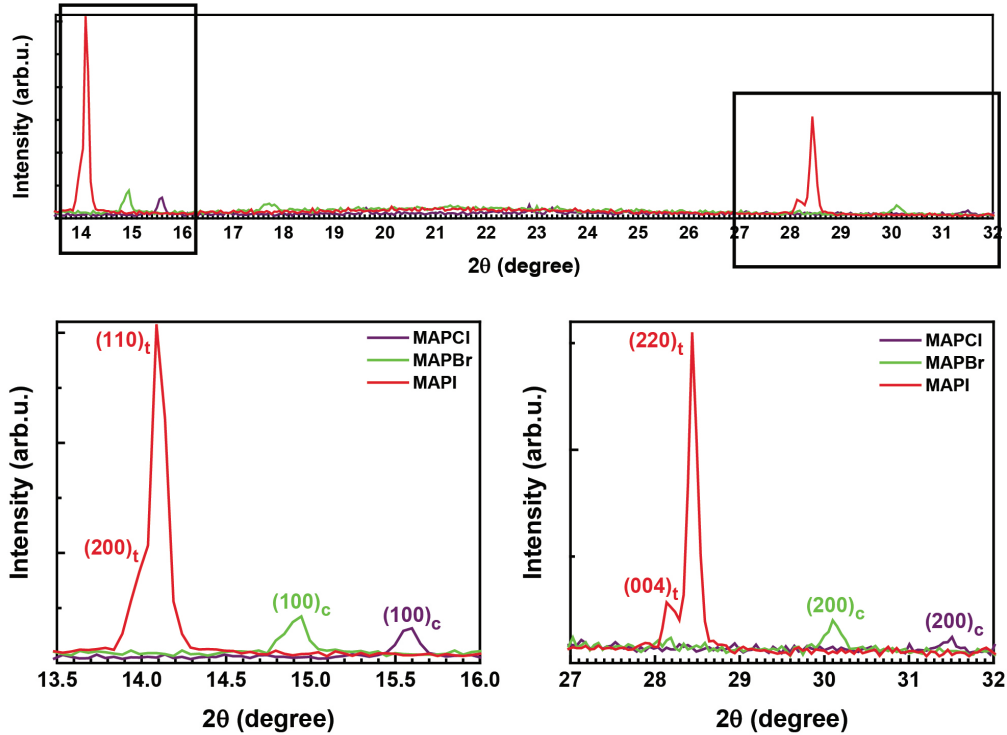


Figure 4.5: XRD scattering spectra of MAPCl, MAPBr and MAPI. In the spectra the characteristic perovskite XRD fingerprint is observed. The recorded peaks can be attributed to the $(100)_c$ and $(200)_c$ reflexes for a cubic structure and the double peaks to the $(200)_t/(110)_t$ and $(004)_t/(220)_t$ reflexes for the tetragonal structure, respectively. The measurements were performed at room temperature. The figure is adopted from Hintermayr et al. [72].

the cubic phase, whereas MAPI is in the tetragonal phase (compare section 2.1.4). Due to the unequal phases and lattice constants, different characteristic fingerprints are expected. On the one hand, in the case of MAPI a double peak is observed near $2\theta = 14^\circ$ and a mere pronounced one at $2\theta = 28^\circ$. These doublets correspond to the 200/110 and 400/220 lattice planes and are a clear evidence for the tetragonal phase [145]. On the other hand, the recorded single peaks for MAPBr and MAPCl located near the MAPI peaks, are in accordance with the implemented cubic phase [146]. Furthermore, a shift of the lowest order peak to larger angles with decreasing halide size is evident. Again, no features which can be attributed to the precursor salts are detected in the XRD spectra [147].

As already mentioned, ligand-assisted liquid-phase exfoliation can be applied to fabricate mixed halide organic-inorganic lead perovskite NPLs as well. A first noticeable difference between the obtained dispersions of mixed halide perovskites is their color. It gradually shifts from transparent to yellow for an increasing amount of bromide in $\text{MAPbBr}_{3-x}\text{Cl}_x$ and from yellow to orange to brown as the fraction of bromide in

$\text{MAPbBr}_y\text{I}_{3-y}$ increases (compare figure 3.7). A detailed analysis of the optical properties of mixed halide perovskites is given in the next chapter.

XRD measurements of mixed halide perovskites were performed to identify the obtained nanoplatelets. In order to track the impact of different halide concentrations, the position of the $(100)_c$ and the $(110)_t$ reflexes for the cubic and the tetragonal perovskite crystal structures are determined and presented in figure 4.6a). With varying halide con-

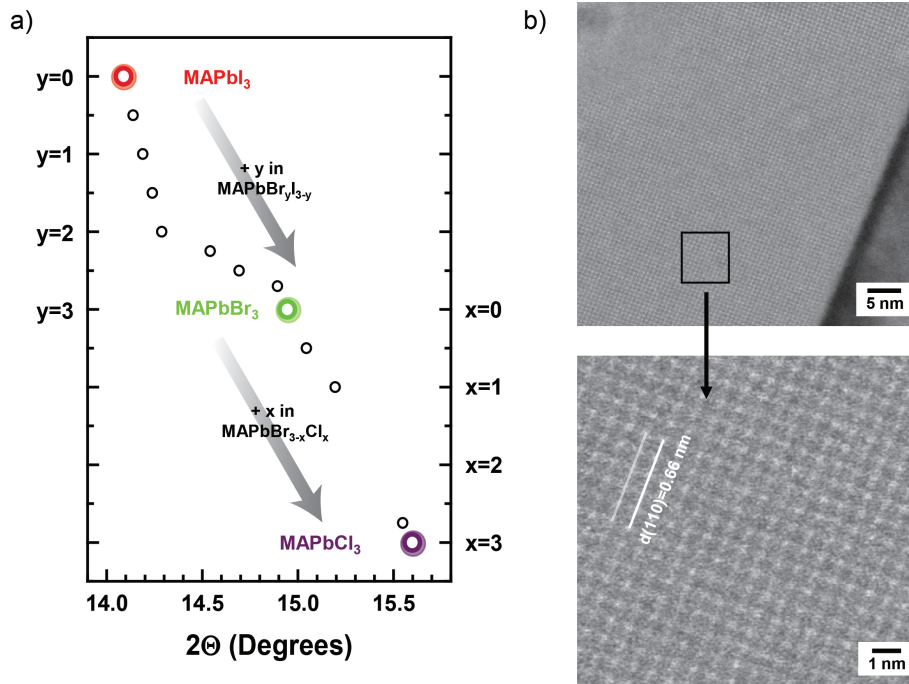
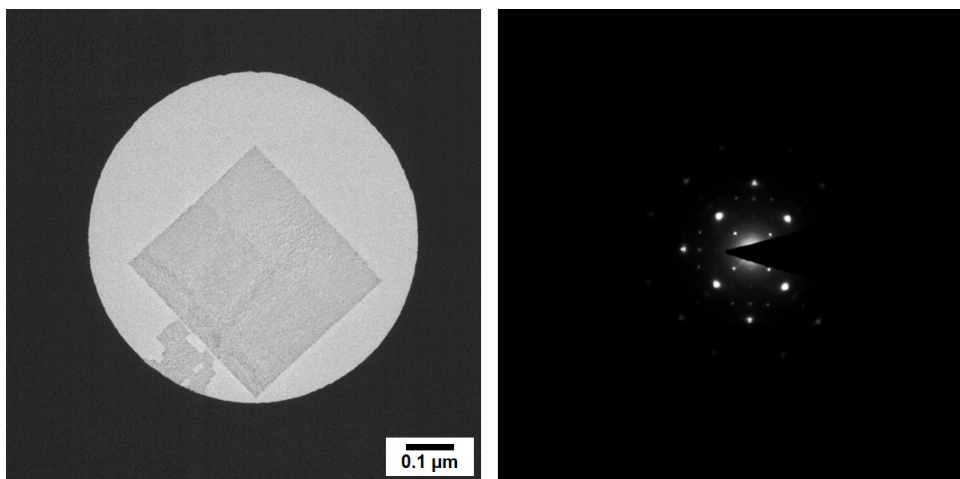


Figure 4.6: Characterization of inorganic-organic lead perovskites with mixed halides. a) Peak position obtained via XRD measurements of the $(100)_c$ and $(110)_t$ reflex. b) HR-TEM images of a MAPI NPI showing the individual atoms and clear lattice fringes with a spacing of 0.66 nm.

centration, a shift of the diffraction peaks is observed. The lattice parameters of halide perovskites strongly depend on the size of the halide ions, as they increase for larger atomic numbers. This affects the lattice constant of the perovskite nanocrystal, hence, the position of the $(110)_t$ and $(100)_c$ reflexes. As the bromide content and subsequently the iodide content is increased, the lattice constant grows progressively [148], leading to a shift of the recorded diffraction peak positions.

Further examinations of the MAPI NPIs utilizing HRTEM imaging reveal individual atoms and clear lattice fringes (see figure 4.6b)). These fringes have a spacing of 0.66 nm and agree well to the 110 lattice plane measured for bulk MAPI [88]. An additional evidence confirming the formation of perovskite NPIs is given by energy dispersive X-ray measurements, yielding a halide to lead ratio of roughly 3 to 1 (compare figure 4.7).



Element	Weight %	Atomic %	Uncert. %	Correction	K-factor
O (K)	24.66	75.09	0.63	0.51	1.921
I (L)	48.41	18.58	0.67	0.98	2.893
Pb (L)	26.92	6.32	0.70	0.99	4.409

$$\frac{\text{Atomic\%}(\text{iodine})}{\text{Atomic\%}(\text{lead})} = 2.94$$

Figure 4.7: EDX measurements on a MAPI NPI. The TEM image and the corresponding electron diffraction pattern image of a MAPI NPI show the single crystalline nature of it. The EDX measurements yield a ratio of iodide to lead of roughly 3 to 1. The figure is adapted from Hintermayr et al. [72].

The ligand-assisted exfoliation can be adopted to fabricate all-inorganic perovskite nanocrystals. Instead the organic cation (MA^+), inorganic cesium (Cs^+) can be used. The general process remains basically the same and is described in the publication by Tong et al. [149].

4.2 Separation of perovskite nanoplatelets with different thicknesses

The PL spectrum of MAPBr nanocrystals shown in figure 4.8 exhibits an asymmetrical shape and on the high energy side a broader shoulder is formed and additional peaks appear. These peaks indicate, like the electron microscopy images shown in figure 4.4, the

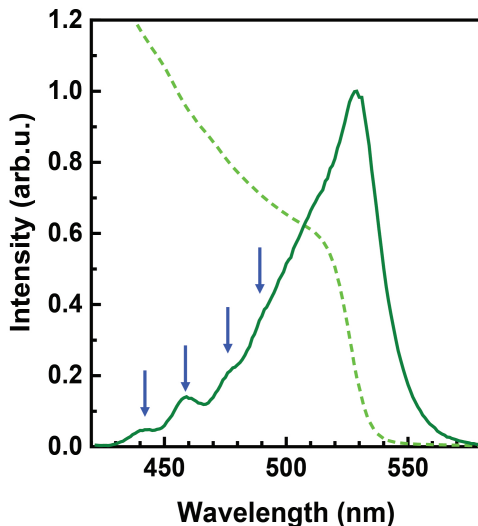


Figure 4.8: Absorption and PL spectrum of MAPBr nanocrystals. The absorption (dotted line) and PL spectra (solid line) show an absorption onset and PL peak at roughly 530 nm, which matches to the values of bulk MAPBr, reported in literature. Additional peaks, highlighted with blue arrows, are attributed to thinner platelets.

formation of very thin nanoplatelets exhibiting a blue-shifted PL emission due to quantum confinement effects. In the work of Sichert et al. [37] the emergence of additional peaks at identical positions is observed as well (compare section 2.1.6). In this publication the impact of quantum size effects in lead halide perovskite nanoplatelets on the PL emission is analyzed. Additionally, similar observations have been done in other studies on layered 2D MAPBr NPs [107, 150, 151].

To investigate the resulting product in more detail, the NPs have to be separated according to their thickness. In order to achieve this separation, the perovskite dispersion obtained right after the tip-sonication was diluted. With increasing degree of dilution the dispersion became more and more transparent in ambient light and a color change of the fluorescence from green to blue was noted (compare inset in figure 4.9a)). To quantify these findings UV-Vis and PL spectra of 10, 25, 50, 100 and 200 times diluted dispersions were acquired. In figure 4.9a) and b) the PL and absorption spectra of this dilution series are illustrated. In the PL spectrum of the weakly diluted sample (10 times) multiple peaks are recorded. Most striking is the double peak at approximately 446 nm/457 nm. Additionally,

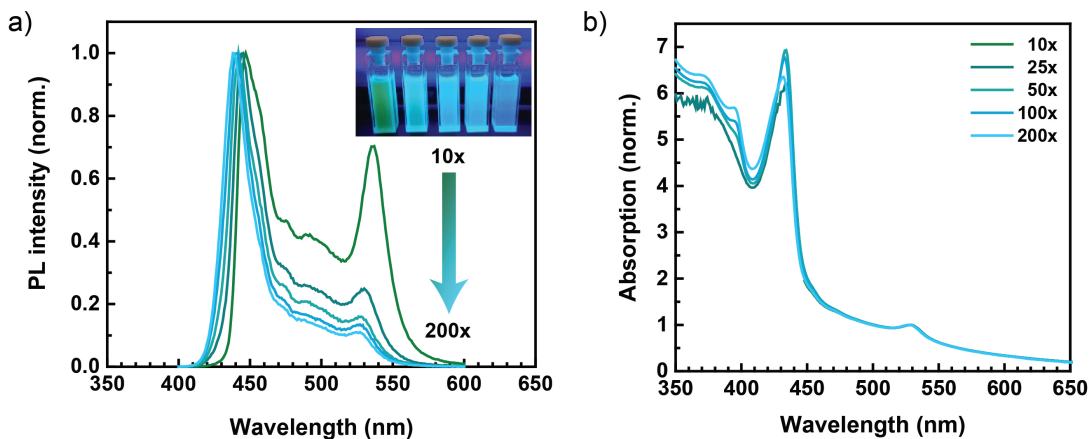


Figure 4.9: PL and absorption spectra of diluted MAPBr dispersions. The as-prepared solution was diluted directly after tip-sonication by 10, 25, 50, 100 and 200 times, respectively. a) PL spectra of diluted MAPBr dispersions. With increasing dilution the peak at 450 nm become more dominant in respect to the one at 535 nm. On the inset a photo of the analyzed dilution series under UV illumination is shown. The dilution is gradually increased from the left to the right picture. b) Corresponding absorption spectra, normalized to the peak at 535 nm. In these spectra no dependence on the degree of dilution is observed.

another peak with high intensity is recorded at 535 nm. The detected intensity at 535 nm is reduced with respect to the PL peak at 446 nm as the degree of dilution increases. Furthermore, a shift of the main PL peak to shorter wavelengths is observed and reaches a maximum blue-shift down to 438 nm for the 200 times diluted dispersion.

In contrast to the PL spectra, the normalized UV-Vis spectra remain nearly constant. Every sample shows a strong absorption peak at 433 nm with further peaks at 395 nm and 370 nm. These additional peaks are indications of excitonic contributions to the absorption spectrum and most likely originate from quantum-confined nanoplatelets. Since the UV-Vis spectra are independent of concentration, the structure and amount of the dissolved nanocrystals seem to be unaffected by the dilution, only the distance between them is changed.

In conclusion, according to the PL and absorption measurements most of the dispersed nanocrystals are extremely small, display quantum confinement in at least one dimension and absorb mainly light in the blue/UV region. The bulk-like nanoplatelets make up only a small fraction of the produced nanocrystals, resulting in a weak absorption in the green region. Moreover, the PL signal at lower energies merging for samples with higher concentration reveals that energy can be transferred from the thin nanoplatelets to the larger ones either through near-field mechanisms, such as Förster resonance energy

transfer (FRET), or through the reabsorption of emitted photons. Consequently, in dense dispersions the PL is red-shifted and mainly originates from bulk-like NPLs.

The as-prepared dispersion produced through tip-sonication is not stable over time. In dependence of the waiting time between sonication and measurement, drastic changes in the PL intensity are recorded as illustrated in figure 4.10. One can observe a decrease

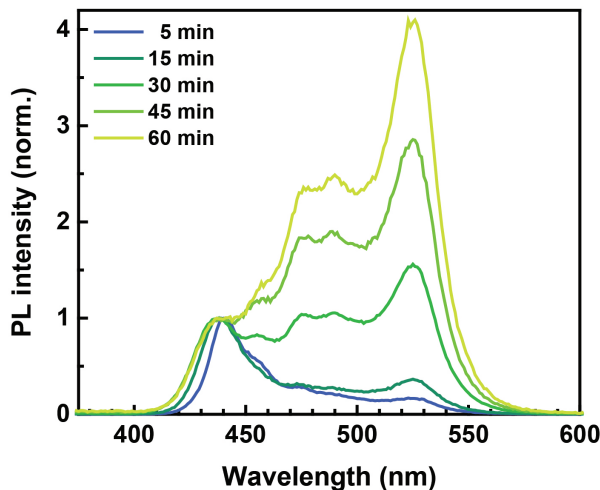


Figure 4.10: Development of the PL signal of a solution obtained by tip-sonication with increasing waiting time. The PL spectrum is recorded several times after the tip-sonication. A relatively increase of the PL signal at higher wavelengths is recorded and can be attributed to the stacking of NPLs and reshaping of bigger crystals.

of PL intensity at higher energies due to the stacking of quantum-confined nanoplatelets and subsequent reshaping to larger crystals. Additional treatments right after the tip-sonication such as centrifugation or dilution improve the stability and prevent stacking. For subsequent experiments the samples were purified by successive steps of centrifugation and redispersion of the obtained precipitant. The results shown here were achieved using MAPBr, but the same effects were observed for MAPI, MAPCl or mixed halides.

In figure 4.11 photos of perovskite NPL dispersions illuminated by UV light and the corresponding PL spectra are presented. These dispersions consist of perovskite NPLs with different halide content. For various halide compositions, a dispersion of bulk-like NPLs and one consisting of thinner NPLs was fabricated according to the synthesis routine described in section 3.3. In the comparison of samples with the same halide composition but with different crystal sizes a blue-shift of the fluorescence is noted. Furthermore, the PL peaks of the thinner platelets are asymmetric in shape, rather broad and have additional peaks at higher energies. The origin of the recorded blue-shift and the multipeak signal derives from the contribution of quantum-confined NPLs. The impact of the quantum confinement on

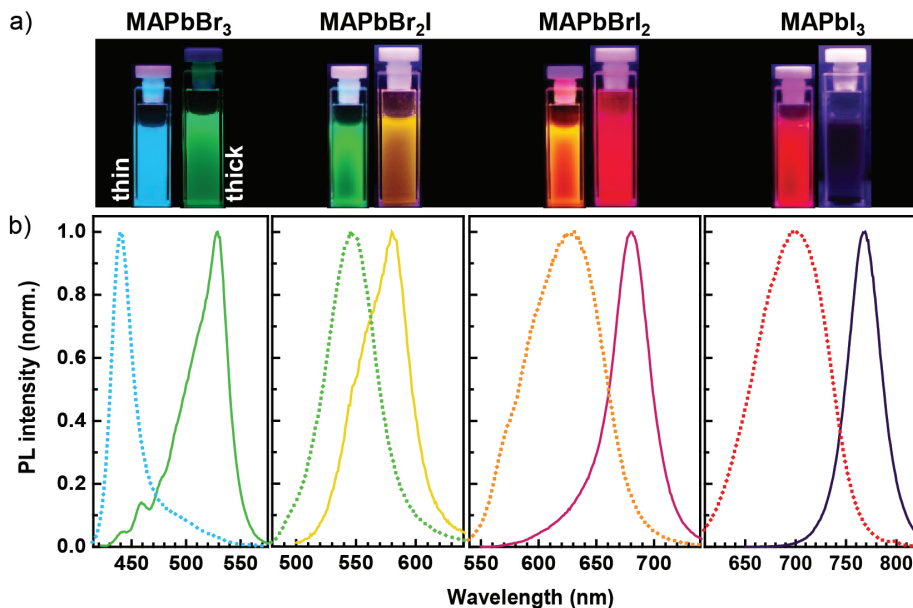


Figure 4.11: Tuning the PL emission of perovskite NPs through size and composition. a) Images of cuvettes containing perovskite NPs with different compositions and sizes under UV-light illumination. A bulk-like NPI dispersion (right) and a thin NPI dispersion (left) is shown for each halide composition. b) Corresponding PL spectra. A clear shift between the thin and thick samples is observed. The figure is taken from Hintermayr et al. [72].

the optical properties of the NPs will be analyzed in more detail in the following chapters. However, the obtained PL spectra generally indicate that the separation of big and small NPs is not yet perfect. A relatively broad PL peak is detected, since it is constituted of many peaks which results from inhomogeneous broadening [152].

To single out NPs of an individual thickness as accomplished in this work is extremely challenging. Several steps of centrifugation, redispersion and dilution are necessary to achieve this goal. At first, the geometry and structure of pure monolayer ($n = 1$), bilayer ($n = 2$) and trilayer ($n = 3$) dispersions of perovskite nanoplatelets are investigated. Hereby, one layer n is defined as a network of laterally arranged $[\text{PbI}_6]^{-4}$ octahedra. In figure 4.12 the TEM images of these dispersions are shown. All NPs, regardless of their thickness, have a rectangular shape and a large lateral size of several hundreds of nanometers. In general, an enhancement of the contrast with increasing thickness of the NPs is noted. This trend corroborates the increasing platelet thickness. Additionally, the emitted fluorescence shifts to higher energies as the thickness of the NPs is reduced, which leads to strong color changes of the dispersions under UV illumination (compare insets in figure 4.12). A yellow ($n = 2$), orange ($n = 3$), red ($n \geq 3$) and IR ($n = \infty$) emission under UV light is observed.

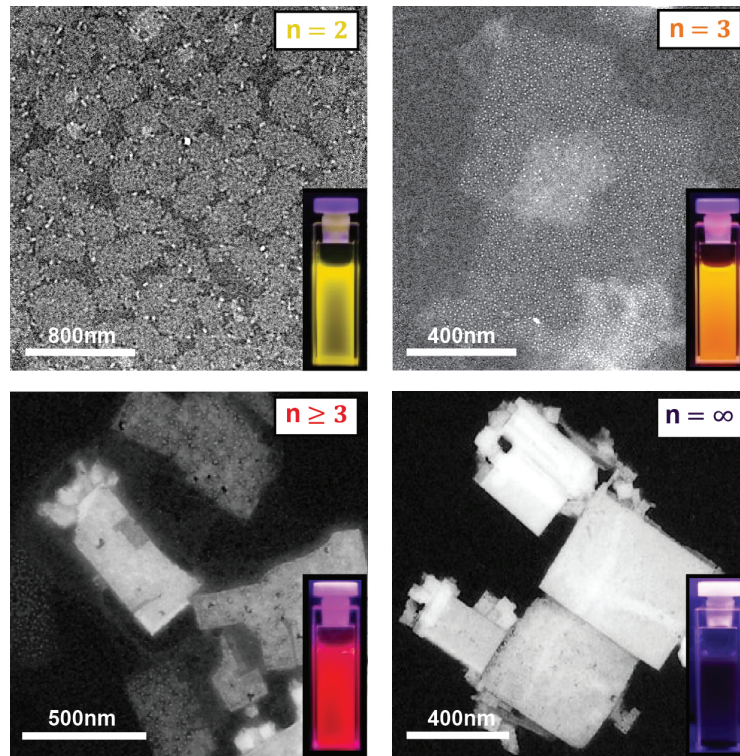


Figure 4.12: TEM images of MAPI NPLs with individual thicknesses. Inverted TEM images of NPLs with $n = 2$, $n = 3$, $n \geq 3$ and $n = \infty$ layers. The recorded decrease of contrast implies that the thickness of the NPLs increases progressively, as the PL emission spectra shifts to smaller wavelengths. The insets show the corresponding images of the dispersions illuminated with UV light. Parts of the figure are adopted from Hintermayr et al. [72].

One issue of the structural characterization of these thin platelets is the degradation of the organic compounds in the electron beam. The temporal sequence of high-resolution HAADF-STEM images, illustrated in figure 4.13, visualizes the effect of electron microscopy on thin perovskite NPLs. As the NPLs degrade in the electron beam, spherical nanoparticles start to appear. These emerging nanoparticles seem to be stable in the e-beam and show high brightness, hence, are considered to consist primarily of lead. Lead has a high Z-value and therefore exhibits a sharp contrast in an electron microscope. A detailed study of Dang et al. proved that the observed spherical nanoparticles are indeed metallic lead particles [153] and not perovskite quantum dots, as it has been reported previously [15, 36]. Thin platelets degrade immediately in the e-beam, making a structural analysis via electron microscopy methods very difficult and up to date the imaging of a MAPI monolayer has not been successful.

To separate platelets with more than three layers by centrifugation is hard or virtually impossible due to the small relative differences in density. The sample containing NPLs thicker than three layers but still in the regime of quantum confinement, is labeled as $n \geq 3$ and is composed of NPLs of different thicknesses.

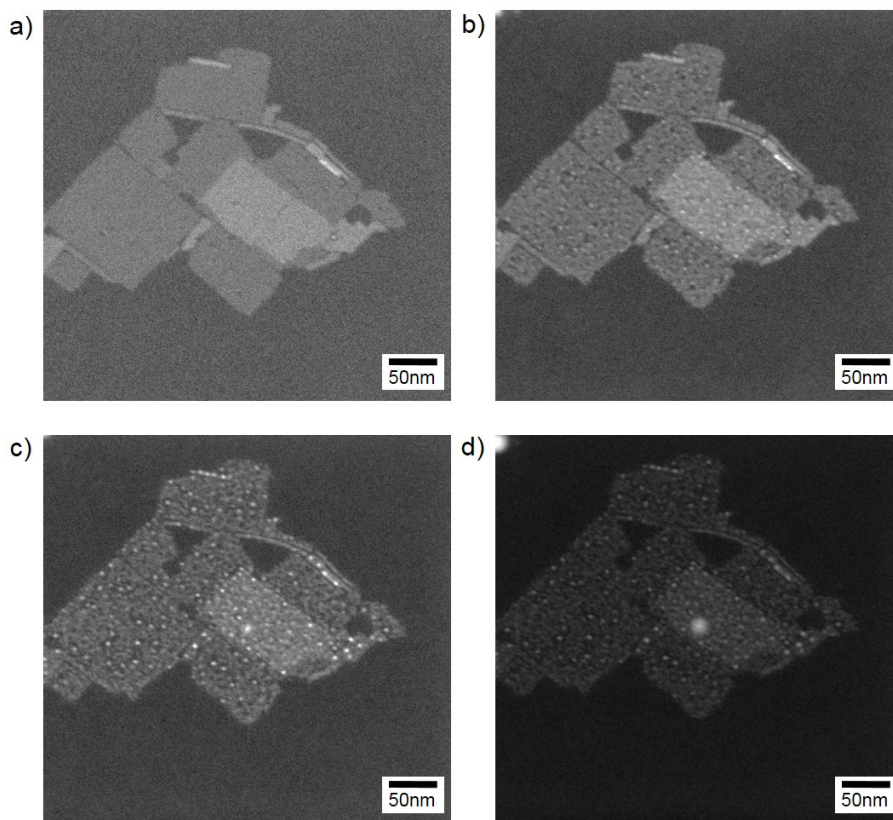


Figure 4.13: Degradation of MAPBr nanoplatelets in the electron beam. Temporal sequence (a-d) of high-resolution HAADF-STEM images of thin MAPBr nanoplatelets acquired at the same region. Upon interaction with the electron beam, these NPLs gradually degrade and small spherical nanoparticles start to appear on the platelets. These particles are most likely metallic lead, which are formed due to the degradation of the organic component of perovskite NPLs. The figure is taken from Hintermayr et al. [72].

Some indication of the modified thickness of the analyzed nanoplatelets have already been stated, like the shifted PL emission wavelengths and the changed contrast of the NPLs in the TEM images. To obtain the actual thickness and to further support the claim that the separation of MAPI NPLs according to their thickness was successful, AFM measurements were performed. These measurements were made on trilayers ($n = 3$) and on bulk-like ($n = \infty$) NPLs and are presented in figure 4.14. Separating single NPLs in order to measure their height in the AFM was difficult to achieve and different approaches have been applied. To obtain single NPLs on a glass substrate a strongly diluted dispersion was drop-casted. After a waiting time of 20 s the substrate was dipped several times in toluene and subsequently dried with nitrogen. The height profiles of bulk-like NPLs show a thickness in the order of tens of nanometers. The trilayer sample exhibit a height of only 2 nm. This value is coincided with the size of three MAPI unit cells, assuming a lattice spacing of 0.66 nm as determined previously via HRTEM measurements (compare figure

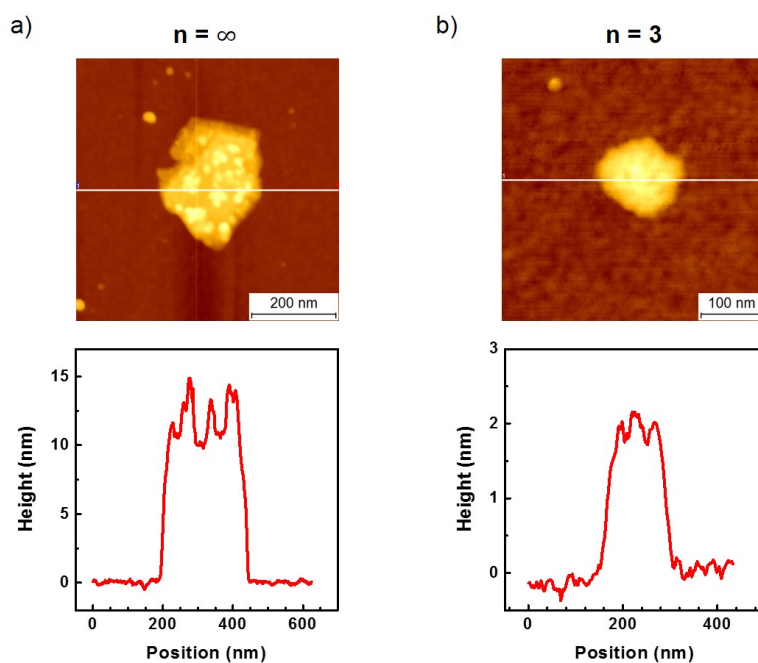


Figure 4.14: AFM images and height profiles of MAPI NCs a) Bulk-like MAPI NCs displaying a height of roughly 10 nm and b) $n = 3$ MAPI NPs revealing in the height profile a thickness of approximately 2nm.

4.6). The height measurements of several NPs of trilayer dispersions give comparable results. These AFM measurements additionally emphasize that the separation according to the thickness succeeded and solely NPs with a certain number of layers are dispersed in one solution. This achieved separation of lead halide perovskites with different thicknesses enables to perform thickness-dependent optical spectroscopy which will be presented in the following chapters.

Thickness-dependent absorption and emission of perovskite nanoplatelets

After the synthesis and separation of MAPI NPLs according to the thickness, their optical properties are analyzed more closely. In the following chapter, the absorption and PL spectra of these NPLs are studied. The thinner the platelets are, the stronger the quantum confinement is. Consequently, one can observe a thickness-dependent energy shift of the absorption onset and PL peak position. Based on the achieved knowledge in the optical steady-state measurements, one can subsequently draw some conclusions regarding the band gap energies (E_G), exciton binding energies (E_B) and the impact of quantum confinement on these quantities. In order to predict the effect of a reduced dimensionality, theoretical considerations are made and compared to experimental results. All in all, it is shown that one can control by means of size and composition the emission wavelength of the NPLs and practically tune it over the full visible spectral range. Furthermore, the thickness-dependent band gap energy and exciton binding energy of perovskite nanoplatelets is determined. Additionally, the temperature dependence of the absorption and the PL of MAPI NPLs is examined and compared to corresponding results of the bulk material known from literature.

5.1 Quantum confinement-induced shift of band gap and exciton binding energy

In order to learn more about the optical properties of MAPI NPIs and to analyze changes of the electronic band structure related to quantum confinement effects, steady-state absorption measurements were performed. In figure 5.1 the absorption of bilayer, trilayer and bulk-like NPI dispersions are depicted. With reducing thickness of the nanoplatelets a

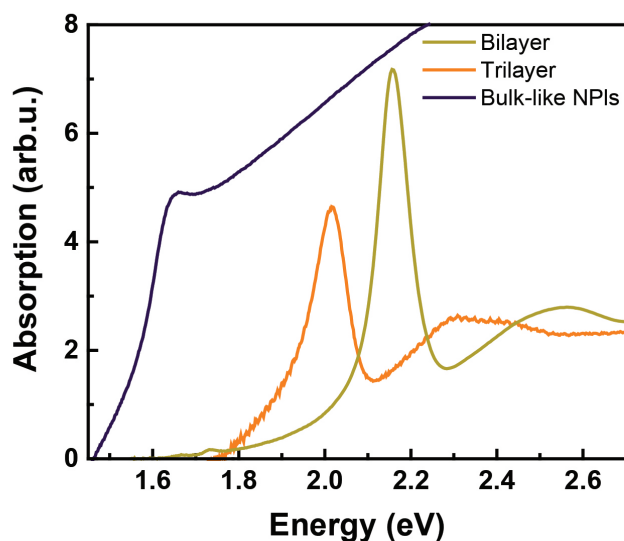


Figure 5.1: Steady-state absorption spectra of MAPI NPIs. The scale of the absorption intensity for the spectrum of the bilayer (dark yellow) trilayer (orange) and bulk-like (purple) NPI dispersions is arbitrary chosen, in a way to enable a direct comparison.

shift of the absorption onset to higher energies is observed. Additionally, excitonic features become more and more prominent. In case of bulk-like NPIs the excitonic contribution is hardly visible and only a small bump at 750 nm (1.65 eV) can be observed. In contrast, the trilayer and bilayer samples show a distinct peak, whose absorption is roughly two (for the trilayer) or three times (bilayer) as strong as the associated broad absorption band related to the continuum and recorded at higher energies. These peaks are attributed to excitons and are located at 615 nm (2.02 eV) and 575 nm (2.16 eV), respectively.

The MAPI mono-, bi- and trilayers are only a few nanometers thick. According to the result of the HRTEM the size of the unit cell is 0.66 nm. The length of the ligand oleylamine is approximately 15 Å, when considered to be a buckled carbon chain [154]. These thicknesses are in the region of the Bohr radius, therefore, quantum confinement needs to be taken into account. The NPIs are mainly reduced in one dimension, hence, they can be considered as 2D structures. The bulk-like NPIs are not confined in any direction

and are addressed as 3D materials. One consequence of the confinement is the increased exciton binding energy in 2D. For an ideal case one can determine that E_B in 2D is four times larger than in 3D [155, 156]. However, the dielectric environment of the organic and inorganic layers is not uniform, thus, an additional contribution to E_B is to be expected. This consideration is necessary to quantify for 2D NPLs, since the electric field between the electron and hole extends outside the inorganic layer into the surrounding medium [157, 158]. In the following a more detailed basis is used to build up an appropriate model.

5.1.1 Two-step quantum well model

To be able to explain the effect of quantum confinement and the resulting shift of the band gap energy, one has to recall the theoretical considerations presented in section 2.2. Different approaches can be used to explain and estimate the effect of quantum confinement on 2D materials. To solve the particle in a box problem with the assumption of an electron and a hole confined within infinite potential barriers is a good first approximation to get an idea of the impact of a reduced dimensionality on the optical properties. The resulting calculated values of the eigenenergies of MAPI nanoplatelets are depicted as a black solid line in figure 5.2b).

Going from the more general case to the particular one, it is reasonable to consider a finite potential and to factor in the attached ligands, namely oleylamine, as well. A two-step quantum well model is used, in order to describe the situation more realistically. Both electron and hole are confined in the nanoplatelet, which is surrounded by organic ligands. Comparing the dielectric constants, one obtains this relation:

$$\epsilon_{\text{NPL}} \gg \epsilon_{\text{ligand}} \quad (5.1)$$

The potential with the related boundary conditions is given by:

$$V(z) = \begin{cases} -\mathcal{X}_{\text{NPL}} & \text{for } 0 \leq z \leq L_{\text{NPL}} \\ -\mathcal{X}_{\text{ligand}} & \text{for } -L_{\text{ligand}} \leq z \leq 0 \text{ or } L_{\text{NPL}} \leq z \leq L_{\text{NPL}} + L_{\text{ligand}} \\ 0 & \text{else,} \end{cases} \quad (5.2)$$

with \mathcal{X}_{NPL} and $\mathcal{X}_{\text{ligand}}$ the corresponding electron affinities and L_{NPL} and L_{ligand} the length of the nanoplatelet and ligand, respectively. In this model the effective mass of the electron and hole in MAPI is used within the NPL. In the area of the ligand, it is assumed that the masses can be approximated by the free electron mass. Outside the semiconductor and the ligand, the hole potential is set to infinite, since the concept of the hole representing a missing electron only works within a material [37].

In figure 5.2a) the model for the two-step potential, which is applied to solve the problem in hand, is graphically shown. According to it, one can assess the energy shift of E_G in 2D nanoplatelets induced by a reduced thickness, ergo, the strength of the quantum confinement. The green solid line in figure 5.2b) illustrates the thickness-dependent energy changes calculated with this model. Actual values determined in experiments (compare section 5.3 for low temperature measurements) are depicted as well. χ_{ligand} is set at 2.1 eV by using the known band offset of oleylamine and MAPBr [37] and adjusting it to MAPI. The band offsets of MAPI are calculated to $V_{CB} = 1.8\text{ eV}$ and $V_{VB} = 3.4\text{ eV}$. Further

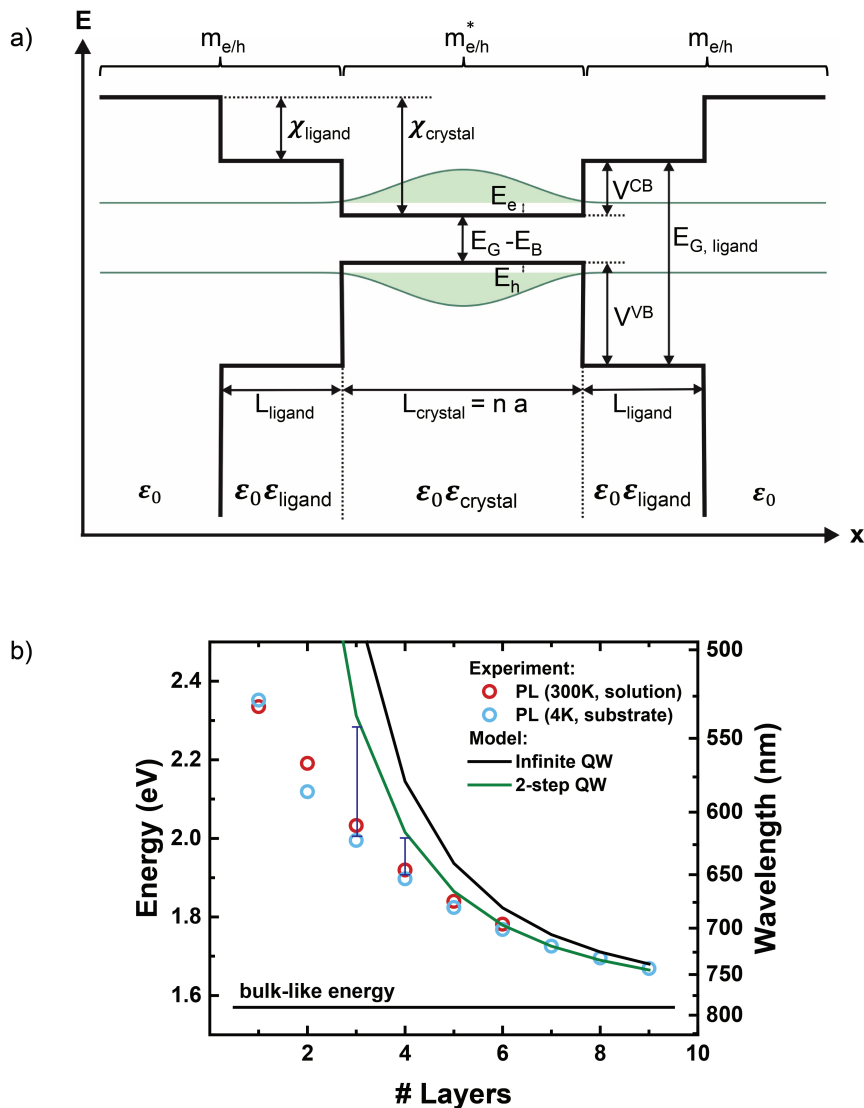


Figure 5.2: Two-step quantum well model applied to charge carriers confined in a MAPI nanoplatelet. a) Sketch of the potential with a labeling for all useful values. b) The resulting curves according to this model or with the assumption of infinite potential barriers are displayed. Besides these models, experimental values are marked as well. The deviation between model and experiment of approx. 280 meV and 120 meV for the 3 and 4 layers can be explained by taking into account the exciton binding energy.

Parameter	MAPI
m_e^*	$0.1 \cdot m_0$ [159]
m_h^*	$0.25 \cdot m_0$ [159]
a	6.6 \AA [37]
ϵ	6.5 [12]
χ	3.9 eV [62]
$E_G - E_B$	1.57 eV

Table 5.1: Parameters used to estimate the change of the electronic band structure due to quantum confinement effects. The given numbers are valid for MAPI and can be found in the cited literature.

parameters necessary for the calculation are listed in table 5.1.

In the comparison of the actual measured values and the one predicted by the models, one has to keep in mind that the model provides the band gap energy without taking into account the exciton binding energy. In turn, E_B might have a significant impact on the recorded PL signal the calculated E_G is compared to. However, in the case of NPLs thicker than four layers, the two-step quantum well model provides satisfying predictions. Given the small Stokes shift observed for perovskites [104] and an expected exciton binding energy in the order of tens of millielectron volts for weakly confined NPLs [37], a good agreement of calculations and measurements is expected. In order to obtain a better agreement also for even thinner, strongly confined NPLs, different factors need to be addressed. First of all, the strong increase of the exciton binding energy with decreasing thickness must be taken into account. The calculated difference for the four and three layered platelets are 120 meV and 230 meV, thus in the expected range of the exciton binding energy (compare following section 5.1.2). Yet, the measured values for mono- and bilayers still deviate from the predictions. For further improvements additional modifications would be necessary, for example regarding the effective masses of electrons and holes [160]. Overall, the model should be taken as a qualitative forecast of induced changes in E_G due to the impact of quantum confinement effects. To create a more sophisticated model is not within the scope of this work, however, would be of great interest to do in the future.

5.1.2 Modeled absorption spectra based on the Elliott formula

In the theory part of this thesis, the attraction of photoexcited electron-hole pairs due to their Coulomb potentials is discussed. This interaction can result in the creation of excitons. Hence, in order to analyze the electronic band structure, excitonic effects need to be included as well. One can implement Elliott's theory to model the absorption coefficient of

Wannier-Mott excitons [111]. By comparing theoretical predictions and actual measurements of the absorption, the exciton binding energy of semiconductors can be estimated. The dimensionality of the analyzed material is critical and needs to be considered in the theoretical calculation of the absorption coefficient (compare section 2.2.2). Using Elliott's theory, it is difficult to obtain an exact value of E_B , since the exact position of the continuum is hard to determine for absorption measurements of MAPI at room temperature. However, it is a good method to conduct an estimation of E_B and E_G .

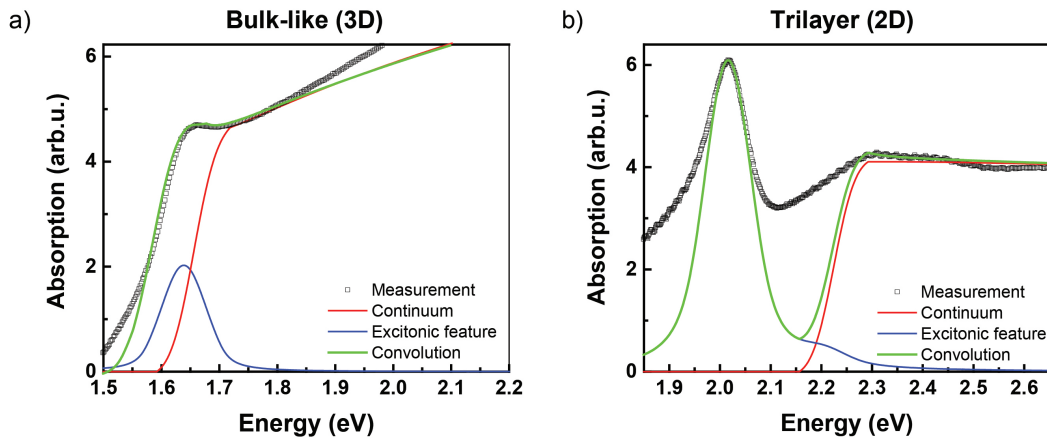


Figure 5.3: Simulations according to Elliott's theory and actual measurements of the absorption spectrum of MAPI NPIs. a) Analysis of the absorption spectrum of a bulk-like NPI dispersion. To simulate the absorption the 3D Elliott formula is applied. The squares show the actual measurement. The calculated contribution of the continuum (red line) and exciton (blue line) and both (green line) according to Elliott's theory is depicted as well. b) Corresponding analysis of the 2D case of a MAPI trilayer dispersion.

In figure 5.3a) the absorption spectrum of bulk-like MAPI NPIs is shown. The dotted line depicts the measured absorption spectrum and the solid lines visualize the calculated absorption spectrum according to Elliott's theory. Additionally, the excitonic contribution and the contribution of the continuum is displayed. The simulation includes the first four excitonic peaks, which are described not as a discrete line but as Lorentzian curves. Both contributions, the one of the excitonic states and the other one of the continuum, are added and convoluted with a Gaussian. The convolution with the Gaussian is implemented to account for inhomogeneous broadening. The obtained simulation nicely fits to the measurement and yields a band gap energy of 1.66 eV and an exciton binding energy of 18.7 meV. The estimations are within the values reported for bulk MAPI. According to literature, the band gap energy of bulk MAPI is at 1.61 eV [50] and the excitonic binding energy lies between 2 meV to 62 meV [89, 161–165]. For higher energies the simulation and actual measurement deviate, and the recorded absorption is higher than the calculation

would suggest. This can be attributed to the absorption into higher bands, which have not been considered in the model. All in all, the absorption measurement of bulk-like NCs is in accordance to the calculation and comparable to measurements performed on MAPI films [166].

The Elliott formula is applied to model the absorption spectrum of MAPI trilayers as well (compare figure 5.3b)). Due to their reduced thickness, they can be considered as a 2D material system, in contrast to the previously discussed bulk-like NPLs, which constitute a 3D system. The calculations according to Elliott's theory result in a band gap energy of roughly 2.27 eV and an exciton binding energy of 230 meV. The comparison of the determined values of E_G and E_B for the bulk-like NPLs and trilayer dispersion displays the induced changes due to quantum confinement. The band gap is energetically shifted by 0.56 eV and the exciton binding energy is increased by a factor of 12. The tremendous increase of E_B can be explained by the reduced screening within the confined platelet due to the dielectric environment outside the semiconductor. Additionally, if the shape of the absorption spectrum regarding the continuum is studied, different trends of the curves are recognizable. Recalling the previous theoretical considerations in section 2.2.2, in which ideal absorption spectra of 2D and 3D semiconductors according to Elliott's theory are discussed, the obtained absorption spectra qualitatively fit to the 3D and 2D case, respectively. For the calculations of the contribution of the continuum, the density of states (D_{CV}^{3D} and D_{CV}^{2D}) is a crucial factor, resulting in a parabolic shaped absorption of the continuum for the 3D case and a constant one for the 2D case. All in all these results fit to values reported in literature [167, 168] and the theoretical calculations from the previous section.

Nevertheless, some divergences between the model and the measurement occur in figure 5.3b). The most evident one observed in the measurement is the increased absorption in the energy range between the excitonic 1s state and the continuum. However, the shape of the continuum can be reproduced nicely. It is important to consider the excitonic states to emulate the measured trend. In the simulation the 1s state is again approximated with a Lorentzian curve. The observed overall raising of the absorption, already starting at energies smaller than the 1s state, is most likely due to scattering. Additionally, other factors are not considered in Elliott's theory, which bases on ideal 3D and 2D semiconductors not on real NPLs with a finite thickness. The mixing of the subbands of the electrons and holes, which affects the electronic band structure, ergo, the absorption, is not included. Moreover, the effective masses of electrons and holes inside and outside the NPLs are unequal. Consequently, the assumption of a constant mass does not describe the situation sufficiently and additional approximations would be necessary to improve the calculation

further. Nevertheless, similar calculations have been conducted for MAPI bilayers yielding an exciton binding energy of 280 meV and a band gap energy of 2.42 eV. In the case of the monolayer the exciton binding energy can only be roughly estimated, since the position of the continuum is not clearly evident in the absorption spectrum. In conclusion an overview of the exciton binding energies is given in table 5.2. All in all, the determined values of the exciton binding and band gap energy are applicable and useful for further considerations.

Number of layers (n)	Exciton binding energy
1	> 300 meV
2	280 meV
3	230 meV
∞	18.7 meV

Table 5.2: Exciton binding energy of MAPI nanoplatelets.

5.2 Tunability of emission by size and composition

The synthesized NPLs show thickness-dependent quantum confinement effects, which are easy to monitor by the change of their color under UV light illumination. To enable a detailed analysis of the effect of quantum confinement, PL and absorption measurements were performed. To draw any conclusion between the reduction of size in one dimension and changes of optical properties, it is necessary to separate perovskite nanoplatelets of individual thickness, which is achieved by several steps of careful centrifugation and dilution.

Figure 5.4a) illustrates a set of MAPI samples separated according to their thickness and illuminated with an UV lamp. All five cuvettes contain MAPI NPLs. To obtain a

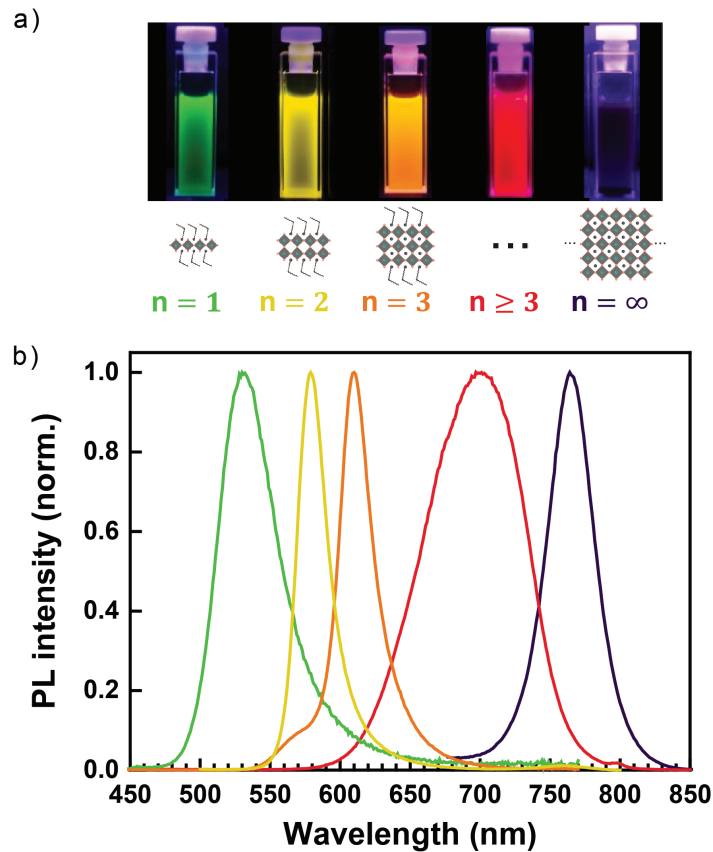


Figure 5.4: PL spectra of MAPI nanoplatelets of individual thickness. a) Images of cuvettes containing MAPI NPL dispersions. The cuvettes are illuminated with UV light and are arranged from left to right with an increasing thickness of the NPLs presented, starting with a monolayer ($n = 1$) and increasing initially stepwise up to a bulk-like value ($n = \infty$). b) Corresponding PL spectra show a shift to smaller wavelengths with decreasing NPL thicknesses. The figure is adopted from Hintermayr et al. [72].

black colored dispersion of bulk-like NPLs is easy, however, to get a dispersion of mono-, bi-, or trilayers is challenging and the procedure must be adjusted individually for every single purification step.

One layer (n) is defined as a network of laterally arranged $[\text{PbI}_6]^{-4}$ octahedra and schematically illustrated in figure 5.4a). In figure 5.4b) the corresponding PL spectra are shown. The PL peak of the bulk-like NPL dispersion is recorded at 765 nm and has a full-width half maximum (FWHM) of only 40 nm. The PL peak positions of the other dispersions are located at 539 nm (green), 579 nm (yellow), 610 nm (orange) and 701 nm (red), respectively. These peak positions of the first three dispersions fit nicely to the values for layered perovskite structures with defined thicknesses of one, two and three unit cells given in literature [12, 168–171]. In the analysis of the TEM images (compare section 4.2) it has already been noted that the red fluorescent sample contains a mixture of different thicknesses of NPLs. The linewidth of the PL peak from the associated PL measurement supports this claim.

As already shown in section 4.2, ligand-assisted exfoliation can also be used to produce mixed halide perovskites. In figure 5.5a) cuvettes illuminated with UV light containing dispersions of methylammonium lead halide perovskites with different halide composition are shown. All of these samples contain bulk-like NPLs and show compelling differences under UV excitation. One can observe a color shift from violet over blue to green, and from green via orange and red to black (infrared), with increasing content of bromide in $\text{MAPbBr}_{3-x}\text{Cl}_x$ and iodide in $\text{MAPbBr}_y\text{I}_{3-y}$, respectively. To qualitatively study this observation and the optical properties, once again the absorption and PL spectra were recorded (see figure 5.5b)). All PL spectra show a single peak. According to the halide content the PL peak position and absorption onset are gradually shifted, from 395 nm (MAPCl) over 525 nm (MAPBr) to 765 nm (MAPI). Hence, the PL emission of the mixed halide perovskite NPLs can be tuned through the entire visible range only by varying the halide content. According to the measurements shown in figure 5.5 the synthesized samples seem to be phase pure, with all containing NPLs exhibiting the same halide ratio. In case NPLs form with different ratios they likely quickly equilibrate to a common halide ion ratio due to rapid ion migration. A similar observation has been made in other studies on perovskite nanoparticles [137, 172–174].

To conclude, the results already presented in this chapter show that one can easily tune the absorption and emission of methylammonium lead halide perovskites by means of size and halide content. A combination of both possibilities of manipulation can be conducted by using the in this work newly established fabrication of lead halide perovskites via ligand-assisted exfoliation. Here the separation of NPLs according to their thickness has

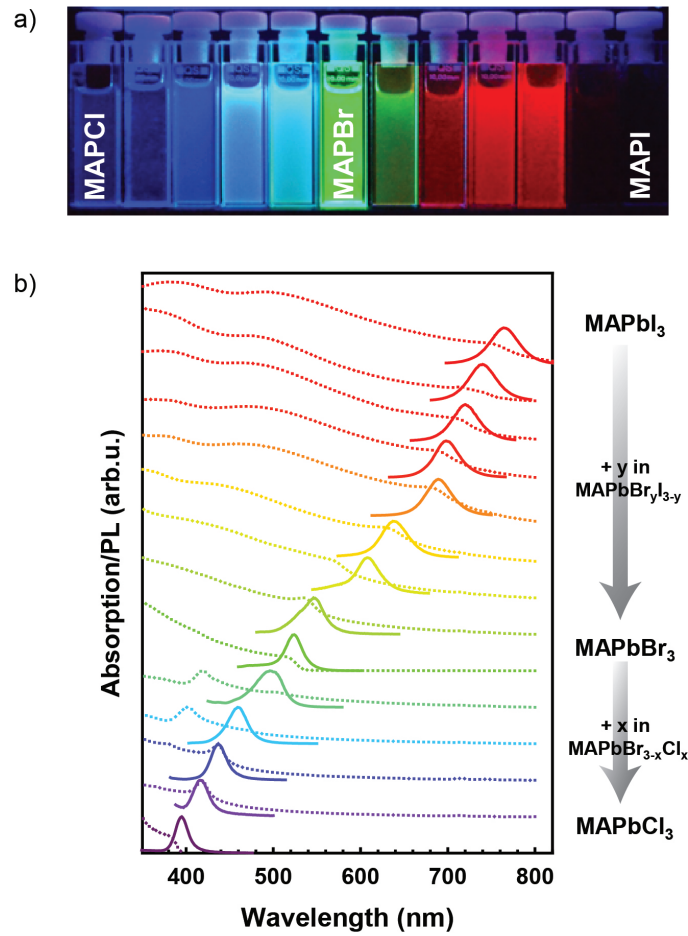


Figure 5.5: Characterization of organic-inorganic lead perovskites with mixed halides

- a) Bulk-like NPI dispersion with different halide content filled in cuvettes and illuminated with UV light. b) Absorption (dotted line) and PL (solid line) spectra of $\text{MAPbBr}_{3-x}\text{Cl}_x$ and $\text{MAPbBr}_y\text{I}_{3-y}$, varying x or y .

been shown for MAPI samples. This routine can be applied to separate any other set of samples, also including mixed halides.

5.3 Temperature-dependent absorption and photoluminescence measurements

The synthesized MAPI NPIs are further investigated at low temperature. Absorption and PL spectra measured at low temperatures can be used to obtain some further information on physical quantities. In contrast to all other optical measurements on perovskite NPIs presented in this thesis, the low temperature studies are not performed in solution but on NPIs drop-casted on a sapphire substrate. First of all, the temperature-dependent absorption of bulk-like NPIs is analyzed and presented in figure 5.6 for the temperature range of 5 K to 295 K. One sees the same trend as observed for MAPI films (compare

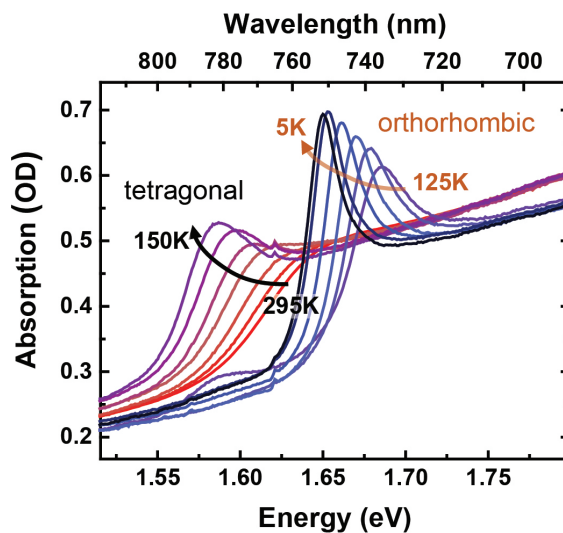


Figure 5.6: Temperature-dependent absorption measurements of bulk-like MAPI NPIs. The temperature is gradually reduced from 295 K to 50 K. Overall a red-shift of the absorption onset is noted. Furthermore, one notices a jump in energy in the range between 125 K to 150 K, which can be attributed to the tetragonal-to-orthorhombic crystal structure phase transition.

section 2.1.4 and [85, 86]). With decreasing temperature, a shift of the absorption to lower energies is recorded. This red-shift is unexpected for a semiconductor, however, it is typical for perovskite films [91, 175, 176] and can be explained by considering their electronic band structure (compare section 2.1.2).

In temperature-dependent absorption measurements, the tetragonal-to-orthorhombic phase transition can be observed. At room temperature MAPI is in the tetragonal phase. With decreasing temperature the movement of the MA^+ cation located in the gaps between the $[\text{PbI}_6]^{-4}$ octahedra is reduced, leading to a different arrangement of the octahedra in respect to each other. The orthorhombic phase is formed. The jump of the absorption

onset, recorded between 150 K and 125 K, is attributed to this phase transition. According to temperature-dependent absorption measurements on MAPI films this phase transition is at 162.2 K (compare section 2.1.4). The phase transition seems to depend on the size or thickness of the analyzed perovskite structures and shifts to a lower temperature with reducing thickness. A similar dependency has already been reported for MAPI microplatelets [177].

In figure 5.7a) temperature-dependent measurements of the PL intensity of a sample containing MAPI NPLs with different thicknesses are shown. The measurement is divided

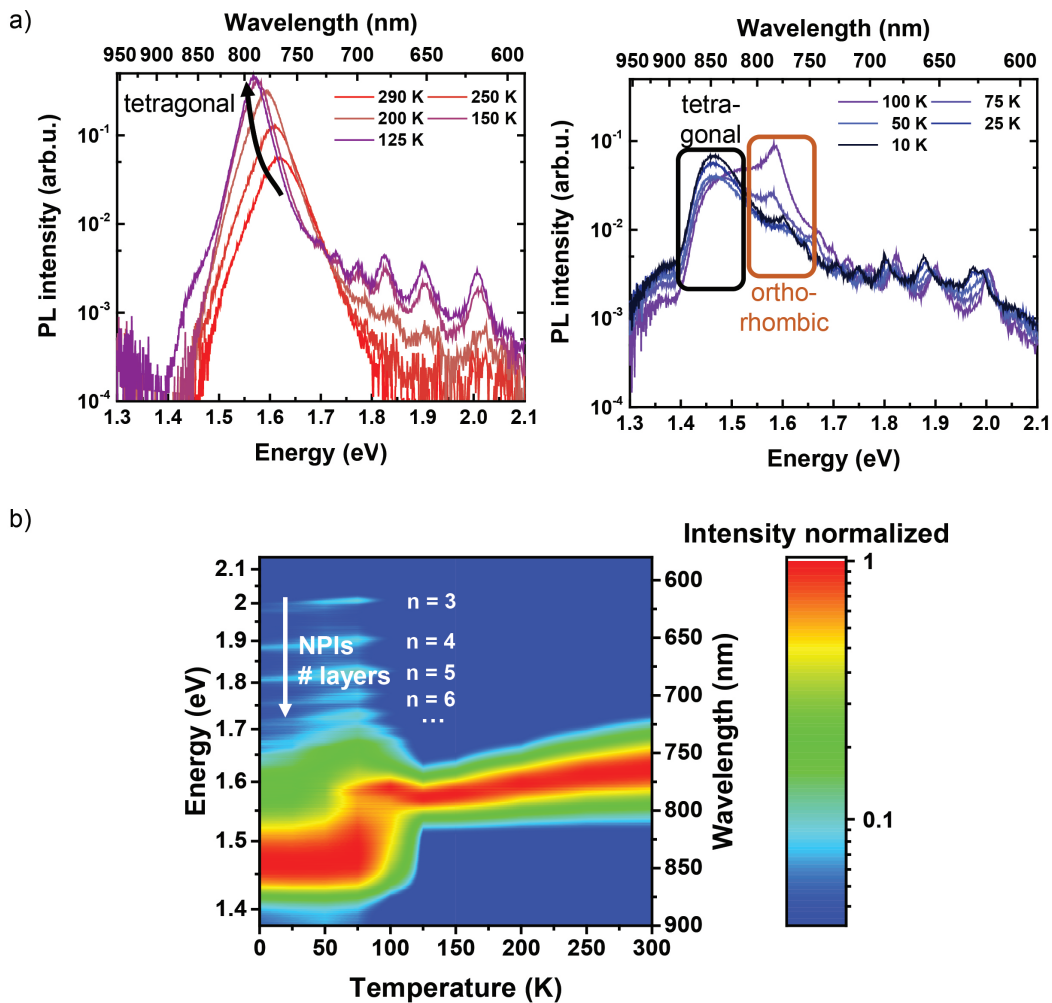


Figure 5.7: Temperature-dependent PL measurements of MAPI NPLs with different thicknesses. a) PL spectrum for temperatures of 290 K to 125 K and 100 K to 10 K, respectively. With decreasing temperature a red-shift of the PL peak is recorded. In the temperature range between 125 K to 100 K the tetragonal-to-orthorhombic phase transition is observed and visible in a sudden jump in PL emission and the appearance of a second peak. The additional peaks appearing at higher energies, can be attributed to quantum-confined structures. b) The same PL measurement illustrated in a color plot.

into two plots with different temperature ranges to provide a clear arrangement. At room temperature a PL emission at 770 nm (1.61 eV) is recorded. Reducing the temperature, a general red-shift of the PL peak is detected. Additionally, in the temperature range between 100 K to 125 K, a second peak appears. These two peaks can be attributed to the tetragonal phase and orthorhombic phase, respectively. The appearance of two peaks is a sign for the coexistence of both phases in the platelets. Contrary to bulk MAPI films, the existence of both phases is still visible at very low temperatures.

In comparison to the temperature-dependent absorption measurements on bulk-like MAPI NPLs, the phase transition temperature of confined nanoplatelets is lower. A size-dependent shift for the phase transition has also been observed in other layered materials [178, 179]. Many different explanations are discussed to interpret the origin of this trend. A plausible reason for this behavior is that with decreasing size of the NPLs the surface-to-volume ratio increases, inducing changes to the surface energies and consequently leading to a lower transition temperature [180].

In figure 5.7b) the measurements are illustrated in a color plot. Here the phase transition is shown more drastically. As the temperature decreases, a gradual shift of the PL peak is recorded. Additionally, one can observe a decrease of the peak width. At approximately 110 K the tetragonal-to-orthorhombic phase transition takes place and the picture drastically changes. Besides the two emission peaks correlating to the coexisting phases, further peaks appear at higher energies. According to previous considerations (compare

Number of layers (n)	Temperature range	PL peak position
1	300 K	539 nm (2.30 eV)
2	300 K	579 nm (2.14 eV)
3	300 K	610 nm (2.03 eV)
3	10 K	628 nm (1.97 eV)
4	10 K	661 nm (1.88 eV)
5	10 K	688 nm (1.80 eV)
6	10 K	710 nm (1.75 eV)
7	10 K	727 nm (1.71 eV)
8	10 K	742 nm (1.67 eV)

Table 5.3: Phase transition temperatures and lattice parameters for MAPI according to Baikie et al. [88].

section 5.1) one can attribute the PL peaks to thin NPLs. An overview of the obtained values is given in table 5.3, providing for the first time experimentally values for NPLs with

up to $n = 8$ layers. In the table one should distinguish between the values obtained at low temperatures (10 K) and at room temperature (300 K). These determined values are used to check the theoretical considerations presented in section 5.1. All in all, the quantum confinement calculations in section 5.1.1 are consistent with the PL measurements presented in this chapter by taking into account the determined exciton binding energies (compare section 5.1.2).

Carrier dynamics in 2D and 3D MAPI nanoplatelets: Excitons versus free carriers

To enable optical studies on ultrafast dynamics of charge carriers in a semiconductor lattice, the usage of a pulsed laser is necessary, which exhibits a pulse length on a time scale shorter than the inspected processes. Femtosecond lasers are ideally suited for this purpose. In the following chapter transient absorption spectroscopy (TAS) and time-resolved PL measurements on MAPI NPLs with different thicknesses are investigated.

By means of TAS, changes in absorption induced by a first laser pulse and probed by a second pulse are analyzed, providing information on charge carrier densities, hot carrier cooling dynamics, the exciton binding energy and the interplay between free carriers and excitons. Additionally, time-resolved PL measurements and the effect of the platelet thickness on excitonic decay times are investigated. These measurements reveal an increased exciton recombination rate with decreasing crystal thickness.

6.1 Transient absorption spectroscopy measurements

Utilizing TAS measurements, one can probe and characterize the electronic and structural properties of short-lived excited states. The investigation of time-dependent charge distributions within the relevant excited states provides a greater insight into charge carrier dynamics and shows the traces of progression through the states. The TAS measurements presented here were performed with a custom-built pump-probe setup (see section 3.2.2). In this setup a first laser pulse (pump) excites the perovskite crystal and certain initial conditions are created. A second laser pulse (probe) is subsequently used to record the changes, evolving with time. In the comparison of 3D and 2D MAPI NPLs, noted differences due to the reduced dimensionality are of special interest and are evaluated in the following.

As described in section 5.2, a separation of MAPI NPLs according to their thickness succeeded. This allows to perform thickness-dependent time-resolved spectroscopy on MAPI NPLs. In the following TAS investigations are conducted on monolayers, trilayers and bulk-like NPLs ($n = 1, 3$ and ∞) with respective thicknesses of roughly 0.7 nm, 2 nm and more than 10 nm. Since the thickness of the MAPI mono- and trilayer platelets is in the range of the excitonic Bohr radius (for this material approximately 3 nm [181]), quantum confinement effects need to be considered and these samples are referred to as 2D materials. All TAS measurements were performed at room temperature and the colloidal NPLs were dispersed in toluene.

6.1.1 Linear and transient absorption of MAPI nanoplatelets

First of all, the in figure 6.1a) shown steady-state and TAS spectra of bulk-like NPLs and MAPI monolayers are analyzed. In the pump-probe experiments an excitation wavelength of 400 nm and a photon fluence of $360 \mu\text{J} \cdot \text{cm}^{-2}$ were used. In case of the bulk-like NPLs a minimum of ΔOD is recorded at 760 nm (1.64 eV). In the steady-state absorption one can observe an absorption onset at roughly this position. Additionally, a second minimum is detected in the TAS spectrum at 490 nm (2.53 eV). As presented in section 2.1.3, these minima around 760 nm and 490 nm can be attributed to the multiband character of the electronic band structure of MAPI. In figure 6.1b) a simplified sketch of the possible multiband structure is shown. In this sketch the effect of band gap renormalization (BGR) is illustrated, which occurs due to photoinduced changes in the exchange corrections to the electronic energy (compare section 2.3.3). Due to BGR new states are created at energies, slightly lower than the band gap energy. This leads to a reduced band gap and an enhanced

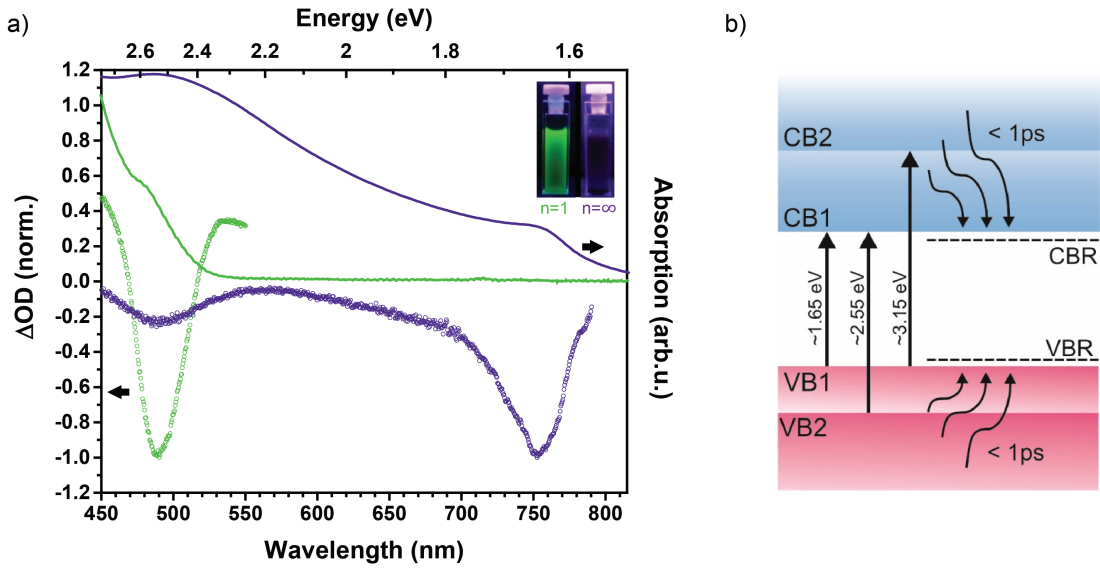


Figure 6.1: Steady-state and transient absorption spectra of MAPI NPIs. a) The absorption and TAS of bulk-like NPIs (3D, purple lines and circles) and a monolayer dispersion (2D, green lines and circles). The TAS spectra are recorded at a delay time corresponding to the maximal signal. b) Scheme of the MAPI (3D) band structure. The labeled transition corresponds to the observed photoinduced bleaching (PIB). The PIB at 394 nm (3.15 eV) is not within the recorded spectral range, but has been reported in literature (see Anand et al. [182]). The conduction band renormalization (CBR) and the valence band renormalization (VBR) caused by photoinduced changes is depicted, as well.

absorption of photons with energies suitable to these states. BGR is commonly observed in methylammonium lead halide perovskite films [166, 183].

The steady-state absorption measurement of the monolayer dispersion reveals an increase of absorption for wavelengths smaller than 520 nm. At roughly the same position, the TAS spectrum exhibits a minimum, equivalent to a reduced absorption. This feature can be attributed to the 1s excitonic state and in the recorded TAS spectrum the bleaching of this state is observed. Generally, a strong energetic blue-shift in absorption is recorded for monolayers compared to bulk-like NPIs, which can be attributed to quantum confinement as examined in the previous chapter. As expected for semiconductors, by decreasing the dimensionality of nanostructure an increase of the band gap energy is induced.

6.1.2 State filling: Analysis of the continuum and excitonic state

The monolayer and bulk-like samples were studied in more detail by performing charge carrier density-dependent TAS measurements. Again, the excitation wavelength was set to 400 nm and the photon flux was gradually increased. A corresponding amplification of the

differential transmission signal, located at 760 nm (bulk-like, 3D) and 490 nm (monolayer, 2D), was observed as it is depicted in figure 6.2a) and b).

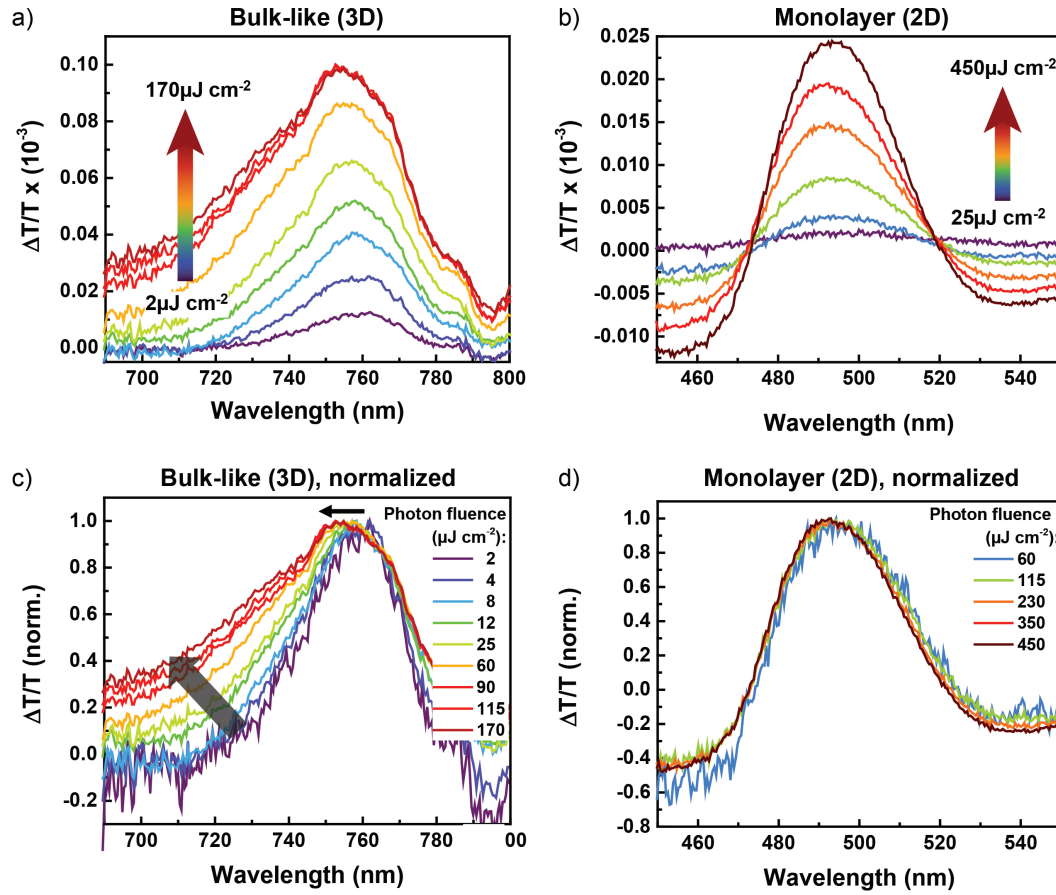


Figure 6.2: Pump pulse intensity-dependent TAS spectra of 3D and 2D MAPI NPIs.

Each of the spectra is taken at maximal $\Delta T/T$ signal. The excitation wavelength is set to 400 nm. a) A rise of the ground state bleaching corresponding to the increased pump laser intensity is observed in the case of bulk-like NPIs. The photon fluence of the pump pulse is enhanced stepwise ($2 \mu\text{J} \cdot \text{cm}^{-2}$, $4 \mu\text{J} \cdot \text{cm}^{-2}$, $8 \mu\text{J} \cdot \text{cm}^{-2}$, $12 \mu\text{J} \cdot \text{cm}^{-2}$, $25 \mu\text{J} \cdot \text{cm}^{-2}$, $60 \mu\text{J} \cdot \text{cm}^{-2}$, $90 \mu\text{J} \cdot \text{cm}^{-2}$, $115 \mu\text{J} \cdot \text{cm}^{-2}$, $170 \mu\text{J} \cdot \text{cm}^{-2}$). b) Gradual increase of the photon fluence of pump pulse ($25 \mu\text{J} \cdot \text{cm}^{-2}$, $60 \mu\text{J} \cdot \text{cm}^{-2}$, $115 \mu\text{J} \cdot \text{cm}^{-2}$, $230 \mu\text{J} \cdot \text{cm}^{-2}$, $350 \mu\text{J} \cdot \text{cm}^{-2}$, $450 \mu\text{J} \cdot \text{cm}^{-2}$) and associated change in transmission detected for a MAPI monolayer dispersion. c) Normalized graph a), illustrating band filling and a blue-shift of the peak position as the charge carrier density is increased. d) Normalized graph b), no charge carrier density dependence is recorded.

The pump pulse photons hit the sample and generate photoexcited charge carriers of a certain density. It is not trivial to determine this density, since the NPIs exhibit different lateral sizes, rendering a proper estimation without further investigations extremely difficult. Furthermore, due to the repetitive steps of centrifugation and dilution, the density of the monolayers is strongly reduced compared to the one of bulk-like NPIs in solution and is not clearly defined. Here, the stated photon fluences support qualitative comparisons

for measurements on the same sample, assuming a charge carrier density directly linked to the number of incident pump photons.

Besides induced changes in transmission, additional carrier density-dependent effects are noticeable. Plotting the TAS spectra, normalized to the maximum, a striking difference between the 3D and 2D case is observable. In figure 6.2c) the graph, normalized to the ground state bleach (GSB) of the continuum for the 3D case is shown. For low energies, the recorded TAS signal exhibits a symmetrically shaped peak. With increasing photon fluences a shoulder on the high energy side arises, which becomes more and more pronounced as the density is enhanced. Furthermore, the peak position of the GSB shifts slightly to higher energies. Regarding density-dependent measurements of the monolayer sample, hardly any change of the shape for different excitation densities is observed (see figure 6.2d)). The broadening at the high energy side and the blue-shift of the peak position can be attributed to band filling as described in section 2.3.3 and has been observed for perovskite films as well [97]. At higher photon fluences more charge carriers are excited. Due to the Pauli exclusion principle the states close to the fundamental band gap become filled and energetically higher states are occupied. Consequently, the transmission of the probe pulse at this energy range is increased. Also, the corresponding blue-shift of the peak position originates from the gradual filling of the states at the vicinity of the conduction and valence band edges.

The observed wavelength range in 6.2b) and d) only depicts the population of the 1s excitonic state in MAPI monolayers. The 1s excitonic state is a distinct energy state and a carrier density independent transmission without the observation of band filling is expected. For a certain density a jump to the next higher energy state is theoretically anticipated, yet not recorded, since too high laser powers induce degradation of the sample and make an excitation with such high photon fluences impossible.

6.1.3 Recombination mechanism in 3D and 2D MAPI nanoplatelets

In the next part the recombination mechanisms of photogenerated charge carriers in MAPI NPLs are investigated. General details on recombination dynamics in semiconductors can be found in section 2.3.2. Figure 6.3a) and b) show the obtained kinetics of bulk-like NPLs and monolayer dispersions, recorded at maximal differential transmission. For the bulk-like NPLs a dependence on the charge carrier density is observed. The more photoexcited charge carriers are created, the faster the recombination proceeds and the bleach recovers. The rate equation (2.19) enables a modelling of the kinetics. Provided that mainly free carriers are created, the effect of trap states can be neglected and only relatively low photon fluences are used, one can simplify the rate equation by setting k_1 and k_3 equal to zero. k_1 is the

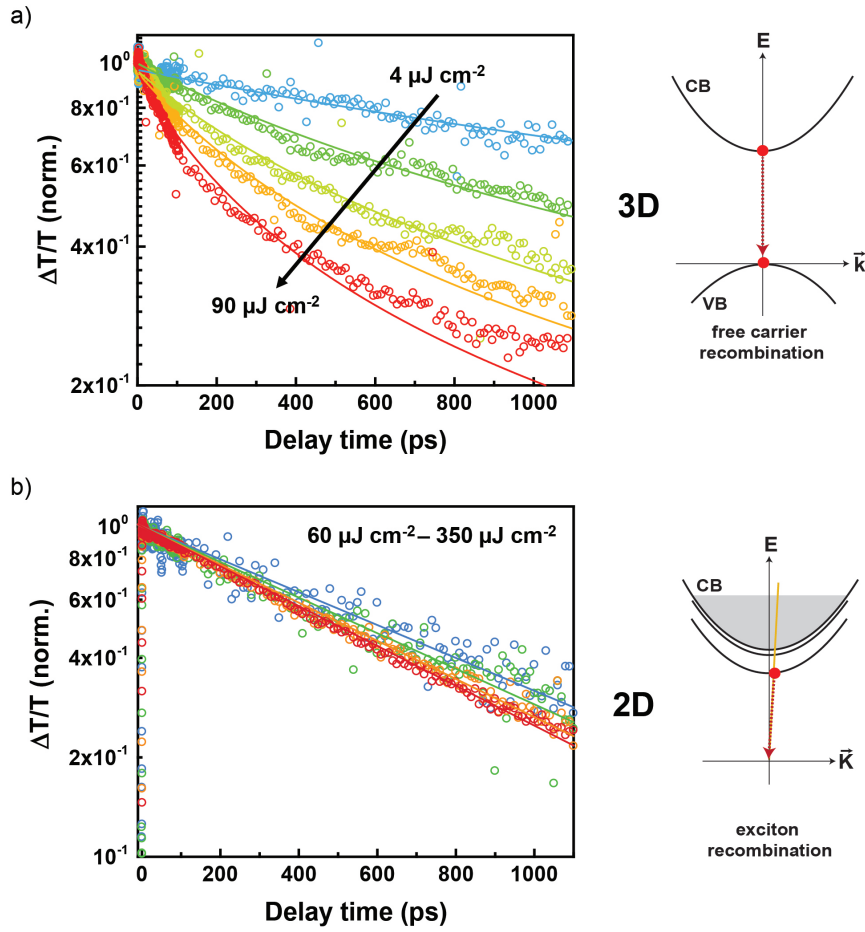


Figure 6.3: Kinetic profiles at maximal $\Delta T/T$ signal. The excitation wavelength is set to 400 nm. a) Normalized kinetic profile for bulk-like NPs (3D) with gradually increasing photon fluence ($4 \mu\text{J} \cdot \text{cm}^{-2}$, $12 \mu\text{J} \cdot \text{cm}^{-2}$, $25 \mu\text{J} \cdot \text{cm}^{-2}$, $60 \mu\text{J} \cdot \text{cm}^{-2}$, $90 \mu\text{J} \cdot \text{cm}^{-2}$). As the carrier density increases, the recombination process quickens. The solid lines show a determined fit function, based on the assumption of pure bimolecular recombination. For higher laser densities, discrepancies occur due to the increasing impact of the three body Auger recombination. On the schematic picture on the right, the bimolecular recombination of free carriers in the one particle picture is illustrated. b) For the monolayer sample (2D) no charge carrier density dependence was observed and the kinetic profiles describe a monomolecular recombination, illustrated in the two particle picture, suited for excitons, on the right.

rate of monomolecular recombination and it is dominant for the recombination mechanism of excitons or trap state-mediated recombination. The rate of the Auger recombination is given by k_3 . The contribution of this three-body interaction can be neglected for small charge carrier densities. Therefore, one obtains a simplified rate equation, given by:

$$-\frac{dn}{dt} \approx k_2 \cdot n^2, \quad (6.1)$$

with the charge carrier density n and the bimolecular recombination rate k_2 . This differential equation can be easily solved and one obtains:

$$n \propto \frac{1}{t}. \quad (6.2)$$

The differential transmission reflects the photogenerated charge carrier density, hence, the resulting proportionality can be used to fit the kinetic profiles shown in figure 6.3a). The resulting fitting curves are illustrated as solid lines in this graph. Especially for low densities, the assumption of a pure bimolecular recombination is sufficient to reproduce the recorded kinetics. For higher laser intensities, the model and the actual measurement slightly deviate from each other. An explanation of this discrepancy is an enhanced Auger recombination with increasing number of photogenerated charge carriers. Consequently, k_3 is unequal zero and needs to be considered, as well. However, in the case of bulk-like MAPI NPLs, the bimolecular recombination rate related to free carriers is the dominate process, similar to MAPI films [21, 105, 184]. In MAPI films free carriers are dominant even at low temperatures, as it has been demonstrated in temperature-dependent TAS measurements [185].

The charge carrier density-dependent kinetics of the maximum $\Delta T/T$ signal, recorded in the TAS measurements of the MAPI monolayer dispersion, are shown in figure 6.3b). Here, it is assumed that the recombination mechanism is governed by the recombination of excitons, thus, k_2 and k_3 can be set to zero. The simplified rate equation is given by:

$$-\frac{dn}{dt} \approx k_1 \cdot n, \quad (6.3)$$

providing the relation

$$n \propto \exp(-k_1 \cdot t). \quad (6.4)$$

Figure 6.3b) reveals that the logarithmically plotted kinetic profiles are in accordance with the equation (6.4). As expected, the kinetics are independent of the photon fluence of the pump pulse.

To simplify a comparison regarding the recombination times, the $1/e$ values of the $\Delta T/T$ signal are extracted. Figure 6.3a) demonstrates the dependence of the recombination time of bulk-like NPLs on the charge carrier density. According to the rate equation (6.1) and the assumption of a pure bimolecular recombination mechanism, the determined recombination times are given by 4220 ps, 1635 ps, 955 ps, 675 ps and 435 ps for a set photon fluences of $4 \mu\text{J} \cdot \text{cm}^{-2}$, $12 \mu\text{J} \cdot \text{cm}^{-2}$, $25 \mu\text{J} \cdot \text{cm}^{-2}$, $60 \mu\text{J} \cdot \text{cm}^{-2}$ and $90 \mu\text{J} \cdot \text{cm}^{-2}$. In the measurements of the monolayer dispersion shown in figure 6.3b), only minor deviations are noticeable and the approximated recombination time is in the range of 750 ps to 900 ps. Since two different processes are observed, the recombination of free carriers and excitons,

a direct comparison would be misleading. However, these considerations provide an insight into the expected time range of the recombination processes. All in all, the recombination dynamics exhibit the dominant role of excitons in 2D NPLs and free carriers in 3D NPLs.

6.1.4 Hot carrier cooling in 2D and 3D perovskite nanoplatelets

As mentioned in the theory part (see section 2.3.1), the relaxation of photoexcited charge carriers can be divided in four different temporal regimes. The recombination is the dominant process in the last of these regimes, the isothermal regime. It is reached as soon as the charge carriers and the lattice are in equilibrium and has been analyzed in the previous section. In the following, the cooling behavior of hot carriers in 2D and 3D MAPI NPLs is of interest and therefore the third regime, the hot-excitation regime, is investigated. To study the cooling of hot charge carriers, TAS measurements with a pump wavelength of 400 nm (3.1 eV) were conducted. Since the energy of the photons from the pump laser is much higher than the band gap energy of the perovskite nanostructure, hot carriers are created which subsequently cool down by scattering mainly with longitudinal optical (LO) phonons.

Figure 6.4a) illustrates the absorption and PL spectra of MAPI trilayers (2D) and MAPI bulk-like NPLs (3D). In contrast to the MAPI monolayers, the energetic position

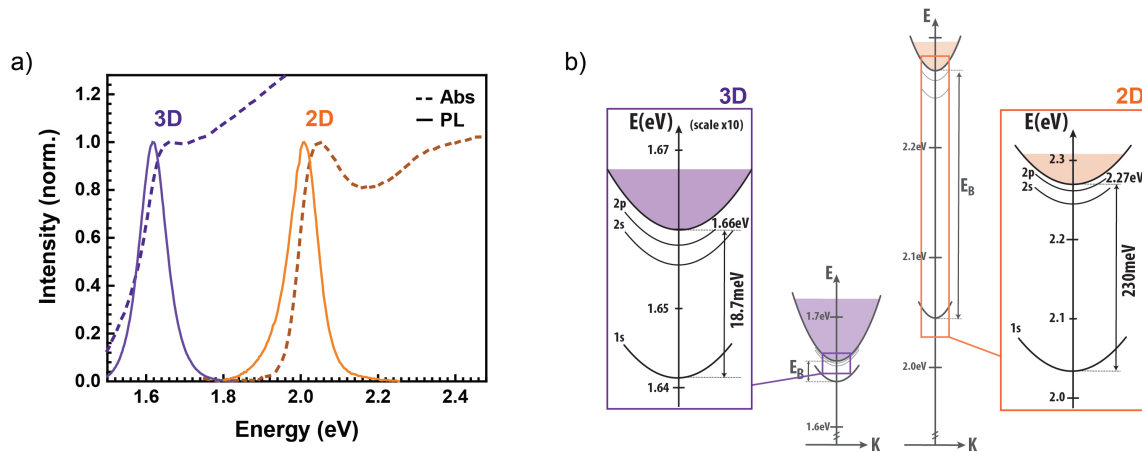


Figure 6.4: Energy levels of 3D and 2D MAPI NPLs. a) Absorption and PL spectra of MAPI bulk-like NPLs (3D) and trilayers (2D). In the absorption of the bulk-like NPLs a small bump at the onset is a noticeable indication of the excitonic contribution. The PL and absorption of the MAPI trilayers are shifted to higher energies due to quantum confinement and a clear excitonic contribution is distinguishable. b) Schematic energy diagrams of the different states according to Elliott's theory for the 3D and 2D samples, respectively.

of the continuum of trilayers is within the range of the probed spectrum. The steady-state absorption spectra of MAPI trilayers and bulk-like NPLs are analyzed according to

Elliott's theory in section 2.2. The resulting energy diagrams are shown in figure 6.4b). The comparison of the energetic levels of both samples reveals two main differences which are important for further considerations. First of all, as shown in the sketch the band gap of the 2D material is much larger than the one of the 3D sample. Secondly, the exciton binding energy of MAPI trilayers is strongly enhanced compared to the one of bulk-like NPLs. For MAPI trilayers E_B is 230 meV and a band gap of 2.27 eV was determined. The calculated exciton binding energy of bulk-like NPLs is 18.7 meV and the band gap energy is 1.66 eV.

Figure 6.5a) depicts the normalized transient absorption of the 3D sample for delay times between 0.5 and 30 ps. The dynamics of the charge carriers are recorded as a

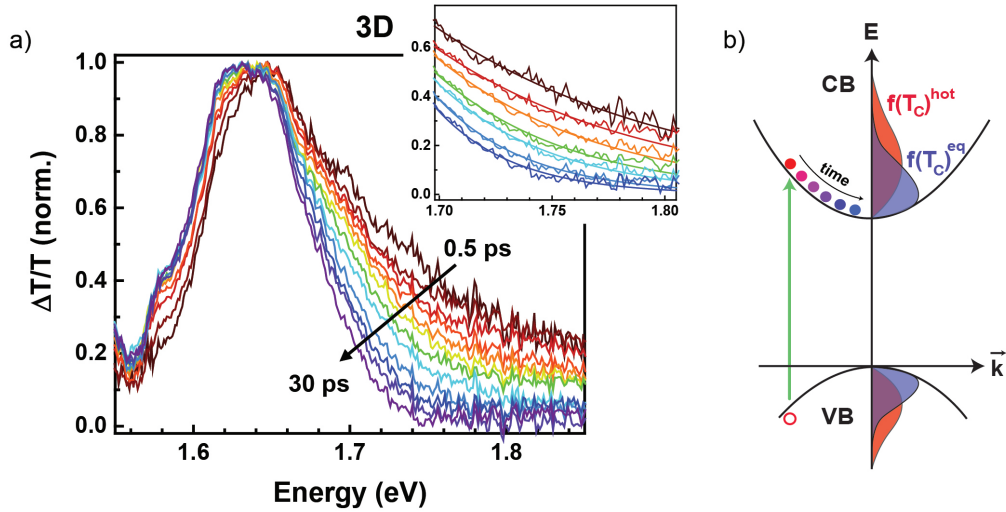


Figure 6.5: Normalized TAS spectra of bulk-like (3D) MAPI NPLs. a) The normalized change of transmission shows a broad high energy shoulder at early delay times. This shoulder decreases as hot carriers from higher states, cool down to energetic lower states. In the inset on the top right, a fit according to the Maxwell-Boltzmann distribution is applied in order to obtain the temperature of the carriers at different time delays. b) Schematic illustration of the cooling of photoexcited hot carriers in the one particle picture. The distribution of the thermalized hot carriers is given by $f(T_C)^{\text{hot}}$ and characterized by a certain temperature T_C . Over time the hot carriers cool down by emitting optical phonons and populate states at the vicinity of the band edge. Their distribution is described by $f(T_C)^{\text{eq}}$ with a temperature close to room temperature. The hole undergoes an analogous process.

function of time and wavelength using a white light spectrum to probe the changes in absorption. A pump pulse of 400 nm and a photon fluence set to $360 \mu\text{J} \cdot \text{cm}^{-2}$ is applied. The peak exhibits an asymmetrical shape and a high energy tail at early times, which decreases with increasing time delays between pump and probe. Gradually, a more and more symmetric shape and a reduction of the high energy tail is recorded. This reflects

the cooling of the charge carriers and has also been analyzed for MAPI films revealing a similar behavior [183]. In order to visualize the cooling process, figure 6.5b) shows a schematic image of the carrier cooling. The excitation energy exceeds the band gap energy by 1.44 eV, therefore, hot carriers are created. The red circle in the sketch represents these photogenerated charge carriers. Hence, at very early delay times higher energy states are occupied, causing the observed asymmetrical shape of the $\Delta T/T$ peak. Within only a few tens of femtoseconds, these hot charge carriers are thermalized and their distribution $f(T_C)^{\text{hot}}$ can be characterized by a certain temperature T_C . After thermalization, the carriers scatter inelastically with optical phonons and occupy energetically lower/higher states at the edge of the conduction/valence band. Consequently, the high energy shoulder diminishes and the distribution of the carriers can now be described with $f(T_C)^{\text{eq}}$ which is also sketched in figure 6.5b).

The corresponding TA spectra of MAPI trilayers, illustrated in figure 6.6, show a different behavior. The maximum changes in transmission are observed around 2.04 eV,

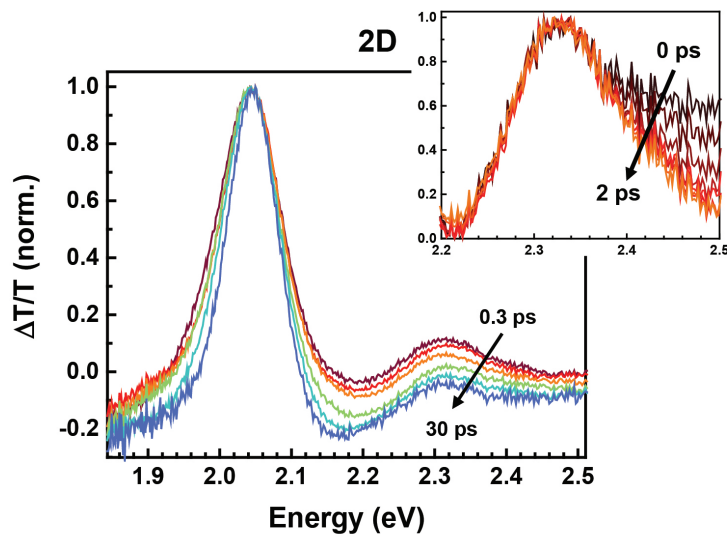


Figure 6.6: Normalized TAS spectra of a MAPI trilayer (2D) dispersion. In the normalized TAS spectra at early delay times (0.3 ps - 30 ps) two main features are noted. At 2.04 eV the bleaching of the excitonic 1s state is recorded and at roughly 2.31 eV the signature of the continuum is observable. The inset shows the same measurement normalized to the continuum. Here, the cooling of the charges is clearly visible and an equilibrium between lattice and carriers is created only within a few picoseconds.

the position of the excitonic 1s state. In contrast to the continuum, the recorded bleaching of the excitonic state is evident in a symmetric shaped peak. The FWHM of the signal reduces over time. This sharpening is due to exciton-exciton interaction and subsequent redistribution. As expected for excitons, the peak position is time independent. Besides

the feature corresponding to the excitonic absorption an additional peak is recorded at roughly 2.27 eV which can be attributed to the continuum. It is less pronounced than the excitonic feature and only recognizable for early times. Yet, in the analysis of the continuum one can observe a broader asymmetrical high energy tail as well. This tail vanishes within less than 2 ps (compare inset of figure 6.6).

The carrier cooling in 2D and 3D can be investigated by studying the recorded high energy tail of the continuum absorption. By elastic scattering with each other the photoexcited carriers thermalize. The gained Fermi Dirac distribution function can be described by a certain carrier temperature T_c which is extracted by approximation with a Boltzmann distribution, yielding [166, 183]:

$$\frac{\Delta T}{T} \propto \exp\left(-\frac{\hbar\omega}{k_b T_c}\right). \quad (6.5)$$

To be able to apply this fit one must assume, that (i) the differential transmission is proportional to the change of the absorption coefficient, (ii) one can indeed describe the carrier distribution as a Boltzmann distribution and (iii) the density of states stays roughly constant in the analyzed region. A sufficient small laser intensity is used to ensure the validity of (i), additionally the accuracy of the fit applying Boltzmann distribution was checked and no changes of DOS was observed in controlled absorption measurements.

Since the carriers cool down by emitting optical phonons, the temperature T_c gradually decreases. By plotting the charge carrier temperature versus time, the cooling curves of the materials are obtained. In order to extract the actual temperature, one needs to consider the linewidth of the signal itself and subtract it, to gain only the broadening of the signal due to the increased charge carrier temperature. The shape of the signal without the broadening due to hot carriers can be determined by modeling the low energy part of the peak.

The bulk-like (3D) and the trilayer (2D) samples were pumped at 400 nm in order to analyze the TAS spectra at the range of the continuum. According to the varying band gap energies, the energy difference between pump and band gap yields 1.44 eV or 0.83 eV, respectively. Due to this difference the theoretical temperature of the photogenerated carriers directly after the pump pulse are dissimilar. Figure 6.7 displays the delay time-dependent charge carrier temperature T_c , measured for bulk-like NPLs and MAPI trilayers, excited with the same photon fluence of $350 \mu\text{J} \cdot \text{cm}^{-2}$. After a certain time an equilibrium between charge carriers and phonons is reached and the charge carriers have a temperature of roughly 300 K. This temperature value is indicated in figure 6.7 as a grey dashed line. One apparent difference between the cooling curves of 3D and 2D MAPI NPLs is the huge discrepancy in the time the charge carriers need to equilibrate with the lattice. The cooling

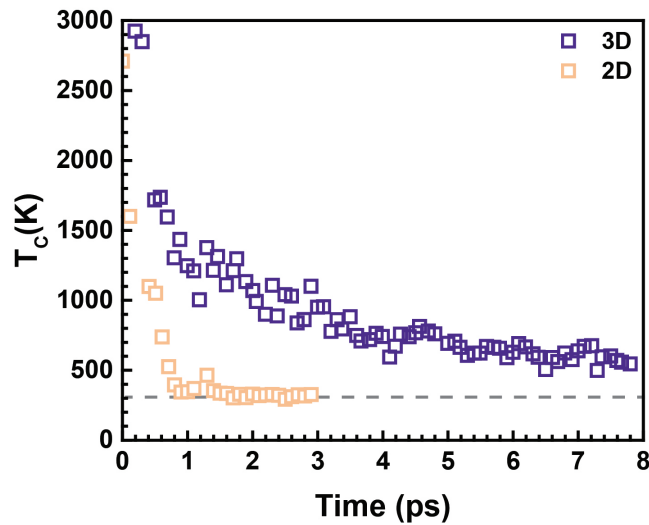


Figure 6.7: Comparison of cooling curves of 3D and 2D MAPI NPIs. For both measurements the excitation wavelength was set to 400 nm and a photon fluence of $350 \mu\text{J} \cdot \text{cm}^{-2}$ was used. In the comparison of both cooling curves a huge time discrepancy is noticed. In case of trilayers (pale pink squares) an equilibrium between charge carriers and phonons is reached after 1.4 ps, for bulk-like NPIs (purple squares) a cooling time of 14.8 ps is determined.

of the charge carriers in a MAPI trilayer dispersion is much faster than the corresponding process in the bulk-like NPIs. In 2D the charge carriers reach a temperature of roughly 300 K (room temperature) circa 1.4 ps after the photoexcitation. On the contrary, in 3D the cooling time is roughly 14.8 ps and therefore about 15 times as long as for 2D. Considering semiconductor nanostructures one may expect an opposite behavior. Due to quantum confinement the DOS of the electrons and the number of phonon modes are reduced. Additionally, the spacing of the electronic levels in nanostructures increases [71]. Consequently, a match of phonons to the electronic energy gaps is less likely. According to these considerations, a higher cooling rate for 3D materials compared to 2D is expected and is observed for some semiconductor NCs [186–188].

In figure 6.8a) and b) photon fluence-dependent cooling curves of the two samples are presented. Analyzing these graphs another difference is observed. In the measurement of bulk-like NPIs, illustrated in figure 6.8a), a clear correlation between carrier density and cooling time is observed. As the photon fluence, ergo the charge carrier density, is gradually enhanced from $70 \mu\text{J} \cdot \text{cm}^{-2}$ to $140 \mu\text{J} \cdot \text{cm}^{-2}$ to $350 \mu\text{J} \cdot \text{cm}^{-2}$, the time until T_c reaches 300 K increases from roughly 2.4 ps to 12 ps to 14.8 ps, respectively. In contrast to the 3D case, the corresponding measurements for 2D NPIs reveal no link between photon fluences and cooling times (see figure 6.8b)). For all used photon fluences ($350 \mu\text{J} \cdot \text{cm}^{-2}$, $700 \mu\text{J} \cdot \text{cm}^{-2}$ and $1050 \mu\text{J} \cdot \text{cm}^{-2}$) a time of roughly 1.4 ps was recorded.

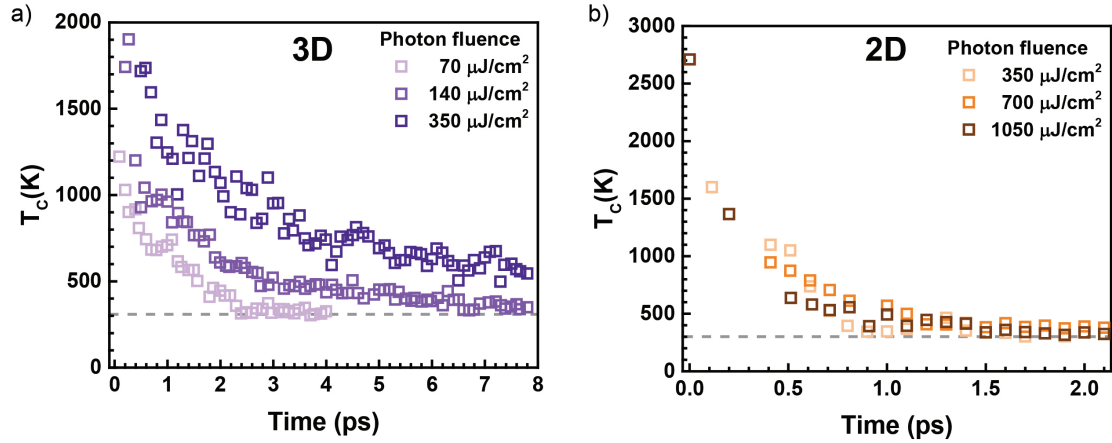


Figure 6.8: Delay time-dependent charge carrier temperature in 3D and 2D MAPI NPIs. a) Cooling curves of bulk-like MAPI NPIs excited at 400 nm. With increasing power fluence the cooling time increases, as well. b) Cooling curves of a trilayer dispersion. In the 2D case no correlation between photon fluence and cooling time is observed. Furthermore, the cooling time is significantly shorter than in the 3D material.

The observations regarding the cooling curves can be understood by considering that the analyzed systems exhibit some crucial differences compared to semiconductor nanostructures like quantum wells. The inspected MAPI NPIs are dissolved in a solvent, namely toluene, and stabilized by a ligand and not embedded in another semiconductor. In figure 6.9 a schematic illustration of the situation in hand for the 2D and 3D case is illustrated. As the surface-to-volume ratio of the bulk-like NPIs is rather small compared to the 2D ones, the effect of the surrounding medium is less dominant and measurements of these are comparable to those of MAPI films. However, in the 2D case the effect of the surrounding medium needs to be considered, especially since the screening of the Coulomb interaction depends on the dielectric environment. In general, the scattering of charge carriers and LO-phonons can be considered as the interaction of a monopole and a dipole described by the Fröhlich interaction [189]. According to this theory the screened coupling constant increases as the dielectric constant is reduced. The dielectric constant of MAPI is bigger than the one of the surrounding medium, hence, the long-ranged Coulomb interaction is screened more effectively in the bulk-like NPIs. Consequently, a lower coupling constant, thus scattering rate than for 2D NPIs can be observed. This in turn results in a slower cooling process in 3D MAPI NPIs.

Another difference is that in contrast to the bulk-like NPIs for the trilayer dispersion no correlation between the charge carrier temperature and density is observed. To explain this observation, one again has to consider the surrounding of the NPIs. In general, hot carriers cool down by emitting a cascade of optical phonons. These optical phonons decay

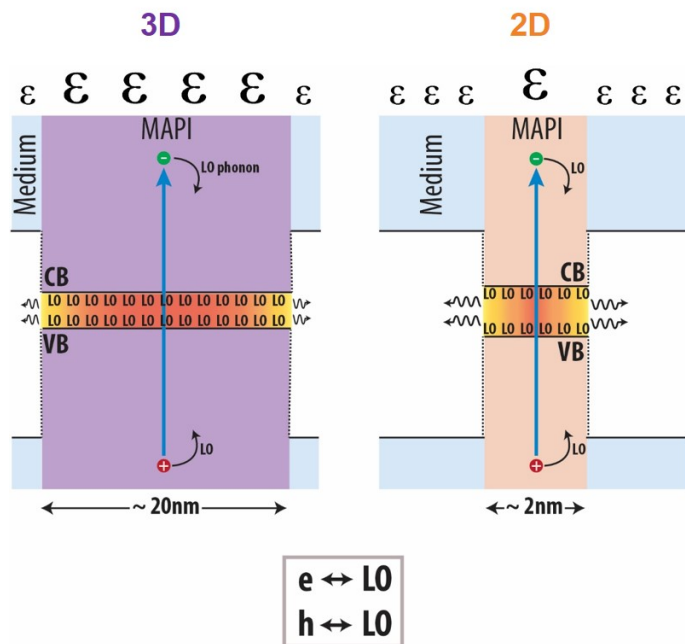


Figure 6.9: Schematic illustration of cooling process in 2D and 3D NPIs. The MAPI NPIs are surrounded by a medium, oleylamine and toluene. After photoexcitation the initial hot electrons and holes cool down to the band edges by mainly emitting LO-phonons. In the schema the 3D and 2D case is illustrated.

within a certain time by emitting acoustic phonons. Naturally, LO-phonons can also be reabsorbed by the charge carriers which are heating up again. The higher the LO-phonon density, the more likely this process is to happen, leading to an overall longer cooling process. The reabsorption of phonons and consequently prolongation of the cooling time is known as the hot phonon effect [190] and has generally been monitored in inorganic crystalline semiconductors [191, 192]. It is also observed in measurements on MAPI films [21, 183]. In the case of 2D NPIs the surface-to-volume ratio is much larger than in 3D NPIs, therefore, the LO-phonons can more effectively dissipate to the cooler surrounding medium. They can for example be transferred to vibrational modes of the ligands and the relaxation mechanism is likely dominated by the vibrations of the surface ligand [193, 194]. In other words, the optical phonons likely 'escape' faster to the cooler surrounding than they can be reabsorbed. Therefore, no hot phonon effect is observed in 2D NPIs and the intensity-dependent cooling curves look nearly identical.

6.1.5 Dissociation of excitons in MAPI nanoplatelets

The tunable excitation wavelength enables a resonant excitation of the excitonic 1s state. According to section 5.1.2 the band gap energy of the 3D NPIs is 1.66 eV and the excitonic 1s state is located at 1.64 eV. In the following experiments the samples is pumped either

in resonance to the excitonic state at a wavelength of 758 nm (1.64 eV) or non-resonantly at 565 nm (2.19 eV). The resulting kinetics are illustrated in figure 6.10 a). When exciting

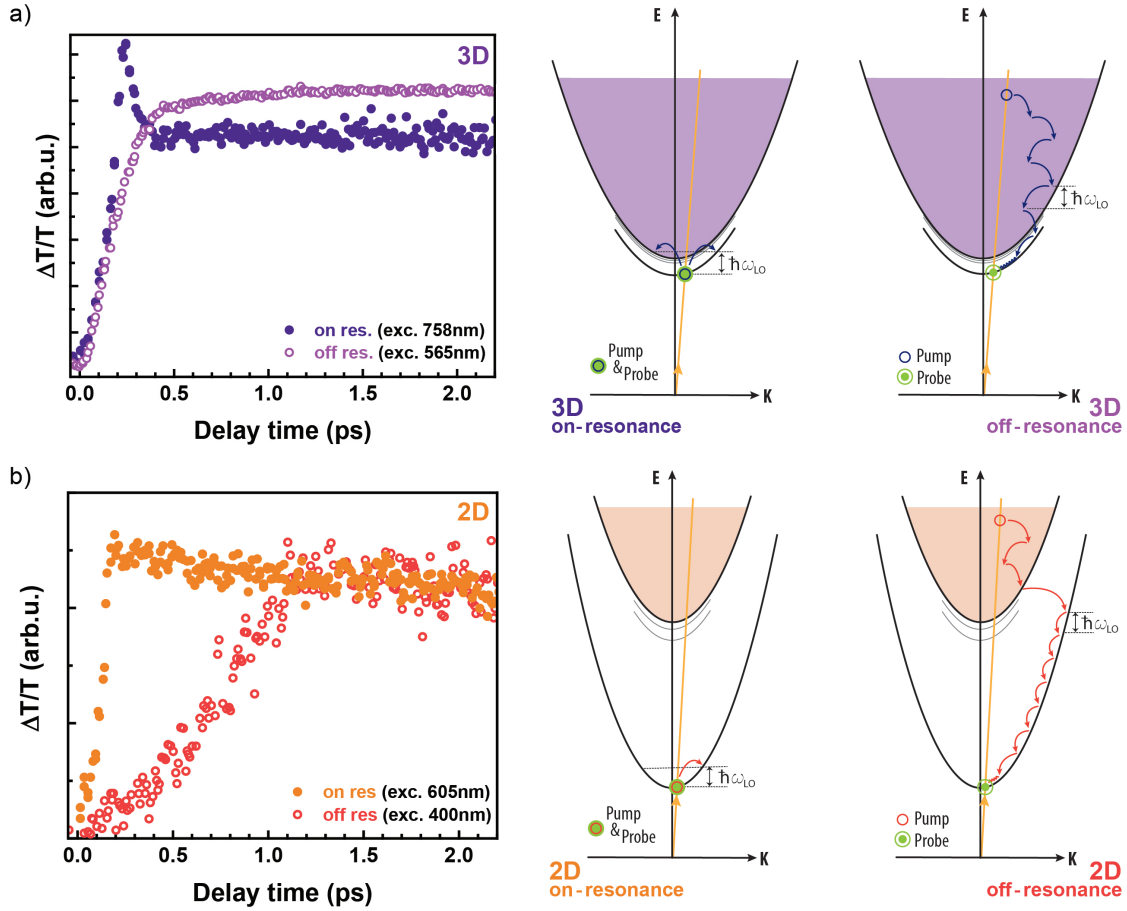


Figure 6.10: Relaxation process of bulk-like NPIs and trilayers pumped on and off resonant. a) Kinetics of on resonant and off resonant pumped bulk-like MAPI NPIs. In the resonant case, the rapid increase of the differential transmission and subsequently recovery of the signal can be attributed to the dissociation of excitons. The off resonant case shows a gradual increase of $\Delta T/T$. b) The corresponding measurement on MAPI trilayers for the resonant case exhibits a different behavior. After an immediate increase, the differential transmission decreases only slowly. Qualitatively, the off resonant spectra of both materials are comparable.

the bulk-like NPI dispersion off resonance, a relatively steep increase differential transmission is detected at the position of the excitonic 1s state. This progression is observed for delay times up to approximately 400 fs. At 400 fs already 92% of the maximal $\Delta T/T$ signal is reached. For longer delay times up to 1.8 ps only a gradual growth is observed. Subsequently the signal decreases and 120 ps after the pump excitation the 1/e of the maximum value is recorded. If the sample is resonantly excited the rise is much more rapidly. The maximum of $\Delta T/T$ is already reached within 230 fs. In turn, the signal drops slightly within 500 fs to 70% of the maximum. The further progression is qualitatively comparable

to the case of non-resonant excitation and the $1/e$ value is reached approximately 115 ps after the excitation. In order to enable a direct comparison of both measurements the relative intensities are adjusted.

The corresponding measurements were also conducted for a dispersion of MAPI trilayers and are depicted in figure 6.10 b). The position of the energy band gap and excitonic 1s state is located at 2.27 eV and 2.04 eV (compare section 5.1.2). Analogously to the previous case a wavelength of 605 nm for resonant excitation and a wavelength of 400 nm for non-resonant excitation were chosen. Again, initially the non-resonant excitation is analyzed. After an initial increase of $\Delta T/T$ within the first picosecond and subsequent decrease is observed. At a delay time of 180 ps only 10 % of the maximal signal is detected. The signal decreases further and at roughly 1 ns nearly any signal was measurable. If the sample is excited resonantly the initial increase is much steeper and after only 200 ps the maximum is reached. The further curve progression does hardly show any deviations in comparison to the non-resonant excitation measurement.

In order to explain the observed kinetics illustrated in figure 6.10 it is useful to consider the dispersion relations. If the NPLs are excited with a wavelength in resonance to the excitonic 1s state cold excitons are directly created. This is evident in the immediate steep increase of the differential transmission, equivalent to the bleaching of the excitonic absorption. In the case of the bulk-like NPLs, these excitons can get dissociated by phonon scattering, since the exciton binding energy of 18.7 meV is smaller than the energy of the thermal phonons ($k_B T \approx 25$ meV at room temperature). In the kinetics, this process is observed in the quick drop of the differential transmission within 270 fs. A similar behavior has been studied on GaAs/AlGaAs QWs [195]. In turn, in the 2D case the exciton binding energy is 230 meV and therefore much bigger than the energy of the phonons. Consequently, no dissociation of the resonantly excited excitons and corresponding drop of the $\Delta T/T$ signal is observed. In the off resonance measurement mainly free carriers are created. As discussed in section 6.1.4, these photoexcited charge carriers with a substantial excess energy relax to the edges of the bands by mainly emitting LO-phonons. The lower energy states are filled up not immediately, but are gradually fed by hot carriers. This process runs within a certain time, resulting in a steady increase of the differential transmission.

Additionally, the maximum of the $\Delta T/T$ signal for off resonant excitation is observed in bulk-like NPLs 500 fs earlier than in trilayers. This observation might be on the first glance contradictory to the cooling times determined in the previous section, but can be explained by reference to the scheme in figure 6.10. In the previous chapter the continuum is analyzed, not the excitonic 1s state. As already discussed, the cooling time of charge

carriers in the 2D NPLs is shorter than for 3D NPLs. However, in the case of MAPI trilayers the emission of many LO-phonons (number > 10) is necessary to reach the energetic minimum of the 1s level of the exciton. Whereas in bulk-like NPLs only a few phonons are sufficient to overcome this energetic barrier. This results in total in the longer lasting initial increase of the measured differential transmission, although a very short cooling time of only a few picoseconds has been observed.

In conclusion, the relaxation and recombination processes in 2D and 3D MAPI NPLs exhibit differences which can be explained by their dimensionality and resulting quantum size effects. Due to an enhanced exciton binding energy of up to 300 meV, exciton dynamics are observed in 2D NPLs, whereas in 3D NPLs mainly free carrier exist.

6.2 Thickness-dependent time-resolved photoluminescence measurements

Time-resolved PL measurements have been performed on MAPI NPLs of different thicknesses using a streak camera. The determined characteristic PL lifetime depends on properties of the analyzed material, like the dimension, the quality of the material and existing interfaces. In time-resolved PL measurements the spectral and temporal evolution of the emission of perovskite NPLs is recorded after previous excitation with a short laser pulse. As described before, a laser pulse excites electron-hole pairs in the perovskites, which subsequently relax, occupying lower energy states and ultimately recombine. If the recombination is radiative, photons are emitted, which can be detected in a streak camera and provide a way to measure transition energies of the analyzed perovskite NPLs and the corresponding lifetimes.

In section 4.2, a successful separation of NPLs according to their thicknesses was demonstrated. The obtained dispersions of purely MAPI mono-, bi- and trilayers enable the study of PL lifetimes for those samples and a comparison to values from bulk-like NPLs. In figure 6.11 streak camera images of the analyzed dispersions are shown. The spectra are obtained by integrating the counts in the time interval from 3.76 to 7.68 ps and are illustrated in grey. The images for the mono-, bi- and trilayers depict a single emission peak, as already observed in the steady-state PL measurements (compare to figure 5.4 in section 5.2). The peaks of maximal emission, detected in the streak camera, are roughly located at 530 nm, 562 nm, 610 nm and 765 nm for $n = 1, 2, 3$ or ∞ , respectively. This values fit to the peak positions determined in steady-state PL measurements of MAPI mono-, bi-, trilayers and bulk-like NPLs. In the case of a bulk-like sample, not only emission at one position is monitored, but also smaller contributions at shorter wavelengths are noted. Those can be attributed to thinner NPLs, showing quantum confinement. The additional peak at 400 nm is a residual signal from the excitation laser and can be ignored.

Figure 6.12a) depicts the PL decays of the different samples. In order to enable a direct comparison of decay times, the time after which the intensity drops to a value of $1/e$ is read out. For the bulk-like sample 26 ns are recorded. Tri-, bi- and monolayers yield PL decay times of 12 ns, 9 ns and 5 ns, respectively. The thinner the platelets are, the shorter the corresponding decay time. Moreover, the decay of the thin, quantum-confined NPLs can be fitted monoexponential, whereas, the function used to model the decay of the bulk-like sample only takes into account the bimolecular recombination of the free carriers. In case of excitons a monomolecular recombination process and in case of free carriers a bimolecular one is expected (compare section 2.3.2). Since the y-axis is plotted in the logarithmic scale

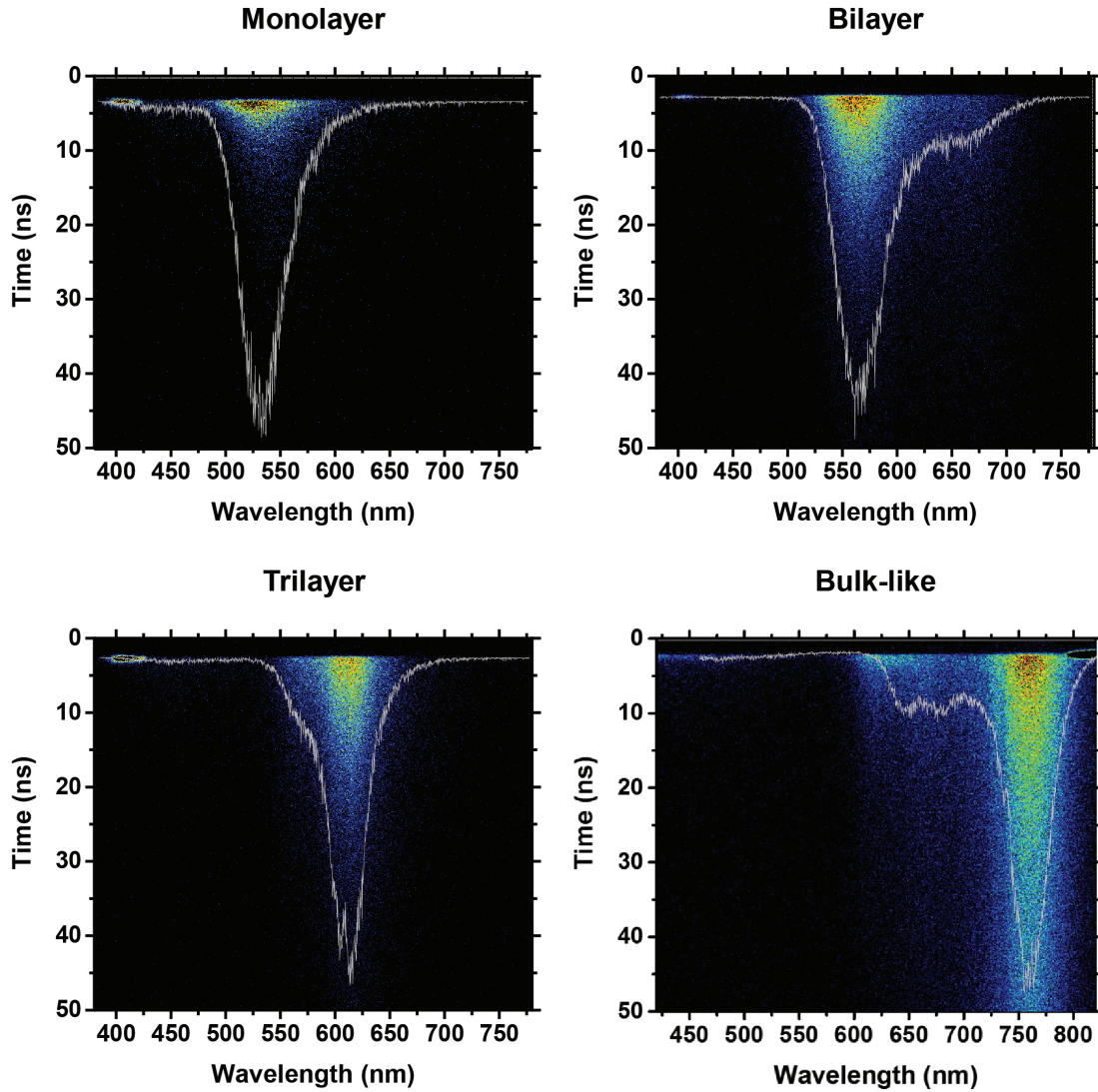


Figure 6.11: Streak camera images of MAPI NPs with different thicknesses. The mono-, bi-, and trilayer dispersions exhibit a single peak in agreement to the steady-state measurements. In the measurement of the bulk-like sample, more channels are recorded which can be attributed to thinner MAPI NPs showing quantum confinement. In grey the spectrum of each sample obtained by integrating the counts in the time interval from 3.76 ps to 7.68 ps are shown.

it is easy to monitor a monoexponential trend for the quantum-confined platelets. In order to show the bimolecular character of the PL decay of the bulk-like sample, the equation (6.2) presented in section 6.1.3 is applied. The resulting curve is depicted in figure 6.12b) as a light purple dashed line and fits nicely to the recorded PL decay. In accordance to the analyzed recombination mechanism of MAPI NPs via TAS presented in section 6.1.3, the obtained monoexponential decay once again testify that in the quantum-confined NPs preliminary the recombination of excitons is observed. In turn, the bimolecular nature of

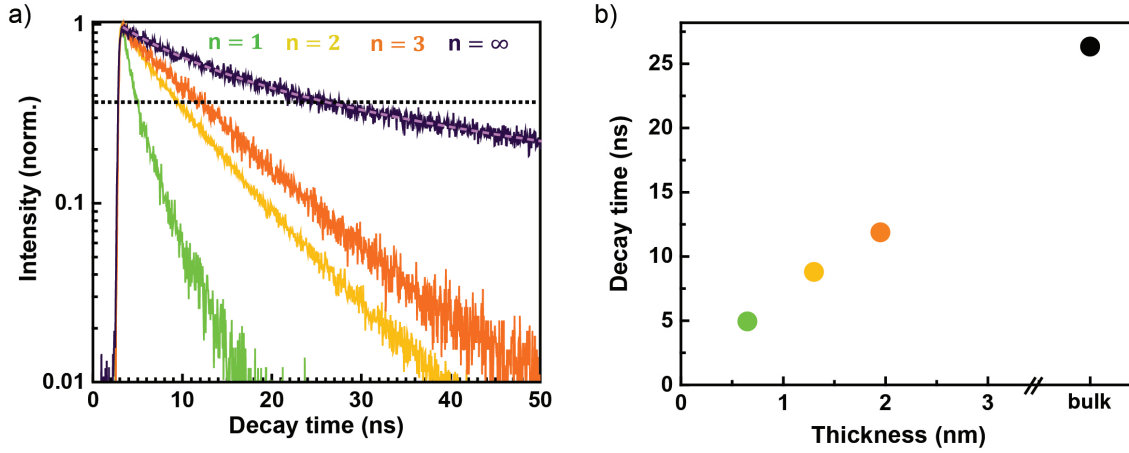


Figure 6.12: PL lifetime of mono-, bi-, trilayers and bulk-like NPLs. a) The PL lifetime is normalized and in order to enable a direct comparison of the decay times the dotted line marks the intensity of $1/e$ of the initial value. In general, a decrease of PL lifetime with reducing number of layers is recorded. Furthermore for the $n = 1, 2, 3$ samples, a monoexponential decay is observed. b) NPLs thickness versus measured decay time. A clear correlation is observed. A thickness of roughly 0.7 nm per layer is assumed.

the recombination kinetics observed for the bulk-like sample confirm the dominant role of free charge carriers in 3D NPLs.

The PL decay occurs via both radiative and nonradiative recombination processes of electron-hole pairs with corresponding decay times τ_r and τ_{nr} . The total decay time (τ_{PL}) is thus given by:

$$\frac{1}{\tau_{PL}} = \frac{1}{\tau_{nr}} + \frac{1}{\tau_r}. \quad (6.6)$$

As already mentioned, the QY also depends on τ_r and τ_{nr} , therefore, by combining equation 6.6 and

$$QY = \frac{\tau_{nr}}{\tau_{nr} + \tau_r}, \quad (6.7)$$

one can evaluate the radiative and nonradiative decay rate, given by:

$$k_r = \frac{1}{\tau_r} \quad \text{and} \quad k_{nr} = \frac{1}{\tau_{nr}}. \quad (6.8)$$

By combining these equations, one obtain

$$k_r = \frac{1}{\tau_{PL}} \cdot QY, \quad (6.9)$$

$$k_{nr} = \frac{1}{\tau_{PL}} (1 - QY). \quad (6.10)$$

Therefore, by measuring the total decay time via for example a streak camera and the QY the radiative and nonradiative decay rate can be determined. QY measurements on a comparable set of samples exhibit a decreasing QY with decreasing thickness of the NPLs [196], consequently k_r and k_{nr} increase with decreasing thickness.

In figure 6.12b) the PL decay times are plotted versus the thickness of the NPLs. As already mentioned a clear trend is noted. With reducing the thickness of the platelets a decrease of the PL decay time is observed. A thickness of 0.7 nm per layer is considered, like observed in the HRTEM measurements presented in section 4.1. A similar trend was observed for epitaxially grown GaAs/AlGaAs quantum wells. In this structure, the radiative decay rate reduces with decreasing well width [197]. A dependence of the radiative decay time (τ^{2D}) on the respective exciton binding energy (E_B) was devised in this work and is given by:

$$\frac{1}{\tau^{2D}} \propto E_B. \quad (6.11)$$

The equation yields a direct dependence of the decay time on the exciton binding energy, but not on the platelet thickness. However, the exciton binding energy is linked to the thickness, thus, one can see a correlation of thickness and decay time in figure 6.12b). Other factors may affect the radiative decay rate as well and the impact of homogeneous or inhomogeneous broadening is discussed in different publications, leading to contradictory conclusions [198, 199]. In order to additionally confirm the validity of equation (6.11) and to address the reasons of the varied decay rate for mono-, bi- and trilayers, further studies, especially on single platelets, would be necessary.

Conclusion and outlook

Within this work, highly stable colloidal lead halide perovskite nanoplatelets of individual thicknesses were fabricated and optically characterized. The synthesis was performed using a top-down synthesis approach, namely ligand-assisted exfoliation, which was developed as part of this work. In order to understand the quantum confinement effects in these nanocrystals, the impact of the dimensionality on the optical properties was studied in more detail. Diverse measurement techniques for optical and structural characterizations supported the analysis and revealed the dominant role of free carriers in bulk-like perovskite NPs and excitons in quantum-confined NPs, respectively. The relaxation and recombination dynamics of photogenerated electron-hole pairs in general, and excitons in particular were closely investigated by performing time-resolved spectroscopy measurements.

In the theoretical part of this work, lead halide perovskites are characterized and compared to well-known semiconductors, like GaAs, using established models and concepts in semiconductor physics. The electronic band structure of lead halide perovskites associated with the absorption is described. Additionally, for a plausible interpretation of the results, ultrafast phenomena and quantum confinement effects are presented in more detail. Most of the cited literature on lead halide perovskites was published during the work on this thesis.

This thesis is about the thickness, and therefore dimensionality dependence of the optical properties of lead halide perovskite nanoplatelets. The developed synthesis based on ligand-assisted exfoliation enables the preparation of nanoplatelets with controlled halide composition and thickness. Based on this method the fabrication of mono-, bi-, and trilayer dispersions of lead halide perovskites succeeded and allows a study of the confinement-induced changes. As the thickness of the MAPI NPs is reduced to only a few layers a significant blue-shift of the PL emission from 1.62 eV to 2.34 eV is noted, indicating strong quantum confinement effects. Furthermore, the linear absorption is calculated based on

the Elliott formula for 2D and 3D semiconductors. A comparison of these calculations and the actual measurements enables the determination of the band gap and the exciton binding energy in dependence of the platelet thickness. The exciton binding energy of bulk-like MAPI NPLs is approximately 18.7 meV and more than a factor of 10 smaller than the one of the strongly confined NPLs.

In the last chapter of this thesis the carrier dynamics in 2D and 3D MAPI nanoplatelets are analyzed. The observed dependence of the state filling on the charge carrier density and the bimolecular recombination in 3D NPLs demonstrate the prevailing role of free charge carriers. In contrary, the same experiments carried out for 2D NPLs show that excitons are dominant. Comparing the cooling curves of 2D and 3D MAPI NPLs reveals a shorter cooling time for the 2D case than the 3D one, which stands in contrast to reports on other semiconductor nanostructures. The deviation in cooling times can be explained by considering the dielectric environment of the perovskite nanoplatelets. The small dielectric constant of the surrounding ligands lead to a reduced Coulomb screening in the 2D NPLs compared to 3D and consequently to a lower scattering rate. Furthermore, hardly any correlation between the cooling time and the charge carrier density was observed in the quantum-confined NPLs unlike to the bulk-like NPLs. In the charge carrier-dependent cooling curves of the bulk-like NPLs the cooling process is prolonged due to the hot phonon effect. In 2D the surface-to-volume ratio is bigger and therefore the LO-phonons dissipate more efficiently to the cooler surrounding before they can be reabsorbed. Consequently, no hot phonon effect was observed. Moreover, from the analysis of the exciton formation dynamics a thickness dependency was discovered. Resonantly excited excitons in bulk-like NPLs quickly dissociate by interactions with thermal phonons. Whereas in 2D the exciton binding energy is much bigger than the phonon energy, hence, a dissociation of the excitons was not observed. Beside transient absorption measurements, time-resolved PL measurements were performed. The recorded photoluminescence lifetime decreases with reducing thickness of the NPLs accompanied by an increasing exciton binding energy. Again, a bimolecular recombination for bulk-like NPLs and a monomolecular recombination for quantum confined NPLs was observed.

In summary, this thesis contains a fundamental study of perovskite NPLs with special interest on the interaction of charge carriers with photons and phonons and their dynamics, which determine their optical properties. The observed thickness-dependence of the optical properties can give a new impetus to improve the efficiency of devices based on lead halide perovskites such as LEDs, lasers and solar cells. A possible approach is to implement NPLs with identical halide compositions but different thicknesses. In such a complex device one could achieve an enhanced efficiency through cascaded energy transfer processes. Further-

more, nanostructures offer a perfect platform to encounter stability issues and prevent the common obstacle of halide migration. By encapsulating the nanoparticles in a polymer shell, improvements regarding both aspects can be accomplished. First promising results have been achieved in the course of this PhD thesis and a publication regarding these findings is in preparation as listed in *Publications and contributions to conferences*.

This thesis concentrates on a more fundamental perspective to support the general understanding and might therefore contribute to further work on hybrid perovskites. It is not yet to be known if perovskite based devices may become part of our daily life. Right now there are many signs suggesting their presence for a bright future.

Bibliography

- [1] H. L. Bowman. On the Structure of Perovskite from the Burgumer Alp. *Mineralogical Magazine*, (15):156–176, 1908.
- [2] S. Miyake and R. Ueda. On Polymorphic Change of BaTiO₃. *Journal of the Physical Society of Japan*, 1(1):32–33, 1946.
- [3] L. E. Cross and R. E. Newnham. History of Ferroelectrics. *Ceramics and Civilization*, (III):289–305, 1987.
- [4] D. Weber. CH₃NH₃PbX₃ ein Pb(ii)-System mit kubischer Perowskitstruktur. *Zeitschrift für Naturforschung*, (33 b):1443–1445, 1978.
- [5] D. Weber. CH₃NH₃SnBr_xI_{3-x} (x=0-3), ein Sn(II)-System mit kubischer Perowskitstruktur. *Zeitschrift für Naturforschung*, (33b):862–865, 1978.
- [6] D. B. Mitzi, C. A. Feild, W. T. A. Harrison, and A. M. Guloy. Conducting tin halides with a layered organic-based perovskite structure. *Nature*, 369(6480):467–469, 1994.
- [7] D. B. Mitzi, C. D. Dimitrakopoulos, and L. L. Kosbar. Structurally tailored organic–inorganic perovskites: Optical properties and solution-processed channel materials for thin-film transistors. *Chemistry of Materials*, 13(10):3728–3740, 2001.
- [8] A. Kojima, K. Teshima, Y. Shirai, and T. Miyasaka. Organometal halide perovskites as visible-light sensitizers for photovoltaic cells. *Journal of the American Chemical Society*, 131(17):6050–6051, 2009.
- [9] W. S. Yang, B. Park, E. H. Jung, N. J. Jeon, Y. C. Kim, D. U. Lee, S. S. Shin, J. Seo, E. K. Kim, J. H. Noh, and S. I. Seok. Iodide management in formamidinium-lead-halide-based perovskite layers for efficient solar cells. *Science*, 356(6345):1376–1379, 2017.

- [10] D. P. McMeekin, G. Sadoughi, Wa. Rehman, G. E. Eperon, M. Saliba, M. T. Horantner, A. Haghighirad, N. Sakai, L. Korte, B. Rech, M. B. Johnston, L. M. Herz, and H. J. Snaith. A mixed-cation lead mixed-halide perovskite absorber for tandem solar cells. *Science*, 351(6269):151–155, 2016.
- [11] D. A. Jenny, J. J. Loferski, and P. Rappaport. Photovoltaic effect in GaAs p-n junctions and solar energy conversions. *Physical Review B*, (101):1208–1209, 1956.
- [12] I. B. Koutselas, L. Ducasse, and G. C. Papavassiliou. Electronic properties of three- and low-dimensional semiconducting materials with Pb halide and Sn halide units. *Journal of Physics: Condensed Matter*, 8(9):1217–1227, 1996.
- [13] T. Ishihara, J. Takahashi, and T. Goto. Optical properties due to electronic transitions in two-dimensional semiconductors $(C_nH_{2n+1}NH_3)_2PbI_4$. *Physical Review B*, 42(17):11099–11107, 1990.
- [14] D. B. Mitzi, S. Wang, C. A. Feild, C. A. Chess, and A. M. Guloy. Conducting layered organic-inorganic halides containing $\langle 110 \rangle$ -oriented perovskite sheets. *Science*, 267(5203):1473–1476, 1995.
- [15] L. C. Schmidt, A. Pertegas, S. Gonzalez-Carrero, O. Malinkiewicz, S. Agouram, G. Minguez Espallargas, H. J. Bolink, R. E. Galian, and J. Perez-Prieto. Nontemplate synthesis of $CH_3NH_3PbBr_3$ perovskite nanoparticles. *Journal of the American Chemical Society*, 136(3):850–853, 2014.
- [16] G. Nedelcu, L. Protesescu, S. Yakunin, M. I. Bodnarchuk, M. J. Grotevent, and M. V. Kovalenko. Fast anion-exchange in highly luminescent nanocrystals of cesium lead halide perovskites ($CsPbX_3$, $X = Cl, Br, I$). *Nano Letters*, 15(8):5635–5640, 2015.
- [17] O. Vybornyi, S. Yakunin, and M. V. Kovalenko. Polar-solvent-free colloidal synthesis of highly luminescent alkylammonium lead halide perovskite nanocrystals. *Nanoscale*, 8(12):6278–6283, 2016.
- [18] I. Lignos, S. Stavarakis, G. Nedelcu, L. Protesescu, A. J. deMello, and M. V. Kovalenko. Synthesis of cesium lead halide perovskite nanocrystals in a droplet-based microfluidic platform: Fast parametric space mapping. *Nano Letters*, 16(3):1869–1877, 2016.
- [19] J. Li, S. G. R. Bade, X. Shan, and Z. Yu. Single-layer light-emitting diodes using organometal halide perovskite/poly(ethylene oxide) composite thin films. *Advanced Materials*, 27(35):5196–5202, 2015.

- [20] K. Domanski, W. Tress, T. Moehl, M. Saliba, M. Khaja Nazeeruddin, and M. Grätzel. Working principles of perovskite photodetectors: Analyzing the interplay between photoconductivity and voltage-driven energy-level alignment. *Advanced Functional Materials*, 25(44):6936–6947, 2015.
- [21] F. Deschler, M. Price, S. Pathak, L. E. Klintberg, D.-D. Jarausch, R. Higler, S. Hüttnner, T. Leijtens, S. D. Stranks, H. J. Snaith, M. Atature, R. T. Phillips, and R. H. Friend. High photoluminescence efficiency and optically pumped lasing in solution-processed mixed halide perovskite semiconductors. *The Journal of Physical Chemistry Letters*, 5(8):1421–1426, 2014.
- [22] H. Zhu, Y. Fu, F. Meng, X. Wu, Z. Gong, Q. Ding, M. V. Gustafsson, M. T. Trinh, S. Jin, and X.-Y. Zhu. Lead halide perovskite nanowire lasers with low lasing thresholds and high quality factors. *Nature Materials*, 14(6):636–642, 2015.
- [23] X. Y. Chin, D. Cortecchia, J. Yin, A. Bruno, and C. Soci. Lead iodide perovskite light-emitting field-effect transistor. *Nature Communications*, 6:7383, 2015.
- [24] S. D. Stranks, V. M. Burlakov, T. Leijtens, J. M. Ball, A. Goriely, and H. J. Snaith. Recombination kinetics in organic-inorganic perovskites: Excitons, free charge, and subgap states. *Physical Review Applied*, 2(3), 2014.
- [25] D. Shi, V. Adinolfi, R. Comin, M. Yuan, E. Alarousu, A. Buin, Y. Chen, S. Hoogland, A. Rothenberger, K. Katsiev, Y. Losovyj, X. Zhang, P. A. Dowben, O. F. Mohammed, E. H. Sargent, and O. M. Bakr. Low trap-state density and long carrier diffusion in organolead trihalide perovskite single crystals. *Science*, 347(6221):519–522, 2015.
- [26] D. W. de Quilettes, S. M. Vorpahl, S. D. Stranks, H. Nagaoka, G. E. Eperon, M. E. Ziffer, H. J. Snaith, and D. S. Ginger. Impact of microstructure on local carrier lifetime in perovskite solar cells. *Science*, 348(6235):683–686, 2015.
- [27] M. M. Lee, J. Teuscher, T. Miyasaka, T. N. Murakami, and H. J. Snaith. Efficient hybrid solar cells based on meso-superstructured organometal halide perovskites. *Science (New York, N.Y.)*, 338(6107):643–647, 2012.
- [28] A. Sadhanala, S. Ahmad, B. Zhao, N. Giesbrecht, P. M. Pearce, F. Deschler, R. L. Z. Hoye, K. C. Gödel, T. Bein, P. Docampo, S. E. Dutton, M. F. L. de Volder, and R. H. Friend. Blue-green color tunable solution processable organolead chloride-bromide mixed halide perovskites for optoelectronic applications. *Nano Letters*, 15(9):6095–6101, 2015.

- [29] F. Stasio, S. Christodoulou, N. Huo, and G. Konstantatos. Near-unity photoluminescence quantum yield in CsPbBr₃ nanocrystal solid-state films via postsynthesis treatment with lead bromide. *Chemistry of Materials*, 29(18):7663–7667, 2017.
- [30] Z. Wang, Q. Lin, F. P. Chmiel, N. Sakai, L. M. Herz, and H. J. Snaith. Efficient ambient-air-stable solar cells with 2d–3d heterostructured butylammonium-caesium-formamidinium lead halide perovskites. *Nature Energy*, 2(9):17135, 2017.
- [31] S. P. Senanayak, B. Yang, T. H. Thomas, N. Giesbrecht, W. Huang, E. Gann, B. Nair, K. Goedel, S. Guha, X. Moya, C. R. McNeill, P. Docampo, A. Sadhanala, R. H. Friend, and H. Sirringhaus. Understanding charge transport in lead iodide perovskite thin-film field-effect transistors. *Science Advances*, 3(1):e1601935, 2017.
- [32] L. N. Quan, M. Yuan, R. Comin, O. Voznyy, E. M. Beauregard, S. Hoogland, A. Buin, A. R. Kirmani, K. Zhao, A. Amassian, D. H. Kim, and E. H. Sargent. Ligand-stabilized reduced-dimensionality perovskites. *Journal of the American Chemical Society*, 138(8):2649–2655, 2016.
- [33] D. H. Cao, C. C. Stoumpos, O. K. Farha, J. T. Hupp, and M. G. Kanatzidis. 2d homologous perovskites as light-absorbing materials for solar cell applications. *Journal of the American Chemical Society*, 137(24):7843–7850, 2015.
- [34] H. Tsai, W. Nie, J.-C. Blancon, C. C. Stoumpos, R. Asadpour, B. Harutyunyan, A. J. Neukirch, R. Verduzco, J. J. Crochet, S. Tretiak, L. Pedesseau, J. Even, M. A. Alam, G. Gupta, J. Lou, P. M. Ajayan, M. J. Bedzyk, and M. G. Kanatzidis. High-efficiency two-dimensional Ruddlesden-Popper perovskite solar cells. *Nature*, 536(7616):312–316, 2016.
- [35] G. E. Eperon, S. D. Stranks, C. Menelaou, M. B. Johnston, L. M. Herz, and H. J. Snaith. Formamidinium lead trihalide: A broadly tunable perovskite for efficient planar heterojunction solar cells. *Energy & Environmental Science*, 7(3):982, 2014.
- [36] F. Zhang, H. Zhong, C. Chen, X. Wu, X. Hu, H. Huang, J. Han, B. o Zou, and Y. Dong. Brightly luminescent and color-tunable colloidal CH₃NH₃PbX₃ (X = Br, I, Cl) quantum dots: Potential alternatives for display technology. *ACS Nano*, 9(4):4533–4542, 2015.
- [37] J. A. Sichert, Y. Tong, N. Mutz, M. Vollmer, S. Fischer, K. Z. Milowska, R. Garcia Cortadella, B. Nickel, C. Cardenas-Daw, J. K. Stolarczyk, A. S. Urban, and J. Feldmann. Quantum size effect in organometal halide perovskite nanoplatelets. *Nano Letters*, 15(10):6521–6527, 2015.

- [38] N.-G. Park. Perovskite solar cells: An emerging photovoltaic technology. *Materials Today*, 18(2):65–72, 2015.
- [39] K. D. Karlin. *Progress in Inorganic Chemistry*. Progress in Inorganic Chemistry. John Wiley & Sons, Inc, Hoboken, NJ, USA, 1999.
- [40] G. Rose. *De perowskite, fossili novo. In de novis quibusdam fossilibus quae in montibus uraliis inveniuntur*. AG Schade, Berlin, 1839.
- [41] V. M. Goldschmidt. Die Gesetze der Krystallochemie. *Die Naturwissenschaften*, 14(21):477–485, 1926.
- [42] C. C. Stoumpos and M. G. Kanatzidis. The renaissance of halide perovskites and their evolution as emerging semiconductors. *Accounts of Chemical Research*, 48(10):2791–2802, 2015.
- [43] B. Saparov and D. B. Mitzi. Organic-inorganic perovskites: Structural versatility for functional materials design. *Chemical Reviews*, 116(7):4558–4596, 2016.
- [44] W. Li, Z. Wang, F. Deschler, S. Gao, R. H. Friend, and A. K. Cheetham. Chemically diverse and multifunctional hybrid organic–inorganic perovskites. *Nature Reviews Materials*, 2(3):16099, 2017.
- [45] S. F. Hoeffler, G. Trimmel, and T. Rath. Progress on lead-free metal halide perovskites for photovoltaic applications: A review. *Monatshefte für Chemie*, 148(5):795–826, 2017.
- [46] M. A. Peña and J. L. G. Fierro. Chemical structures and performance of perovskite oxides. *Chemical Reviews*, 101(7):1981–2018, 2001.
- [47] I. M. Reaney, E. L. Colla, and N. Setter. Dielectric and structural characteristics of Ba- and Sr-based complex perovskites as a function of tolerance factor. *Japanese Journal of Applied Physics*, 33(7R):3984, 1994.
- [48] F. Brivio, J. M. Frost, J. M. Skelton, A. J. Jackson, O. J. Weber, M. T. Weller, A. R. Goñi, A. M. A. Leguy, P. R. F. Barnes, and A. Walsh. Lattice dynamics and vibrational spectra of the orthorhombic, tetragonal, and cubic phases of methylammonium lead iodide. *Physical Review B*, 92(14), 2015.
- [49] A. Poglitsch and D. Weber. Dynamic disorder in methylammoniumtrihalogenoplumbates (II) observed by millimeter-wave spectroscopy. *The Journal of Chemical Physics*, 87(11):6373–6378, 1987.

- [50] M. Shirayama, H. Kadowaki, T. Miyadera, T. Sugita, M. Tamakoshi, M. Kato, T. Fujiseki, D. Murata, S. Hara, T. N. Murakami, S. Fujimoto, M. Chikamatsu, and H. Fujiwara. Optical transitions in hybrid perovskite solar cells: Ellipsometry, density functional theory, and quantum efficiency analyses for $\text{CH}_3\text{NH}_3\text{PbI}_3$. *Physical Review Applied*, 5(1), 2016.
- [51] Y. Wang, T. Gould, J. F. Dobson, H. Zhang, H. Yang, X. Yao, and H. Zhao. Density functional theory analysis of structural and electronic properties of orthorhombic perovskite $\text{CH}_3\text{NH}_3\text{PbI}_3$. *Physical Chemistry Chemical Physics : PCCP*, 16(4):1424–1429, 2014.
- [52] G. Giorgi, J.-I. Fujisawa, H. Segawa, and K. Yamashita. Small photocarrier effective masses featuring ambipolar transport in methylammonium lead iodide perovskite: A density functional analysis. *The Journal of Physical Chemistry Letters*, 4(24):4213–4216, 2013.
- [53] J. Even, L. Pedesseau, M.-A. Dupertuis, J.-M. Jancu, and C. Katan. Electronic model for self-assembled hybrid organic/perovskite semiconductors: Reverse band edge electronic states ordering and spin-orbit coupling. *Physical Review B*, 86(20), 2012.
- [54] P. Umari, E. Mosconi, and F. de Angelis. Relativistic GW calculations on $\text{CH}_3\text{NH}_3\text{PbI}_3$ and $\text{CH}_3\text{NH}_3\text{SnI}_3$ perovskites for solar cell applications. *Scientific Reports*, 4:4467, 2014.
- [55] F. Brivio, K. T. Butler, A. Walsh, and M. van Schilfgaarde. Relativistic quasiparticle self-consistent electronic structure of hybrid halide perovskite photovoltaic absorbers. *Physical Review B*, 89(15), 2014.
- [56] J. Even, L. Pedesseau, C. Katan, M. Kepenekian, J.-S. Lauret, D. Saponi, and E. Deleporte. Solid-state physics perspective on hybrid perovskite semiconductors. *The Journal of Physical Chemistry C*, 119(19):10161–10177, 2015.
- [57] J. S. Manser, J. A. Christians, and P. V. Kamat. Intriguing optoelectronic properties of metal halide perovskites. *Chemical Reviews*, 116(21):12956–13008, 2016.
- [58] E. Menéndez-Proupin, P. Palacios, P. Wahnón, and J. C. Conesa. Self-consistent relativistic band structure of the $\text{CH}_3\text{NH}_3\text{PbI}_3$ perovskite. *Physical Review B*, 90(4), 2014.

- [59] W.-J. Yin, J.-H. Yang, J. Kang, Y. Yan, and S.-H. Wei. Halide perovskite materials for solar cells: A theoretical review. *Journal of Materials Chemistry A*, 3(17):8926–8942, 2015.
- [60] T. Umebayashi, K. Asai, T. Kondo, and A. Nakao. Electronic structures of lead iodide based low-dimensional crystals. *Physical Review B*, 67(15), 2003.
- [61] D. J. Griffiths. *Introduction to quantum mechanics*. Prentice Hall, Englewood Cliffs, N.J., 1995.
- [62] J. Even, L. Pedesseau, J.-M. Jancu, and C. Katan. Importance of spin-orbit coupling in hybrid organic/inorganic perovskites for photovoltaic applications. *The Journal of Physical Chemistry Letters*, 4(17):2999–3005, 2013.
- [63] A. Amat, E. Mosconi, E. Ronca, C. Quarti, P. Umari, M. K. Nazeeruddin, M. Grätzel, and F. de Angelis. Cation-induced band-gap tuning in organohalide perovskites: interplay of spin-orbit coupling and octahedra tilting. *Nano Letters*, 14(6):3608–3616, 2014.
- [64] G. Bihlmayer, O. Rader, and R. Winkler. Focus on the rashba effect. *New Journal of Physics*, 17(5):050202, 2015.
- [65] D. Niesner, M. Hauck, S. Shrestha, I. Levchuk, G. J. Matt, A. Osvet, M. Batentschuk, C. Brabec, H. B. Weber, and T. Fauster. Spin-split bands cause the indirect band gap of $(\text{CH}_3\text{NH}_3)\text{PbI}_3$: Experimental evidence from circular photogalvanic effect. *Journal of Physics: Condensed Matter*, (arXiv:1703.08740v1), 2017.
- [66] F. Zheng, L. Z. Tan, S. Liu, and A. M. Rappe. Rashba spin-orbit coupling enhanced carrier lifetime in $\text{CH}_3\text{NH}_3\text{PbI}_3$. *Nano letters*, 15(12):7794–7800, 2015.
- [67] D. Giovanni, H. Ma, J. Chua, M. Grätzel, R. Ramesh, S. Mhaisalkar, N. Mathews, and T. C. Sum. Highly spin-polarized carrier dynamics and ultralarge photoinduced magnetization in $\text{CH}_3\text{NH}_3\text{PbI}_3$ perovskite thin films. *Nano Letters*, 15(3):1553–1558, 2015.
- [68] Y.-C. Hsiao, T. Wu, M. Li, and B. Hu. Magneto-optical studies on spin-dependent charge recombination and dissociation in perovskite solar cells. *Advanced Materials*, 27(18):2899–2906, 2015.
- [69] C. Motta, F. El-Mellouhi, S. Kais, N. Tabet, F. Alharbi, and S. Sanvito. Revealing the role of organic cations in hybrid halide perovskite $\text{CH}_3\text{NH}_3\text{PbI}_3$. *Nature Communications*, 6:7026, 2015.

- [70] E. Mosconi, T. Etienne, and F. de Angelis. Rashba band splitting in organohalide lead perovskites: Bulk and surface effects. *The Journal of Physical Chemistry Letters*, 8(10):2247–2252, 2017.
- [71] P. Y. Yu and M. Cardona. *Fundamentals of Semiconductors*. Springer Berlin Heidelberg, Berlin, Heidelberg, 2010.
- [72] V. A. Hintermayr, A. F. Richter, F. Ehrat, M. Döblinger, W. Vanderlinden, J. A. Sichert, Y. Tong, L. Polavarapu, J. Feldmann, and A. S. Urban. Tuning the optical properties of perovskite nanoplatelets through composition and thickness by ligand-assisted exfoliation. *Advanced Materials*, 28(43):9478–9485, 2016.
- [73] P. A. M. Dirac. The quantum theory of the emission and absorption of radiation. *Proceedings of the Royal Society A: Mathematical, Physical and Engineering Sciences*, 114(767):243–265, 1927.
- [74] E. Fermi, J. Orear, A. H. Rosenfeld, and R. A. Schluter. *Nuclear physics*. Midway Reprints. University of Chicago Press, 1992.
- [75] J. Even, L. Pedesseau, and C. Katan. Analysis of multivalley and multibandgap absorption and enhancement of free carriers related to exciton screening in hybrid perovskites. *The Journal of Physical Chemistry C*, 118(22):11566–11572, 2014.
- [76] J. Even, L. Pedesseau, J.-M. Jancu, and C. Katan. DFT and k-p modelling of the phase transitions of lead and tin halide perovskites for photovoltaic cells. *Physica Status Solidi - Rapid Research Letters*, 8(1):31–35, 2014.
- [77] L. M. Herz. Charge-carrier dynamics in organic-inorganic metal halide perovskites. *Annual Review of Physical Chemistry*, 67:65–89, 2016.
- [78] Y. P. Varshni. Temperature dependence of the energy gap in semiconductors. *Physica*, 34(1):149–154, 1967.
- [79] S.-H. Wei and A. Zunger. Predicted band-gap pressure coefficients of all diamond and zinc-blende semiconductors: Chemical trends. *Physical Review B*, 60(8):5404–5411, 1999.
- [80] J. Bardeen and W. Shockley. Deformation potentials and mobilities in non-polar crystals. *Physical Review*, 80(1):72–80, 1950.
- [81] C. H. Chang, C. H. Park, and K. Matsuishi. First-principles study of the structural and the electronic properties of the lead-halide-based inorganic-organic perovskites

- (CH_3NH_3) PbX_3 and CsPbX_3 ($X = \text{Cl, Br, I}$). *Journal of the Korean Physical Society*, (44):889–893, 2004.
- [82] J. M. Frost, K. T. Butler, F. Brivio, C. H. Hendon, M. van Schilfhaarde, and A. Walsh. Atomistic origins of high-performance in hybrid halide perovskite solar cells. *Nano Letters*, 14(5):2584–2590, 2014.
- [83] J. I. Pankove. *Optical processes in semiconductors*. Dover Publications and Constable, New York and London, 1975.
- [84] T. Dittrich, C. Awino, P. Prajontat, B. Rech, and M. C. Lux-Steiner. Temperature dependence of the band gap of $\text{CH}_3\text{NH}_3\text{PbI}_3$ stabilized with PMMA: A modulated surface photovoltage study. *The Journal of Physical Chemistry C*, 119(42):23968–23972, 2015.
- [85] V. D’Innocenzo, G. Grancini, M. J. P. Alcocer, A. R. S. Kandada, S. D. Stranks, M. M. Lee, G. Lanzani, H. J. Snaith, and A. Petrozza. Excitons versus free charges in organo-lead tri-halide perovskites. *Nature Communications*, 5:3586, 2014.
- [86] R. L. Milot, G. E. Eperon, H. J. Snaith, M. B. Johnston, and L. M. Herz. Temperature-dependent charge-carrier dynamics in $\text{CH}_3\text{NH}_3\text{PbI}_3$ perovskite thin films. *Advanced Functional Materials*, 25(39):6218–6227, 2015.
- [87] I. P. Swainson, R. P. Hammond, C. Soullière, O. Knop, and W. Massa. Phase transitions in the perovskite methylammonium lead bromide, $\text{CH}_3\text{ND}_3\text{PbBr}_3$. *Journal of Solid State Chemistry*, 176(1):97–104, 2003.
- [88] T. Baikie, Y. Fang, J. M. Kadro, M. Schreyer, F. Wei, S. G. Mhaisalkar, M. Graetzel, and T. J. White. Synthesis and crystal chemistry of the hybrid perovskite (CH_3NH_3) PbI_3 for solid-state sensitised solar cell applications. *Journal of Materials Chemistry A*, 1(18):5628, 2013.
- [89] K. Wu, A. Bera, C. Ma, Y. Du, Y. Yang, L. Li, and T. Wu. Temperature-dependent excitonic photoluminescence of hybrid organometal halide perovskite films. *Physical Chemistry Chemical Physics : PCCP*, 16(41):22476–22481, 2014.
- [90] J. Xing, X. F. Liu, Q. Zhang, S. T. Ha, Y. W. Yuan, C. Shen, T. C. Sum, and Q. Xiong. Vapor phase synthesis of organometal halide perovskite nanowires for tunable room-temperature nanolasers. *Nano Letters*, 15(7):4571–4577, 2015.
- [91] M. T. Weller, O. J. Weber, P. F. Henry, A. M. Di Pumpo, and T. C. Hansen. Complete structure and cation orientation in the perovskite photovoltaic methylammo-

- mium lead iodide between 100 and 352 K. *Chemical Communications*, 51(20):4180–4183, 2015.
- [92] P. S. Whitfield, N. Herron, W. E. Guise, K. Page, Y. Q. Cheng, I. Milas, and M. K. Crawford. Structures, phase transitions and tricritical behavior of the hybrid perovskite methyl ammonium lead iodide. *Scientific Reports*, 6:35685, 2016.
- [93] D. M. Trots and S. V. Myagkota. High-temperature structural evolution of caesium and rubidium triiodoplumbates. *Journal of Physics and Chemistry of Solids*, 69(10):2520–2526, 2008.
- [94] G. D. Scholes and G. Rumbles. Excitons in nanoscale systems. *Nature Materials*, 5(9):683–696, 2006.
- [95] C. Kittel. *Einführung in die Festkörperphysik*. Oldenbourg Verlag, München, 15 edition, 2013.
- [96] C. Klingshirn. *Semiconductor optics*. Advanced Texts in Physics. Springer, Berlin, 3rd edition, 2007.
- [97] J. S. Manser and P. V. Kamat. Band filling with free charge carriers in organometal halide perovskites. *Nature Photonics*, 8(9):737–743, 2014.
- [98] M. Saba, M. Cadelano, D. Marongiu, F. Chen, V. Sarritzu, N. Sestu, C. Figus, M. Aresti, R. Piras, A. G. Lehmann, C. Cannas, A. Musinu, F. Quochi, A. Mura, and G. Bongiovanni. Correlated electron-hole plasma in organometal perovskites. *Nature Communications*, 5:5049, 2014.
- [99] T. J. Savenije, C. S. Ponseca, L. Kunneman, M. Abdellah, K. Zheng, Y. Tian, Q. Zhu, S. E. Canton, I. G. Scheblykin, T. Pullerits, A. Yartsev, and V. Sundstrom. Thermally activated exciton dissociation and recombination control the carrier dynamics in organometal halide perovskite. *The Journal of Physical Chemistry Letters*, 5(13):2189–2194, 2014.
- [100] A. M. Askar and K. Shankar. Exciton binding energy in organic–inorganic tri-halide perovskites. *Journal of Nanoscience and Nanotechnology*, 16(6):5890–5901, 2016.
- [101] H. Huang, L. Polavarapu, J. A. Sichert, A. S. Sussha, A. S. Urban, and A. L. Rogach. Colloidal lead halide perovskite nanocrystals: Synthesis, optical properties and applications. *NPG Asia Materials*, 8(11):e328, 2016.

- [102] J. Tilchin, D. N. Dirin, G. I. Maikov, A. Sashchiuk, M. V. Kovalenko, and E. Lifshitz. Hydrogen-like Wannier-Mott excitons in single crystal of methylammonium lead bromide perovskite. *ACS Nano*, 10(6):6363–6371, 2016.
- [103] M. Saba, F. Quochi, A. Mura, and G. Bongiovanni. Excited state properties of hybrid perovskites. *Accounts of Chemical Research*, 49(1):166–173, 2016.
- [104] S. D. Stranks, G. E. Eperon, G. Grancini, C. r Menelaou, M. J. P. Alcocer, T. Leijtens, L. M. Herz, A. Petrozza, and H. J. Snaith. Electron-hole diffusion lengths exceeding 1 micrometer in an organometal trihalide perovskite absorber. *Science*, 342(6156):341–344, 2013.
- [105] C. Wehrenfennig, G. E. Eperon, M. B. Johnston, H. J. Snaith, and L. M. Herz. High charge carrier mobilities and lifetimes in organolead trihalide perovskites. *Advanced Materials*, 26(10):1584–1589, 2014.
- [106] Y. Yamada, T. Nakamura, M. Endo, A. Wakamiya, and Y. Kanemitsu. Photocarrier recombination dynamics in perovskite $\text{CH}_3\text{NH}_3\text{PbI}_3$ for solar cell applications. *Journal of the American Chemical Society*, 136(33):11610–11613, 2014.
- [107] P. Tyagi, S. M. Arveson, and W. A. Tisdale. Colloidal organohalide perovskite nanoplatelets exhibiting quantum confinement. *The Journal of Physical Chemistry Letters*, 6(10):1911–1916, 2015.
- [108] G. Q. Zhang and A. Roosmalen. *More than Moore*. Springer US, Boston, MA, 2009.
- [109] J. H. Davies. *The physics of low-dimensional semiconductors: An introduction*. Cambridge University Press, Cambridge, 2009.
- [110] H. Haug and S. W. Koch. *Quantum theory of the optical and electronic properties of semiconductors*. World Scientific, New Jersey, 4th ed., repr edition, 2005.
- [111] R. J. Elliott. Intensity of optical absorption by excitons. *Physical Review*, 108(6):1384–1389, 1957.
- [112] D. S. Chemla and D. A. B. Miller. Room-temperature excitonic nonlinear-optical effects in semiconductor quantum-well structures. *Journal of the Optical Society of America B*, 2(7):1155, 1985.
- [113] S. Glutsch. *Excitons in low-dimensional semiconductors: Theory, numerical methods, applications*, volume 141 of *Springer series in solid-state sciences*. Springer, Berlin and London, 2011.

- [114] S. Schmitt-Rink, D. S. Chemla, and D. A. B. Miller. Linear and nonlinear optical properties of semiconductor quantum wells. *Advances in Physics*, 38(2):89–188, 1989.
- [115] J. Shah. *Ultrafast spectroscopy of semiconductors and semiconductor nanostructures*, volume 115. Springer Verlag, Berlin and New York, 2 edition, 2010.
- [116] J. Shah. *Hot carriers in semiconductor nanostructures: Physics and applications*. Academic Press, Boston, 1992.
- [117] O. Flender, J. R. Klein, T. Lenzer, and K. Oum. Ultrafast photoinduced dynamics of the organolead trihalide perovskite $\text{CH}_3\text{NH}_3\text{PbI}_3$ on mesoporous TiO_2 scaffolds in the 320–920 nm range. *Physical Chemistry Chemical Physics : PCCP*, 17(29):19238–19246, 2015.
- [118] P. T. Landsberg and A. R. Beattie. Auger effect in semiconductors. *Journal of Physics and Chemistry of Solids*, 8:73–75, 1959.
- [119] W. Lochmann. Phonon-assisted Auger recombination in semiconductors. *Physica Status Solidi (a)*, 40(1):285–292, 1977.
- [120] M. Takeshima. Theory of phonon-assisted Auger recombination in semiconductors. *Physical Review B*, 23(12):6625–6637, 1981.
- [121] Y. Yang, M. Yang, Z. Li, R. Crisp, K. Zhu, and M. C. Beard. Comparison of recombination dynamics in $\text{CH}_3\text{NH}_3\text{PbBr}_3$ and $\text{CH}_3\text{NH}_3\text{PbI}_3$ perovskite films: Influence of exciton binding energy. *The Journal of Physical Chemistry Letters*, 6(23):4688–4692, 2015.
- [122] M. B. Johnston and L. M. Herz. Hybrid perovskites for photovoltaics: Charge-carrier recombination, diffusion, and radiative efficiencies. *Accounts of Chemical Research*, 49(1):146–154, 2016.
- [123] W. Pauli. Über den Zusammenhang des Abschlusses der Elektronengruppen im Atom mit der Komplexstruktur der Spektren. *Zeitschrift für Physik*, 31(1):765–783, 1925.
- [124] D. K. Ferry. *Semiconductors: Bonds and bands*. IOP Publishing Ltd, Bristol, UK, 2013.
- [125] K. F. Berggren and B. E. Sernelius. Band-gap narrowing in heavily doped many-valley semiconductors. *Physical Review B*, 24(4):1971–1986, 1981.

- [126] S. G. Lipson, H. Lipson, and D. Stefan Tannhauser. *Optical physics*. Cambridge Univ. Press, Cambridge [u.a.], 3 edition, 2004.
- [127] L. de Broglie. The reinterpretation of wave mechanics. *Foundations of Physics*, 1(1):5–15, 1970.
- [128] A. V. Crewe, J. Wall, and J. Langmore. Visibility of single atoms. *Science*, 168(3937):1338–1340, 1970.
- [129] G. Binnig, C. Quate, and C. Gerber. Atomic force microscope. *Physical Review Letters*, 56(9):930–933, 1986.
- [130] W. H. Bragg and W. L. Bragg. The reflection of x-rays by crystals. *Proceedings of the Royal Society A: Mathematical, Physical and Engineering Sciences*, 88(605):428–438, 1913.
- [131] A. Beer. Bestimmung der Absorption des rothen Lichts in farbigen Flüssigkeiten. *Annalen der Physik und Chemie*, 162(5):78–88, 1852.
- [132] J. Mooney and P. Kambhampati. Get the basics right: Jacobian conversion of wavelength and energy scales for quantitative analysis of emission spectra. *The Journal of Physical Chemistry Letters*, 4(19):3316–3318, 2013.
- [133] J. N. Coleman, M. Lotya, A. O’Neill, S. D. Bergin, P. J. King, U. Khan, K. Young, A. Gaucher, S. De, R. J. Smith, I. V. Shvets, S. K. Arora, G. Stanton, H.-Y. Kim, K. Lee, G. T. Kim, G. S. Duesberg, T. Hallam, J. J. Boland, J. J. Wang, J. F. Donegan, J. C. Grunlan, G. Moriarty, A. Shmeliov, R. J. Nicholls, J. M. Perkins, E. M. Grievson, K. Theuwissen, D. W. McComb, P. D. Nellist, and V. Nicolosi. Two-dimensional nanosheets produced by liquid exfoliation of layered materials. *Science*, 331(6017):568–571, 2011.
- [134] U. Khan, H. Porwal, A. O’Neill, K. Nawaz, P. May, and J. N. Coleman. Solvent-exfoliated graphene at extremely high concentration. *Langmuir*, 27(15):9077–9082, 2011.
- [135] K. R. Paton, E. Varrla, C. Backes, R. J. Smith, U. Khan, A. O’Neill, C. Boland, M. Lotya, O. M. Istrate, P. King, T. Higgins, S. Barwich, P. May, P. Puczkarski, I. Ahmed, M. Moebius, H. Pettersson, E. Long, J. Coelho, S. E. O’Brien, E. K. McGuire, B. M. Sanchez, G. S. Duesberg, N. McEvoy, T. J. Pennycook, C. Downing, A. Crossley, V. Nicolosi, and J. N. Coleman. Scalable production of large quantities of defect-free few-layer graphene by shear exfoliation in liquids. *Nature Materials*, 13(6):624–630, 2014.

- [136] Z. Cheng and J. Lin. Layered organic–inorganic hybrid perovskites: Structure, optical properties, film preparation, patterning and templating engineering. *CrystEngComm*, 12(10):2646, 2010.
- [137] C. C. Stoumpos, C. D. Malliakas, and M. G. Kanatzidis. Semiconducting tin and lead iodide perovskites with organic cations: Phase transitions, high mobilities, and near-infrared photoluminescent properties. *Inorganic Chemistry*, 52(15):9019–9038, 2013.
- [138] Y. Bekenstein, B. A. Koscher, S. W. Eaton, P. Yang, and A. P. Alivisatos. Highly luminescent colloidal nanoplates of perovskite cesium lead halide and their oriented assemblies. *Journal of the American Chemical Society*, 137(51):16008–16011, 2015.
- [139] I. Levchuk, P. Herre, M. Brandl, A. Osvet, R. Hock, W. Peukert, P. Schweizer, E. Spiecker, M. Batentschuk, and C. J. Brabec. Ligand-assisted thickness tailoring of highly luminescent colloidal $\text{CH}_3\text{NH}_3\text{PbX}_3$ (X = Br and I) perovskite nanoplatelets. *Chemical Communications*, 53(1):244–247, 2016.
- [140] Q. A. Akkerman, S. G. Motti, S. A. R. Kandada, E. Mosconi, V. D’Innocenzo, G. Bertoni, S. Marras, B. A. Kamino, L. Miranda, F. de Angelis, A. Petrozza, M. Prato, and L. Manna. Solution synthesis approach to colloidal cesium lead halide perovskite nanoplatelets with monolayer-level thickness control. *Journal of the American Chemical Society*, 138(3):1010–1016, 2016.
- [141] J. Shamsi, Z. Dang, P. Bianchini, C. Canale, F. Di Stasio, R. Brescia, M. Prato, and L. Manna. Colloidal synthesis of quantum confined single crystal CsPbBr_3 nanosheets with lateral size control up to the micrometer range. *Journal of the American Chemical Society*, 138(23):7240–7243, 2016.
- [142] L. Polavarapu, B. Nickel, J. Feldmann, and A. S. Urban. Advances in quantum-confined perovskite nanocrystals for optoelectronics. *Advanced Energy Materials*, 501:1700267, 2017.
- [143] F. Zhu, L. Men, Y. Guo, Q. Zhu, U. Bhattacharjee, P. M. Goodwin, J. W. Petrich, E. A. Smith, and J. Vela. Shape evolution and single particle luminescence of organometal halide perovskite nanocrystals. *ACS Nano*, 9(3):2948–2959, 2015.
- [144] N. K. Kumawat, N. Jain, A. Dey, K. L. Narasimhan, and D. Kabra. Quantitative correlation of perovskite film morphology to light emitting diodes efficiency parameters. *Advanced Functional Materials*, 27(3):1603219, 2017.

- [145] J. R. Klein, O. Flender, M. Scholz, K. Oum, and T. Lenzer. Charge carrier dynamics of methylammonium lead iodide: From PbI_2 -rich to low-dimensional broadly emitting perovskites. *Physical Chemistry Chemical Physics (PCCP)*, 18(16):10800–10808, 2016.
- [146] L. A. Kosyachenko. *Solar Cells - New Approaches and Reviews*. InTech, 2015.
- [147] L. Wang, C. McCleese, A. Kovalsky, Y. Zhao, and C. Burda. Femtosecond time-resolved transient absorption spectroscopy of $\text{CH}_3\text{NH}_3\text{PbI}_3$ perovskite films: Evidence for passivation effect of PbI_2 . *Journal of the American Chemical Society*, 136(35):12205–12208, 2014.
- [148] N. Pellet, J. Teuscher, J. Maier, and M. Grätzel. Transforming hybrid organic inorganic perovskites by rapid halide exchange. *Chemistry of Materials*, 27(6):2181–2188, 2015.
- [149] Y. Tong, E. Bladt, M. F. Aygüler, A. Manzi, K. Z. Milowska, V. A. Hintermayr, P. Docampo, S. Bals, A. S. Urban, L. Polavarapu, and J. Feldmann. Highly luminescent cesium lead halide perovskite nanocrystals with tunable composition and thickness by ultrasonication. *Angewandte Chemie*, 55(44):13887–13892, 2016.
- [150] S. Gonzalez-Carrero, G. M. Espallargas, R. E. Galian, and J. Pérez-Prieto. Blue-luminescent organic lead bromide perovskites: Highly dispersible and photostable materials. *Journal of Materials Chemistry A*, 3(26):14039–14045, 2015.
- [151] R. Sheng, A. Ho-Baillie, S. Huang, S. Chen, X. Wen, X. Hao, and M. A. Green. Methylammonium lead bromide perovskite-based solar cells by vapor-assisted deposition. *The Journal of Physical Chemistry C*, 119(7):3545–3549, 2015.
- [152] W.-Y. Wu, J. N. Schulman, T. Y. Hsu, and U. Efron. Effect of size nonuniformity on the absorption spectrum of a semiconductor quantum dot system. *Applied Physics Letters*, 51(10):710–712, 1987.
- [153] Z. Dang, J. Shamsi, F. Palazon, M. Imran, Q. A. Akkerman, S. Park, G. Bertoni, M. Prato, R. Brescia, and L. Manna. In situ transmission electron microscopy study of electron beam-induced transformations in colloidal cesium lead halide perovskite nanocrystals. *ACS Nano*, 11(2):2124–2132, 2017.
- [154] Z. Wang, X.-D. Wen, R. Hoffmann, J. S. Son, R. Li, C.-C. Fang, D.-M. Smilgies, and T. Hyeon. Reconstructing a solid-solid phase transformation pathway in CdSe nanosheets with associated soft ligands. *Proceedings of the National Academy of Sciences of the United States of America*, 107(40):17119–17124, 2010.

- [155] G. Bastard, E. E. Mendez, L. L. Chang, and L. Esaki. Exciton binding energy in quantum wells. *Physical Review B*, 26(4):1974–1979, 1982.
- [156] A. Chernikov, T. C. Berkelbach, H. M. Hill, A. Rigosi, Y. Li, O. B. Aslan, D. R. Reichman, M. S. Hybertsen, and T. F. Heinz. Exciton binding energy and nonhydrogenic Rydberg series in monolayer WS₂. *Physical Review Letters*, 113(7):076802, 2014.
- [157] O. Yaffe, A. Chernikov, Z. M. Norman, Y. Zhong, A. Velauthapillai, A. van der Zande, J. S. Owen, and T. F. Heinz. Excitons in ultrathin organic-inorganic perovskite crystals. *Physical Review B*, 92(4):716, 2015.
- [158] L. V. Keldysh. Coulomb interaction in thin semiconductor and semimetal films. *Soviet Journal of Experimental and Theoretical Physics Letters*, (29), 1979.
- [159] Q. Chen, N. de Marco, Y. Yang, T.-B. Song, C.-C. Chen, H. Zhao, Z. Hong, and H. Zhou. Under the spotlight: The organic–inorganic hybrid halide perovskite for optoelectronic applications. *Nano Today*, 10(3):355–396, 2015.
- [160] J. Even, L. Pedesseau, and C. Katan. Understanding quantum confinement of charge carriers in layered 2d hybrid perovskites. *ChemPhysChem*, 15(17):3733–3741, 2014.
- [161] Q. Lin, A. Armin, R. C. R. Nagiri, P. L. Burn, and P. Meredith. Electro-optics of perovskite solar cells. *Nature Photonics*, 9(2):106–112, 2014.
- [162] S. Sun, T. Salim, N. Mathews, M. Duchamp, C. Boothroyd, G. Xing, T. C. Sum, and Y. M. Lam. The origin of high efficiency in low-temperature solution-processable bilayer organometal halide hybrid solar cells. *Energy Environment Science*, 7(1):399–407, 2014.
- [163] N. Sestu, M. Cadelano, V. Sarritzu, F. Chen, D. Marongiu, R. Piras, M. Mainas, F. Quochi, M. Saba, A. Mura, and G. Bongiovanni. Absorption f-sum rule for the exciton binding energy in methylammonium lead halide perovskites. *The Journal of Physical Chemistry Letters*, 6(22):4566–4572, 2015.
- [164] Y. Yamada, T. Nakamura, M. Endo, A. Wakamiya, and Y. Kanemitsu. Photoelectronic responses in solution-processed perovskite CH₃NH₃PbI₃ solar cells studied by photoluminescence and photoabsorption spectroscopy. *IEEE Journal of Photovoltaics*, 5(1):401–405, 2015.
- [165] A. Miyata, A. Mitiglu, P. Plochocka, O. Portugall, J. T.-W. Wang, S. D. Stranks, H. J. Snaith, and R. J. Nicholas. Direct measurement of the exciton binding energy

- and effective masses for charge carriers in organic–inorganic tri-halide perovskites. *Nature Physics*, 11(7):582–587, 2015.
- [166] Y. Yang, D. P. Ostrowski, R. M. France, K. Zhu, J. van de Lagemaat, J. M. Luther, and M. C. Beard. Observation of a hot-phonon bottleneck in lead-iodide perovskites. *Nature Photonics*, 10(1):53–59, 2015.
- [167] Y. Hassan, Y. Song, R. D. Pensack, A. I. Abdelrahman, Y. Kobayashi, M. A. Winnik, and G. D. Scholes. Structure-tuned lead halide perovskite nanocrystals. *Advanced Materials*, 28(3):566–573, 2016.
- [168] K. Tanaka and T. Kondo. Bandgap and exciton binding energies in lead-iodide-based natural quantum-well crystals. *Science and Technology of Advanced Materials*, 4(6):599–604, 2016.
- [169] G. C. Papavassiliou and I. B. Koutselas. Structural, optical and related properties of some natural three- and lower-dimensional semiconductor systems. *Synthetic Metals*, 71(1-3):1713–1714, 1995.
- [170] X. Wu, M. T. Trinh, D. Niesner, H. Zhu, Z. Norman, J. S. Owen, O. Yaffe, B. J. Kudisch, and X.-Y. Zhu. Trap states in lead iodide perovskites. *Journal of the American Chemical Society*, 137(5):2089–2096, 2015.
- [171] D. Saponi, M. Kepenekian, L. Pedesseau, C. Katan, and J. Even. Quantum confinement and dielectric profiles of colloidal nanoplatelets of halide inorganic and hybrid organic-inorganic perovskites. *Nanoscale*, 8(12):6369–6378, 2016.
- [172] D. M. Jang, K. Park, D. H. Kim, J. Park, F. Shojaei, H. S. Kang, J.-P. Ahn, J. Woon Lee, and J. K. Song. Reversible halide exchange reaction of organometal trihalide perovskite colloidal nanocrystals for full-range band gap tuning. *Nano Letters*, 15(8):5191–5199, 2015.
- [173] Q. A. Akkerman, V. D’Innocenzo, S. Accornero, A. Scarpellini, A. Petrozza, M. Prato, and L. Manna. Tuning the optical properties of cesium lead halide perovskite nanocrystals by anion exchange reactions. *Journal of the American Chemical Society*, 137(32):10276–10281, 2015.
- [174] A. Kojima, M. Ikegami, K. Teshima, and T. Miyasaka. Highly luminescent lead bromide perovskite nanoparticles synthesized with porous alumina media. *Chemistry Letters*, 41(4):397–399, 2012.

- [175] N. Onoda-Yamamuro, T. Matsuo, and H. Suga. Calorimetric and IR spectroscopic studies of phase transitions in methylammonium trihalogenoplumbates (II). *Journal of Physics and Chemistry of Solids*, 51(12):1383–1395, 1990.
- [176] C. Wehrenfennig, M. Liu, H. J. Snaith, M. B. Johnston, and L. M. Herz. Charge carrier recombination channels in the low-temperature phase of organic-inorganic lead halide perovskite thin films. *APL Materials*, 2(8):081513, 2014.
- [177] D. Li, G. Wang, H.-C. Cheng, C.-Y. Chen, H. Wu, Y. Liu, Y. Huang, and X. Duan. Size-dependent phase transition in methylammonium lead iodide perovskite microplate crystals. *Nature Communications*, 7:11330, 2016.
- [178] X. Xi, L. Zhao, Z. Wang, H. Berger, L. Forró, J. Shan, and K. F. Mak. Strongly enhanced charge-density-wave order in monolayer NbSe₂. *Nature Nanotechnology*, 10(9):765–769, 2015.
- [179] Y. Yu, F. Yang, X. F. Lu, Y. J. Yan, Y.-H. Cho, L. Ma, X. Niu, S. Kim, Y.-W. Son, D. Feng, S. Li, S.-W. Cheong, X. H. Chen, and Y. Zhang. Gate-tunable phase transitions in thin flakes of 1T-TaS₂. *Nature Nanotechnology*, 10(3):270–276, 2015.
- [180] M. J. Mayo, A. Suresh, and W. D. Porter. Thermodynamics for nanosystems: Grain and particle-size dependent phase diagrams. *Reviews on Advance Materials Science*, (5):100–109, 2003.
- [181] M. Hirasawa, T. Ishihara, T. Goto, K. Uchida, and N. Miura. Magnetoabsorption of the lowest exciton in perovskite-type compound CH₃NH₃PbI₃. *Physica B: Condensed Matter*, 201:427–430, 1994.
- [182] B. Anand, S. Sampat, E. O. Danilov, W. Peng, S. M. Rupich, Y. J. Chabal, Y. N. Gartstein, and A. V. Malko. Broadband transient absorption study of photoexcitations in lead halide perovskites: Towards a multiband picture. *Physical Review B*, 93(16), 2016.
- [183] M. B. Price, J. Butkus, T. C. Jellicoe, A. Sadhanala, A. Briane, J. E. Halpert, K. Broch, Justin M. Hodgkiss, R. H. Friend, and F. Deschler. Hot-carrier cooling and photoinduced refractive index changes in organic-inorganic lead halide perovskites. *Nature Communications*, 6:8420, 2015.
- [184] A. Sadhanala, F. Deschler, T. H. Thomas, S. E. Dutton, K. C. Goedel, F. C. Hanusch, M. L. Lai, U. Steiner, T. Bein, P. Docampo, D. Cahen, and R. H. Friend. Preparation of single-phase films of CH₃NH₃Pb(I_{1-x}Br_x)₃ with sharp optical band edges. *The Journal of Physical Chemistry Letters*, 5(15):2501–2505, 2014.

- [185] L. Q. Phuong, Y. Yamada, M. Nagai, N. Maruyama, A. Wakamiya, and Y. Kanemitsu. Free carriers versus excitons in $\text{CH}_3\text{NH}_3\text{PbI}_3$ perovskite thin films at low temperatures: Charge transfer from the orthorhombic phase to the tetragonal phase. *The Journal of Physical Chemistry Letters*, 7(13):2316–2321, 2016.
- [186] R. Heitz, A. Kalburge, Q. Xie, M. Grundmann, P. Chen, A. Hoffmann, A. Madhukar, and D. Bimberg. Excited states and energy relaxation in stacked InAs/GaAs quantum dots. *Physical Review B*, 57(15):9050–9060, 1998.
- [187] P. Guyot-Sionnest, M. Shim, C. Matranga, and M. Hines. Intraband relaxation in CdSe quantum dots. *Physical Review B*, 60(4):R2181–R2184, 1999.
- [188] A. Pandey and P. Guyot-Sionnest. Slow electron cooling in colloidal quantum dots. *Science*, 322(5903):929–932, 2008.
- [189] G. Czycholl. *Theoretische Festkörperphysik: Von den klassischen Modellen zu modernen Forschungsthemen*. Springer, Berlin and Heidelberg, 2008.
- [190] W. Pötz. Hot-phonon effects in bulk GaAs. *Physical Review B*, 36(9):5016–5019, 1987.
- [191] D. Chemla, D. Miller, P. Smith, A. C. Gossard, and W. Wiegmann. Room temperature excitonic nonlinear absorption and refraction in GaAs/AlGaAs multiple quantum well structures. *IEEE Journal of Quantum Electronics*, 20(3):265–275, 1984.
- [192] W. F. Brinkman and T. M. Rice. Electron-hole liquids in semiconductors. *Physical Review B*, 7(4):1508–1523, 1973.
- [193] H. Bao, B. F. Habenicht, O. V. Prezhdo, and X. Ruan. Temperature dependence of hot-carrier relaxation in PbSe nanocrystals: An ab initio study. *Physical Review B*, 79(23), 2009.
- [194] R. R. Cooney, S. L. Sewall, E. A. Dias, D. M. Sagar, K. E. H. Anderson, and P. Kambhampati. Unified picture of electron and hole relaxation pathways in semiconductor quantum dots. *Physical Review B*, 75(24):281, 2007.
- [195] W. H. Knox, R. L. Fork, M. C. Downer, D. A. B. Miller, D. S. Chemla, C. V. Shank, A. C. Gossard, and W. Wiegmann. Femtosecond dynamics of resonantly excited excitons in room-temperature GaAs quantum wells. *Physical Review Letters*, 54(12):1306–1309, 1985.

- [196] Y. Tong, F. Ehrat, W. Vanderlinden, C. Cardenas-Daw, J. K. Stolarczyk, L. Polavarapu, and A. S. Urban. Dilution-induced formation of hybrid perovskite nanoplatelets. *ACS Nano*, 10(12):10936–10944, 2016.
- [197] J. Feldmann, G. Peter, E.O. Göbel, P. Dawson, K. Moore, C. Foxon, and R. J. Elliott. Linewidth dependence of radiative exciton lifetimes in quantum wells. *Physical Review Letters*, 59(20):2337–2340, 1987.
- [198] D. S. Citrin. Homogeneous-linewidth effects on radiative lifetimes of excitons in quantum wells. *Solid State Communications*, 84(3):281–284, 1992.
- [199] A. L. Efros, C. Wetzel, and J. M. Worlock. Effect of a random adiabatic potential on the optical properties of two-dimensional excitons. *Physical Review B*, 52(11):8384–8390, 1995.

List of abbreviations

AFM	atomic force microscopy
BGR	band gap renormalization
BZ	Brillouin zone
CB	conduction band
CBM	conduction band minimum
CBR	conduction band renormalization
DFT	density-functional theory
DT	differential transmission
DOS	density of states
EDX	energy-dispersive X-ray spectroscopy
FRET	Förster resonance energy transfer
FWHM	full-width half maximum
GSB	ground state bleach
GW	Green's function, screened Coulomb interaction
HOMO	highest occupied molecular orbital
HE	heavy electron
HH	heavy hole
HRTEM	high-resolution transmission electron microscope
JDOS	joint density of states
LO	longitudinal optical
LE	light electron
LH	light hole
LUMO	lowest unoccupied molecular orbital
MA	methylammonium (CH_3NH_3)
MAPBr	methylammonium lead bromide ($\text{CH}_3\text{NH}_3\text{PbBr}_3$)
MAPCl	methylammonium lead chloride ($\text{CH}_3\text{NH}_3\text{PbCl}_3$)
MAPI	methylammonium lead iodide ($\text{CH}_3\text{NH}_3\text{PbI}_3$)
NC	nanocrystal
NPl	nanoplatelet
NIR	near-infrared
OD	optical density
OPA	optical parametric amplifier
PL	photoluminescence
PIB	photoinduced bleaching

QY	quantum yield
SEM	scanning electron microscope
SF	Sommerfeld factor
SO	split-off band
SOC	spin-orbit coupling
SPM	scanning probe microscopy
STEM	scanning transmission electron microscope
TAS	transient absorption spectroscopy
TEM	transmission electron microscope
UV	ultra-violet
VB	valence band
VBM	valence band maximum
VBR	valence band renormalization
Vis	visible
WLG	white light generator
XRD	X-ray diffraction
3D	three-dimensional
2D	two-dimensional

Acknowledgment

During the time at the Chair of Photonic and Optoelectronic I learned a lot, not only professionally but also personally. I would like to take this opportunity to thank the people who supported me the most in completing my thesis.

First of all, I want to thank my 'Doktorvater' Prof. Dr. Jochen Feldmann. He gave me the opportunity to do my PhD thesis at his chair and always supported me in my scientific work and gave me guidance if needed. In numerous discussions, I benefited from his knowledge and experience and learned how to carry out scientific work.

Many thanks to Dr. Alexander Urban. He is always open for new ideas and supported me with his knowledge in various scientific fields. The door to his office was (literally) always open whenever I had any question.

I am thankful to Dr. Lakshminarayana Polavarapu who guided me during my starting time in the chemistry lab and helped me to gain more skills in chemistry in general and in performing synthesis in particular.

I want to thank Prof. Dr. Thomas Bein, Prof. Dr. Joachim Rädler and Prof. Dr. Hermann Gaub for providing the HRTEM, TEM and AFM equipment respectively and Dr. Willem Vanderlinden and Dr. Markus Döblinger for performing measurements on the AFM and HRTEM.

Many thanks to my colleagues Alexander Richter, Aurora Manzi, Yu Tong, Jasmina Sichert and Bernhard Bohn, who also work on perovskites for the great teamwork and excellent working climate.

I want to thank the master students I was working with: Niklas Mutz, Alexander Richter und Max Löw.

Thank you Thomas Simon for introducing me to the Pump-Probe setup and for sharing your memorable stories.

Christoph Maier, Florian Ehrat, Carla Pernpeintner, Patrick Urban, Felix Winter, Aurora

Manzi, Bernhard Bohn, thanks for your friendship! It has been golden times and it is more than a degree I made during the time at the chair.

Special thanks to Gerlinde Adam for taking care of the administration and us.

Thanks to Stefan Niedermaier for the help in all technical questions and the design of specialized devices.

My special thanks go to all my colleagues at the Chair of Photonics and Optoelectronics, there are too many to list all of them. I always liked to go to work not least because of you.

Last but not least, I want to thank my family and friends. Especially my parents, Sebastian Hintermayr and Regina Hintermayr, deserve the greatest thank you of all. Without their support and never-ending sympathy I would not have studied in the first place.

Thanks to all of you for your encouragement and enrichment of my everyday life.